NTNU

Norwegian University of
Science and Technology

Low Frequency AC Transmission

Investigating the Dynamics of an Export Cable
for Offshore Wind Power Applications

Henrik Waje-Andreassen

Master of Energy and Environmental Engineering
Submission date: February 2016
Supervisor: Kjetil Uhlen, ELKRAFT

Norwegian University of Science and Technology
Department of Electric Power Engineering

Problem Description

The use of low frequency alternating current (LFAC) power transmission has been proposed in different studies as an alternative to high voltage direct current (HVDC) transmission from offshore wind farms, thereby seeking out to be a competitive technology for the mid-range transmission distance where conventional high voltage alternating current (HVAC) transmission is no longer an attractive solution. The properties of the subsea export cable must be examined when operated at lower frequencies in order to design a complete LFAC transmission system, and this thesis investigates the export cable for certain steady state and dynamic conditions.

Abstract

In the following thesis, the properties of a $16^{2}/_{3}$Hz, low frequency alternating current (LFAC) export cable was examined in both steady state and dynamic conditions, as part of a simplified offshore transmission system. Simulations were performed for both LFAC and conventional 50 Hz high voltage alternating current (HVAC) systems for comparison purposes. Introductory to the simulations, different cable models were investigated. Using MATLAB/SIMULINK SimPowerSystems, the use of the built-in distributed parameters model (DPM) was considered the best option for simulation, especially when studying the power cable in dynamic situations. For steady state conditions, the utilization of the series π-model showed satisfying results, e.g. when the effect of voltage rise in a lightly loaded or unloaded transmission system was studied (Ferranti effect). The results revealed a significantly lower voltage increase across the LFAC cable compared to a conventional HVAC cable. Thus, in the case of sudden disconnections or loss of load, the risk of damaging transmission system components can be lower for an LFAC system compared to an HVAC system.

Charging currents were observed to be lower and less sensitive to cable length variations for an LFAC cable compared to an HVAC cable. Thus, more active power is allowed to be transmitted in the LFAC cable. During energization of the cable, the LFAC voltages and currents experienced temporary transient distortions of the waveform before stabilizing at steady state, whereas the same distortions were not observed for the HVAC system. Transient distortions were also observed in the fault analysis for different short circuit (SC) events; three phase to ground, double phase to ground and phase to phase faults. The fourth SC event, the single phase to ground fault, showed very little distortion. However, the highest direct current (DC) offset magnitude was observed for the phase to ground voltages posterior to this fault. DC offsets were also observed after clearing the three phase to ground fault and double phase to ground fault, resulting from the lack of grounding in the cable system. The DC offsets were present for a long period of time; up to 100 seconds depending on the type of fault, and the magnitude of the DC offsets was significantly higher for the HVAC system. Connecting the cable's end terminal to ground through a shunt reactor resulted in a far lower DC offset magnitude

which was rapidly damped to zero. Similar oscillations were observed for the HVAC system, and the DC offset was damped faster in this case due to higher resistance in the cable. The frequency of the oscillations were ∼30 Hz for the LFAC system and ∼44 Hz for the HVAC system, and it should be examined whether such oscillations may contribute to resonance in the power system. Possible measures to increase the damping of the oscillations would be a better optimization of the shunt reactor.

Common for the dynamic situations investigated was the presence of harmonic distortion after switching operations or faults/clearing of faults. In the case of switching operations, the problem of transient distortion could possibly be more prominent for LFAC transmission systems compared to HVAC systems. However, further studies should be carried out before making final conclusions on this topic. In summary, the LFAC cable showed promising results in terms of overvoltages under steady and dynamic situations compared to a conventional HVAC system.

Sammendrag

I den følgende masteroppgaven ble en lavfrekvent vekselstrøms (low frecuency alternating current, LFAC) sjøkabel undersøkt i stasjonære og dynamiske situasjoner, som del av et forenklet offshore kraftsystem. Simuleringer ble også utført for et konvensjonelt 50 Hz høyspent vekselstrømsystem (high voltage alternating current, HVAC), for å bedre kunne trekke frem fordeler og ulemper ved bruk av LFAC. Som en introduksjon til simuleringene ble forskjellige kabelmodeller undersøkt, og gjennom bruk av MATLAB/SIMULINK SimPowerSystems ble det konkludert med at den innebygde modellen basert på distribuerte parametre var mest egnet for simuleringer, spesielt i tilfeller hvor kraftsystemet ble undersøkt under dynamisk tilstand. For stasjonær tilstand var det mulig å benytte seg av π-modellen, som f.eks ved simulering av spenningsstigning i en lang kabel med åpen ende (Ferrantieffekten). Resultatene viste en påfallende lavere spenningsstigning for en LFAC-kabel sammenlignet med en HVAC-kabel. Skulle et LFAC transmisjonssystem oppleve brudd eller plutselig tap av last, vil det dermed være betydelig mindre risiko for overspenninger som kan skade andre komponenter i kraftsystemet.

Ladestrømmene ble observert å være lavere for LFAC-systemet sammenlignet med HVAC-systemet, samtidig som de var mindre sensitive for endringer av den totale kabellengden. Under lading ble det påvist temporære transiente forstyrrelser for både spenning og ladestrøm i LFAC-systemet, mens tilsvarende forstyrrelser ikke ble observert for HVAC-systemet. I feilanalysen ble det oppdaget transiente forstyrrelser for tre typer kortslutningsfeil; trefase til jord-, dobbeltfase til jord- og fase til fase-feil. Selv om tilsvarende interferens ikke ble påvist for enkeltfase til jord-feil, oppstod det en kraftig likestrømskomponent (DC-komponent) for spenningssignalene etter feilklarering. DC-komponenter i spenningen ble også påvist ved begge ender av kabelen etter trefase- og dobbeltfasekortslutninger, som kan forklares av manglende jording ved kabelens terminaler. DC-komponentene var langvarige; opp til 100 sekunder avhengig av typen feil, og DC-komponentens magnitude var betydelig høyere for HVAC-systemet. Gjennom jordtilkobling via en shuntreaktor ved mottakersiden av kabelen ble DC-komponenten

raskt dempet. I dette tilfellet ble det imidlertid påvist lavfrekvente svingninger i DC-komponeneten; ∼30 Hz for LFAC-systemet og ∼44 Hz for HVAC-systemet, og det bør undersøkes om slike svingninger kan bidra til resonans. Et tiltak for ytterligere demping er bedre optimalisering av shuntreaktoren.

Felles for de undersøkte dynamiske situasjonene var forekomsten av harmonisk interferens etter bryteroperasjoner og feil/feilgjenoppretting. Det er en mulighet for at harmonisk interferens er et større problem i LFAC-systemer enn i HVAC-systemer ved bryteroperasjoner. Det er imidlertid nødvendig med ytterligere studier på dette feltet før man trekker endelige konklusjoner. Totalt sett viste LFAC-systemet lovende resultater med tanke på overspenninger i både stasjonære og dynamiske tilfeller.

Acknowledgements

Firstly, I would like to thank Statkraft for providing an interesting topic in the field of offshore wind energy, and my contact Sverre Skalleberg Gjerde for having taken the time to give detailed and valuable feedback despite being very occupied with his work. His effort to arrange meetings in a tight schedule is very much appreciated. I would also like to thank my supervisor prof. Kjetil Uhlen for being available answering questions and giving advice to improve the quality of the thesis. Secondly, I would like to give a huge thanks to my friend Stian Solberg and my parents for reading through my work, correcting errors that I have been blind to. I would also like to give thanks to NTNU for taking good care of me while being a student, and to my friends and co-students for the countless coffee-breaks, lunches and dinners, making five years of studying memorable and fun.

Contents

List of Figures

List of Tables

Abbreviations

AC	Alternating Current
BD	Breakeven Distance
CB	Circuit Breaker
DC	Direct Current
DPM	Distributed Parameters Model
GMR	Geometric Mean Radius
HVAC	High Voltage Alternating Current
HVDC	High Voltage Direct Current
IGBT	Insulated-Gate Bipolar Transistor
KCL	Kirchoff's Current Law
KVL	Kirchoff's Voltage Law
LCC	Line Commutated Converter
LF	Low Frequency
LFAC	Low Frequency Alternating Current
MMC	Modular Multi-level Converter
OHL	Overhead Line
OWF	Offshore Wind Farm
RMS	Root Mean Square
SC	Short Circuit
SR	Shunt Reactor
VSC	Voltage Source Converter

Symbols

A	conductor cross-section area
A_c	cross sectional area in transformer core
B	magnetic flux density
C	capacitance per unit length
D_e	penetration depth of the earth
E	electromagnetic emf induced in the transformer coils
f	frequency
G	conductance per unit length
GMR	geometric mean radius of a conductor
I_c	charging current
I_R	receiving end current
I_S	sending end current
I_{th}	current-carrying capacity of a transmission cable
l	length of transmission line/cable
L	inductance per unit length
L_s	inductance representing the offshore wind farm components
N	number of cascaded π-sections in a series π-model
N_t	number of turns in a transformer
P	active power
Q	reactive power
R	resistance per unit length
R_{DC}	resistance for a conductor under DC conditions
R_s	resistance representing the offshore wind farm components
S	apparent power
S_{base}	base power for per unit measurements

S_{th}	thermal loading limit of a transmission line/cable
v	traveling wave propagation speed
V_{base}	base voltage for per unit measurements
V_R	receiving end voltage
$V_{R,DC}$	receiving end voltage DC offset
$V_{R,DC_{avg}}$	average DC offset of the receiving end voltage
V_s	wind farm side voltage
V_S	sending end voltage
y_p	proximity effect factor
y_s	skin effect factor
Z_c	characteristic impedance

α	attenuation constant
α_T	temperature coefficient
β	phase constant
δ	transmission angle
ϵ	permittivity
γ	propagation constant
μ	permeability
ω	angular frequency
ρ	electrical resistivity
σ	conductivity
τ	traveling wave time delay

Chapter 1

Introduction

1.1 Background

The world's increasing population and the industrialization of former underdeveloped countries creates a huge demand for energy in the future. As fossil energy resources become scarce, many industrialized countries seek to increase the share of electricity production originating from renewable energy sources. From 1990 to 2012, there has been a nearly continuous increase of power production originating from renewables in Europe. Scenarios predict wind energy producing up to 34% of Europe's electricity demand by 2030, where production from offshore wind installations might exceed 200 GW (compared to 8 GW in 2014) [1][2]. This requires a long-term strategic approach in both technology and policy research, and several European countries are taking major roles in developing the renewable energy sector. The German government has already decided to vastly increase the electricity production originating from renewable energy sources at the expense of fossil fuels and nuclear sources [3]. The UK has set a goal to have renewables cover 15% of the energy consumption by 2020, and by 2030 the share of energy production in the UK coming from wind energy is expected to reach almost 50% [4][2]. To reach this goal, offshore construction projects have been distributed to different developers by the Crown Estate through a span of three rounds. The first two rounds include small/medium wind farms relatively close to shore, while the third round includes large far-from-shore installations with significantly larger capacity [5].

By the end of June 2015, there are 3,072 offshore wind turbines with a total capacity of 10,393.5 MW connected to the European grid [6]. Fig. 1.1 shows the average size of wind farms (in megawatts) installed offshore and added capacity connected to the grid annually from 2009 to 2014.

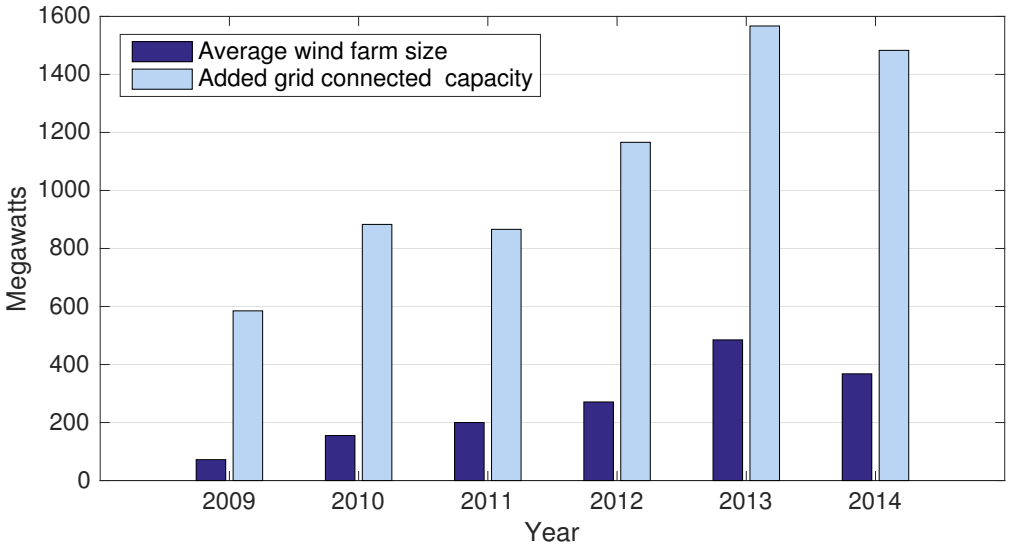

FIGURE 1.1: Average installed wind farm size and added grid-connected capacity per year

Thus far, the construction of offshore wind farms are based on the concept of installing the wind turbines directly on the seabed, either by using monopoles or jacket foundations. As the water depth exceeds approximately 50 meters, new construction methods must be introduced in order to build floating wind farms in the future. Recently, Statoil got approval for building floating offshore wind turbines in Scotland [7], and a commercialization of wind farms utilizing this concept would be a milestone in offshore wind farm construction, resulting in projects that would not be feasible with the current-day technology. Figure 1.2 shows the water depth in European waters, where the North Sea has a large share of shallow waters compared to other seas. Especially Denmark, the UK, the Netherlands and Germany have the possibility to exploit the shallow waters for offshore wind warm construction.

Over the last years, offshore wind farms are being built at deeper waters and farther away from shore, where the wind velocities are higher and more predictable. Thus more wind power can be produced, and the negative visual impact associated with wind farms will be eliminated. Fig. 1.3 shows the average distance to shore from offshore wind farms completed or partially completed each year from 2009 to 2014, as well as the average water depth [8][9][10][11][12]. However, constructing wind farms far from the shore introduces challenges in the power transmission.

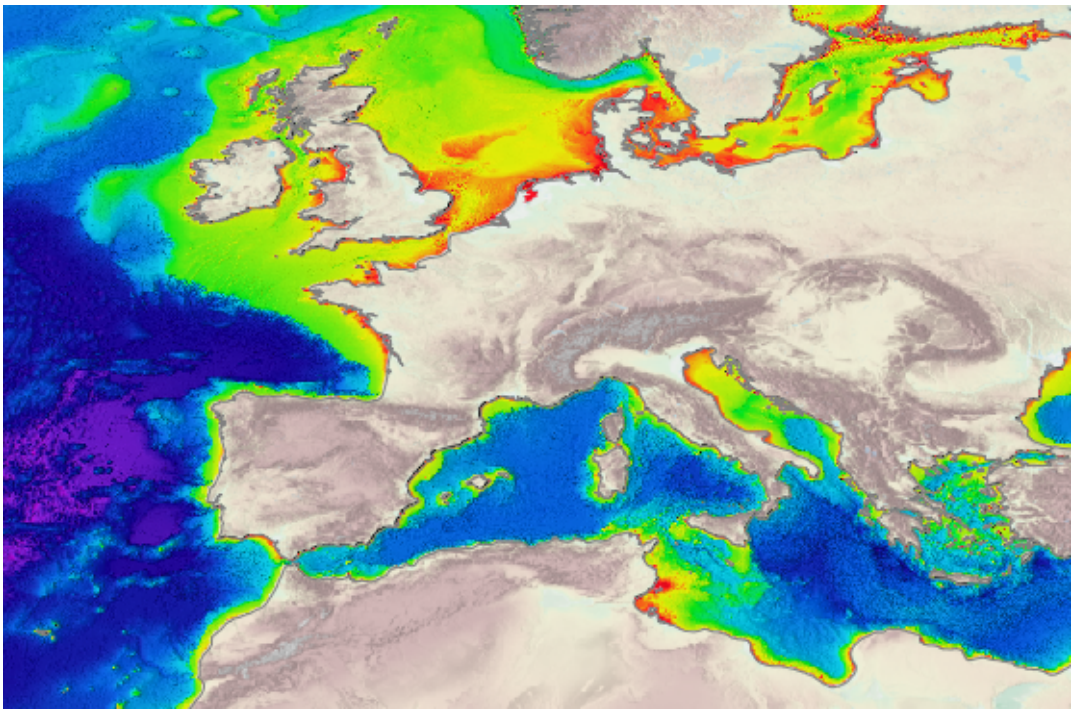

FIGURE 1.2: Map showing bathymetry in Europe. Red and yellow colors indicate shallow waters ranging between 0-50 meters [13]

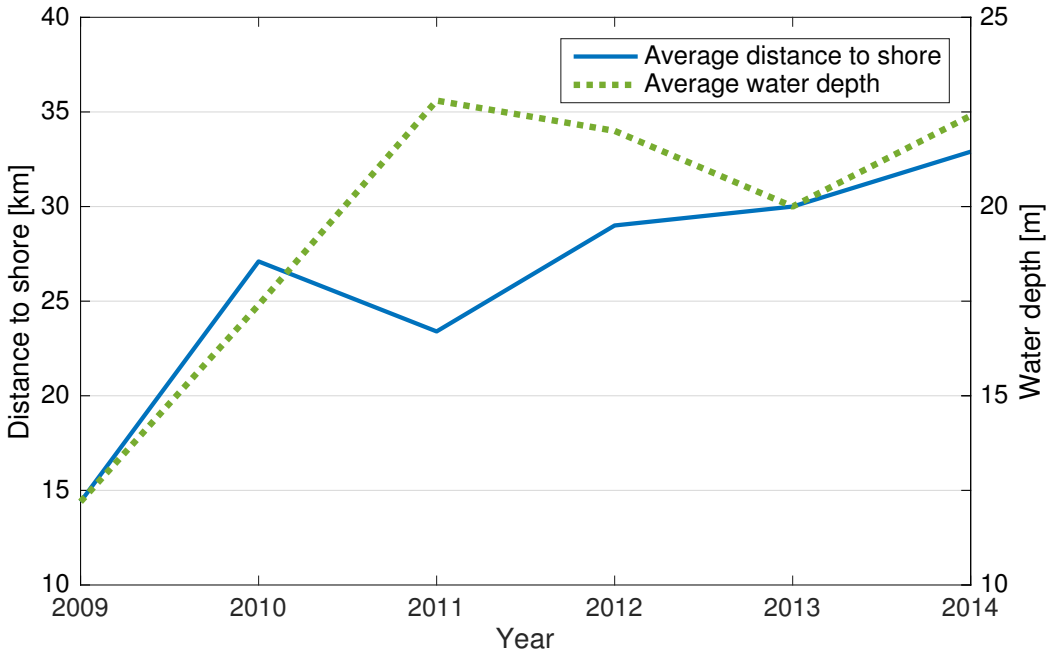

FIGURE 1.3: Average distance to shore and water depth for offshore wind farms installed per year

1.2 State-of-the-art Power Transmission Technology

Today, offshore wind farms at distances exceeding approximately 100 km from shore would utilize a high voltage direct current (HVDC) transmission system based on voltage source converter (VSC) technology. Among the VSCs, the use of the modular multi-level converter (MMC) offers some advantages compared to other VSCs such as the two- or three-level converter topologies. Some of the benefits are[14][15]:

- Harmonic generation is kept low.
- No large capacitor needed at the DC terminals. Replaced by multiple smaller modules.
- No filter needed on the AC side.
- Lower losses due to low resulting switching frequency.
- Semiconductor components can be optimized for low conduction losses.

With an HVDC transmission system, it is in theory possible to transmit power over an unlimited distance, and losses are minimal. When the use of high voltage alternating current (HVAC) becomes unfeasible due to technical or economical limitations[1], HVDC is used. However, the construction of an offshore HVDC VSC transmission system introduces high costs, mainly due to the investment costs of the converter stations that must be installed offshore.

In an effort to extend the feasibility regarding offshore HVAC transmission, the concept of low frequency alternating current (LFAC) transmission has been introduced. The idea dates back to the nineties, where a transmission system based on fractional frequency transmission was introduced as an alternative to HVDC for long-distance in-land systems [16]. Additionally, several railway systems in Europe are operated on lower frequencies than the conventional transmission and distribution frequency.

The frequency of choice in this thesis is $16^2/_3$ Hz, which is mainly due to the fact that multiple railway grids operate at, or close to this frequency. For instance, Norwegian and Swedish railway systems use $16^2/_3$ Hz, whereas German and Swiss systems use 16.7 Hz[2]. This is an advantage as many power system components are designed for such a low frequency, however at lower voltage levels. In order to optimize for a high voltage power transmission system, modifications must be made. Although some technology can be adopted from the railway sector, it is important to take the space limitations at offshore wind farms into consideration.

[1] See chapter 2 for details.

[2] Though the difference is small, the two frequencies should *not* be treated as being equal.

1.3 Motivation and Objectives

The thesis aims to investigate the feasibility of using technology alternative to HVDC transmission solutions for offshore wind farms located in the range of 200 km from shore. The concept of using LFAC transmission and thereby introducing possible cost savings in both investment and maintenance, could result in a larger commitment to offshore wind energy in the future. The export cable will be studied and modeled for both steady state and dynamic conditions, and the results from the LFAC simulations will in most cases be compared to simulations performed on a conventional HVAC system. In short, the thesis will include the following topics:

1. Finding an appropriate model for an offshore LFAC cable.
2. Frequency analysis of an LFAC export cable, investigating the impact of the nominal frequency of the transmission system, cable length and inductive elements in the transmission system.
3. Steady state analysis of an LFAC export cable, where the phenomenon of increased voltage in a lightly or even unloaded transmission system, also known as the Ferranti effect, will be examined.
4. Dynamic behavior of an LFAC export cable during charging and fault events.
5. Investigating occurring voltage DC offsets following certain short circuit faults.

1.4 Approach

Although the term LFAC refers to a low frequency AC system, it is important to keep in mind that LFAC is a subclass of the HVAC technology (the most accurate term would be LF HVAC). In this thesis, systems based on $16^2/_3$ Hz and 50 Hz will be compared. When discussing the two systems, the term LFAC refers to the use of $16^2/_3$ Hz. Similarly, the term HVAC implies the use of a conventional 50 Hz AC system.

For the simulations, the cable will primarily have a length of 200 km, however other lengths will be investigated as well. Based on theoretical and practical considerations regarding the state of the system, an appropriate model will be chosen for each situation. The theoretical understanding for different cable models will be given separately and prior to the chapters where the simulations are performed.

Simulations will be performed in MATLAB/SIMULINK SimPowerSystems. For the frequency analysis in chapter 4, the analysis is performed on a single-phase system, whereas three-phase circuits will be used in chapters 5, 6 and 7.

1.5 Limitations

When examining a transmission system based on LFAC technology, there are many different aspects to take into consideration. Examples include all the different electrical components in a transmission system (generators, converters, breakers etc.), which have been subjects of study in the pre-project report [17]. Also, the impact of LFAC solutions on the total costs can be studied in detail. As this thesis aims to investigate the export cable in an LFAC transmission system, it is not possible to explore other system components in detail, and limitations are necessary:

- The turbines will not be examined in detail, and different concepts of wind farm designs are also left out. The offshore wind farm will therefore be considered as one large generating unit, including some internal resistance and inductance.
- The report will primarily compare LFAC to conventional HVAC offshore transmission systems, although it could be interesting to see the benefits/drawbacks compared to HVDC transmission solutions as well. The concept of HVDC transmission will be presented briefly, but this technology will not be used in simulations.
- Power converters and their control will not be included in the simulations.
- Cost aspects will not be studied in detail.
- For the modeling of the export cable, the SIMULINK library is limited to only a few cable models. The available models are the π-section model and the Bergeron distributed parameters model[3]. Additionally, the software tool does not allow editing of conductance[4], nor parameters regarding the physical geometry of the cable (conductor radius, positions, sheath configurations etc.).

1.6 Structure of the Thesis

Chapter 1 investigates the background of the given problem, and examines trends and developments regarding offshore wind farms in Europe. It also presents the current-day

[3] See section 3.2.
[4] Explained briefly in section 3.1.4.

technology for offshore wind power transmission, and explains the motivation of using LFAC as an alternative transmission technology.

Chapter 2 explains the concept of LFAC and investigates the impact of reducing the transmission frequency in the export cable, in addition to other selected components that are present in the transmission system.

Chapter 3 provides the necessary cable modeling theory, where several cable models are presented, explaining their strengths and weaknesses.

Chapter 4 describes a simplified offshore transmission system in steady state. The frequency response for various cable models are illustrated, and different cases regarding different cable lengths and inductive elements are studied.

Chapter 5 examines the effect of voltage rise over a lightly loaded/unloaded transmission cable, also known as the Ferranti effect.

Chapter 6 investigates the charging operation of an unloaded export cable with respect to the behavior of the charging currents and terminal voltages.

Chapter 7 examines various fault events in the system, distinguished by location and type. Firstly, the occurrence of a voltage sag/swell on the grid side of the power system will be studied. Finally, different short circuit faults occurring at the sending end (wind farm end) will be investigated. Additionally, the occurrence of DC components (DC offsets) posterior to certain fault events will be examined.

Chapter 8 concludes the thesis and proposes topics for further studies.

Chapter 2

Low Frequency AC in Transmission Systems

2.1 Transmission Technologies

For offshore installations, submarine cables must be used for power transmission. The transmission system can either be HVDC or HVAC, depending on the distance from the offshore wind farm to shore. In this section, the different technologies will be briefly presented in terms of their advantages and disadvantages.

HVAC

As the majority of wind farms located offshore have a distance to shore below 100 km, HVAC cables are mostly used to date. Up to a transmission distance of approximately 100-140 km, HVAC is still feasible before charging currents become too large for successful active power transmission. The charging currents are a result of energization/de-energization of the high capacitance in a transmission cable, and is given in eq. (2.1)[1] [18]:

$$I_c = \frac{V_n}{\sqrt{3}} 2\pi f C l \tag{2.1}$$

where V_n is the nominal phase-to-phase voltage, f is the system frequency, C is the capacitance per unit length and l is the total length of the cable.

The charging current contributes to a larger amount of reactive power produced by the cable, expressed by eq. (2.2). The increase of reactive power in turn decreases the active

[1] Derived in appendix A, section A.1.

power that can be transmitted by the cable.

$$Q_c = 3I_c \frac{V_n}{\sqrt{3}} = 2\pi f C l V_n^2 \tag{2.2}$$

Hence, the feasible transmission length is also dependent on the degree of reactive compensation, i.e. shunt reactors that consume reactive power. These can be installed in either end of the transmission cable, or both. In cases where compensation is needed mid-line, the costs of installing additional platforms will contribute in making HVAC transmission a less favorable solution [14]. As illustrated in fig. 2.1, the HVAC system does not require expensive frequency converter stations offshore/onshore, which is a huge advantage for this technology.

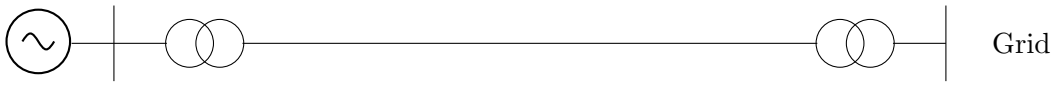

FIGURE 2.1: HVAC transmission system

HVDC

When the transmission distance exceeds a certain length, commonly referred to as the breakeven distance (BD), the use of HVAC becomes unfeasible due to high charging currents and cost for reactive compensation. See fig. 2.3. In such cases, HVDC is the preferred technology. HVDC cables do not suffer from capacitive charging currents($f = 0$ in eq. (2.1)), and can in theory be infinitely long. Additionally, high voltage levels can be used in HVDC transmission systems, as this will not contribute to any capacitive charging currents. This allows for large amounts of power to be transmitted over large distances. The major disadvantage for this kind of technology is the cost, as highly expensive offshore power converter platforms must be installed, see fig. 2.2.

FIGURE 2.2: HVDC transmission system

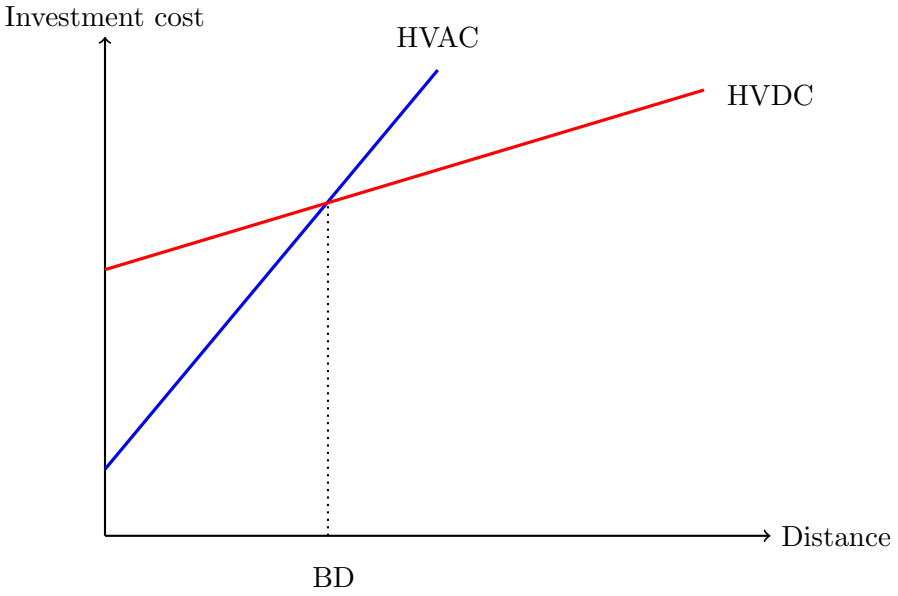

FIGURE 2.3: Breakeven distance (BD) for a conventional HVAC transmission system

The power converter technology used for HVDC power transmission purposes is divided in two main categories; the current source converters, also known as line commutated converters (LCC), and voltage source converters (VSCs). The LCC is a well known and established technology which primary use is to transfer bulk power over large distances, or to interconnect asynchronous AC systems. The LCC uses thyristor valves in its operation, and therefore rely on an external voltage source (from the AC network). The requirement of strong networks on either side of the converter makes the LCC unsuited for connection of offshore wind farms.

Opposed to the LCC, the VSC uses controllable switches which are independent of an external line voltage for commutation. The switches are insulated gate bipolar transistors (IGBTs) that can be switched on or off independently of the conducted current at the time. Being self commutating, the VSC does not require connection to a strong AC grid, making it suitable for integration of offshore wind farms. Additional characteristics and benefits are listed in table 2.1 [14][19][20].

TABLE 2.1: Characteristics of line commutated converter (LCC) and voltage source converter (VSC) technologies

	LCC	**VSC**
Filtering	Filters required to obtain a satisfactory sinusoidal on the AC side	Little filtering required, due to better approximation of the sinusoid at the AC side
Minimum power limit	Requires 5-15% of rated power	No theoretical limit
Power control	Always consumes reactive power	Independent control of both active and reactive power
Size	Demands a lot of space	Smaller footprint compared to LCC due to filters
Losses	Low switching losses	High switching losses due to high switching frequency. An MMC would have losses closer to LCC
Technology maturity	Well established, introduced in 1954	Introduced in 1997. Technology still in development, first commissioned for offshore wind purposes in 2015

2.2 LFAC Transmission

To deal with the shortcomings of conventional HVAC, and avoid the costly HVDC, the use of LFAC transmission has been proposed. The solution is based on HVAC, only with a lower transmission frequency compared to the conventional frequency of 50 (or 60) Hz. This results in lower charging currents (see eq. (2.1)), and allows for more active power to be transmitted from the wind farm to the main grid. Consequently, the feasible transmission distance will be longer compared to conventional HVAC.

Being AC-based, expensive frequency converter stations are avoided on the *offshore side* of the LFAC transmission system. It is however necessary to have a converter station onshore in order to transform the low transmission frequency to the grid distribution frequency. Although requiring an equal number of converter units in total, the LFAC transmission system allows for a lower installation and maintenance cost compared to an HVDC system. As a result, the breakeven distance is increased, illustrated in fig. 2.4. The initial costs for an LFAC transmission system is higher compared to conventional HVAC due to the frequency converters that must be installed. After a certain distance

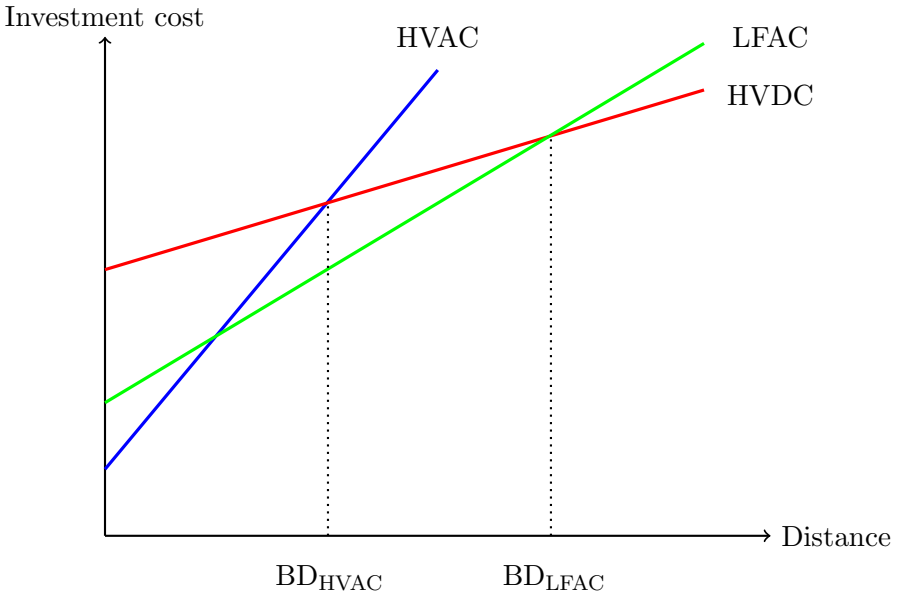

FIGURE 2.4: Breakeven distance (BD) for conventional HVAC versus LFAC transmission systems

the LFAC system becomes less expensive than HVAC, due to a lower amount of reactive compensation necessary. As the distance increases, LFAC will inevitably become more expensive compared to HVDC. It should be noted that fig. 2.4 is simply used for illustrative purposes, and does not reflect the exact relationship between the different transmission systems regarding costs and distance.

In the following sections, some of the components present in a power transmission system will be studied in brief with respect to LFAC transmission. In addition to the export cable, the transformer, frequency converter and switchgear will be examined.

2.2.1 Transformer

For a power transformer, the electro-magnetic force (emf) induced in the coils is given[2] as:

$$E = 4.4 f N_t A_c B \tag{2.3}$$

where N_t is the number of turns in the windings, A_c is the cross sectional area of the core, while B is the magnetic flux density. If the frequency is reduced and B is kept constant, the number of turns or the core cross section must be increased in order to maintain the same output voltage. This results in a weight and size increase of the transformer. A low frequency transformer operating at $16^2/_3$ Hz would be expected to double in weight and size compared to a 50 Hz transformer [21]. Considering the scarcity

[2]Derived in appendix A, section A.3.

of space on offshore wind installations, the volumetric increase of the transformer is a challenge. An alternative to placing the transformer in the turbine nacelle would be to install it in the tower structure of the wind turbine. Additionally, three single-phase units could be used to make transportation less cumbersome.

2.2.2 Frequency Converters

For an LFAC transmission system, the number of frequency converters necessary depend on the system design. For a wind farm where the turbines have a 50 Hz output from its back-to-back converters, offshore frequency converter stations must be installed to transform the frequency to the desired lower level before transmitting the power to shore (see fig. 2.5). At shore, the frequency must be transformed back to the grid frequency, and a new frequency converter is needed.

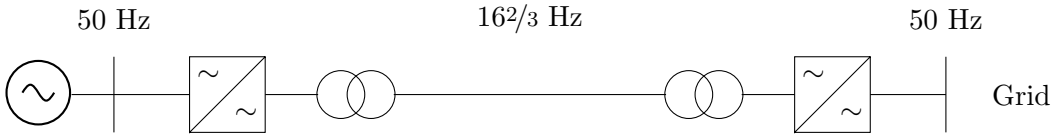

FIGURE 2.5: LFAC transmission system

The back-to-back converters in the wind turbines can be designed to produce a 16⅔ Hz output. Thus the offshore frequency converter station can be omitted, and only one shore-based converter station is necessary. This is illustrated in fig. 2.6. In addition to lowering the investment costs, this solution makes maintenance less complicated.

FIGURE 2.6: LFAC transmission system without offshore frequency converter station

Previous studies regarding LFAC transmission have proposed the use of cycloconverters for frequency conversion [22][23][24][25]. Being based on thyristors, the cycloconverter has no independent control of the reactive power or voltage capability, and the power factor is always lagging on the 50 Hz AC side. It therefore requires additional compensation and control systems. Additionally, studies have shown that the use of cycloconverters can lead to an increased amount of low order harmonics which need filtering [26].

More recent studies suggest that the transformation of frequency could be obtained through a back-to-back solution based on the MMC technology. The MMC offers independent control over reactive power, and the need for additional compensation is reduced. Filter requirements are lower compared to the cycloconverter, making the MMC station footprint smaller. The most prominent drawbacks are the need for numerous IGBT components, making the control system more complex. Additionally, the MMC technology is less mature compared to other frequency converters. For these reasons, it is an advantage to install an MMC converter station onshore, which is well suited for LFAC transmission systems [27][28].

2.2.3 Switchgear

Several European railway systems are operated at $16^2/_3$ Hz, which is a major advantage for choosing this particular frequency for the proposed LFAC transmission system. In german and swiss railway systems, SF_6 circuit breakers (CB) have been in commercial use for several years. The short circuit (SC) level in railway systems is higher compared to SC level in offshore systems, and interruption would thus be easier in an LFAC grid [21]. However, the low SC level introduces some drawbacks as it becomes more challenging to detect faults. As the voltage levels in the railway traction grids are small (usually 15 kV) compared to a power transmission system, the CBs must be modified and developed for higher voltages. Such technology modification needs to mature, and further research is necessary in order to optimize components for the use of LFAC power transmission.

2.2.4 Export Cable

Submarine export cables can be used without modification in LFAC transmission systems, and a reduction of the system frequency can be beneficial in terms of power transmission. Consider a lossless π-equivalent[3] of a transmission line/cable. The resulting equivalent circuit is shown in fig. 2.7.

[3]See chapter 3.

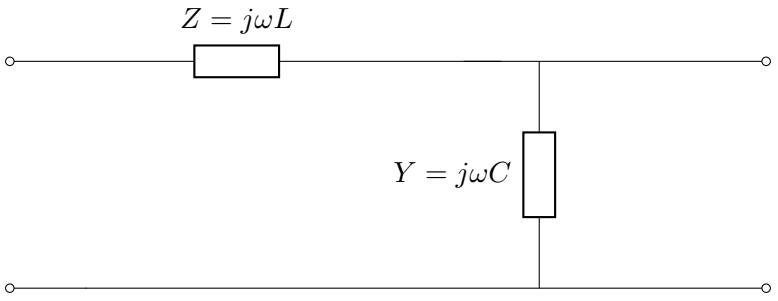

FIGURE 2.7: Circuit equivalent of a lossless transmission cable

The inductive and capacitive reactances per unit length become:

$$X_L = \omega L = 2\pi f L \tag{2.4}$$

$$X_C = -\frac{1}{\omega C} = -\frac{1}{2\pi f C} \tag{2.5}$$

where L and C are the inductance and capacitance per unit length, respectively. Reducing the transmission frequency results in a decrease in inductive reactance, while the capacitive reactance is increased. Both effects are beneficial:

- Low inductive reactance increases the active power flow.
- High capacitive reactance limits the capacitive charging currents in the cable, increasing the feasible distance of active power transmission.

The benefit of low inductive reactance can be explained by eq. (2.6), expressing the maximum active power[4] which can be transmitted across a line/cable.

$$P_R = \frac{V_S V_R}{X_L} \sin(\delta) \tag{2.6}$$

where V_S and V_R are the sending and receiving end voltages, respectively, and δ being the angle between the two. Inserting eq. (2.4) into (2.6), it is seen that the theoretical active power can be three times as high for a $16^2/_3$ Hz transmission system compared to a 50 Hz system. It should however be noted that eq. (2.6) is based on simplifications and assumptions that might not be valid for long subsea cables.

Another benefit of the LFAC system is the reduction of transmission losses, due to the lower resistance caused by the skin- and proximity effect[5].

[4] Derived in appendix A, section A.2.
[5] See chapter 3 for more details.

Chapter 3

Theory

3.1 Electrical Parameters of a Cable

Transmission cables can be treated as circuits with distributed parameters along the entire cable length. Figure 3.1 illustrates a per-phase equivalent for a transmission cable.

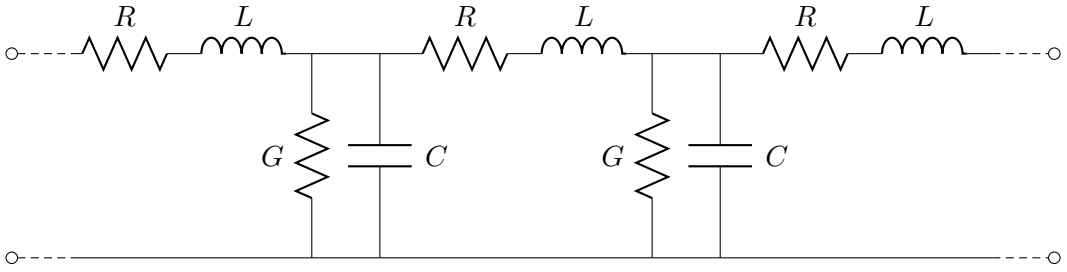

FIGURE 3.1: Electrical parameters per phase of a transmission line/cable

- R: Resistance per differential length [Ω/m]
- L: Inductance per differential length [H/m]
- C: Capacitance per differential length [F/m]
- G: Conductance per differential length [S/m]

3.1.1 Resistance

The DC resistance of a conductor is determined by the conductor cross-section and the electric resistivity of the conductor material:

$$R_{DC} = \frac{\rho}{A} \quad [\Omega/\mathrm{m}] \tag{3.1}$$

As the electric resistivity differs for varying temperatures, it is necessary to correct the DC resistance through eq. (3.2). The electrical resistivity is usually given at 20 °C, and must be corrected by a temperature coefficient.

$$R_{DC}(T) = R_{20\,^\circ\mathrm{C}}(1 + \alpha_T(T - 20)) \tag{3.2}$$

where $R_{20\,^\circ\mathrm{C}}$ is the DC resistance calculated for 20 °C, α_T is the temperature coefficient, and T is the temperature in the conductor during operation. For AC currents, one must take into consideration the *skin effect* and *proximity effect*, which both contribute to an increased resistance compared to DC currents. **Skin effect** is a result of electromagnetic induction, and results in a higher concentration of the AC current closer to the conductor surface as the frequency increases. This leads to a less effective utilization of the conductor cross section (decreasing the value of A in eq. (3.1)), and the resistance is increased. The **proximity effect** is a result of two or more AC current-carrying conductors close to one another. The AC current in one conductor induces eddy currents in the other conductor(s), opposing the original currents. This effect is also frequency dependent, and causes an increase of resistance as frequency increases.
For pipe-type cables commonly used for submarine power transmission, the resistance per unit length can be expressed by:

$$R = R_{DC}(1 + 1.5(y_s + y_p)) \quad [\Omega/\mathrm{m}] \tag{3.3}$$

where y_s and y_p are the *skin effect factor* and *proximity effect factor*, respectively. They are calculated by the equations (3.4) and (3.5).

$$y_s = \frac{x_s^4}{192 + 0.8x_s^4} \tag{3.4}$$

$$y_p = \frac{x_p^4}{192 + 0.8x_p^4}\left(\frac{\frac{r}{2}}{s}\right)^2 \left[0.312\left(\frac{\frac{r}{2}}{s}\right)^2 + \frac{1.18}{\frac{x_p^4}{192+0.8x_p^4} + 0.27}\right] \tag{3.5}$$

where

$$x_s^2 = \frac{8\pi f}{R_{DC}} 10^{-7} k_s \tag{3.6}$$

$$x_p^2 = \frac{8\pi f}{R_{DC}} 10^{-7} k_p \tag{3.7}$$

where k_s and k_p are constants determined by the conductor material and shape (both typically given values of 1.0) [29].

Fig. 3.2 shows the skin- and proximity effect factors as a function of frequency. It is seen that after approximately 20 Hz, the skin effect factor becomes more dominant than the proximity effect factor.

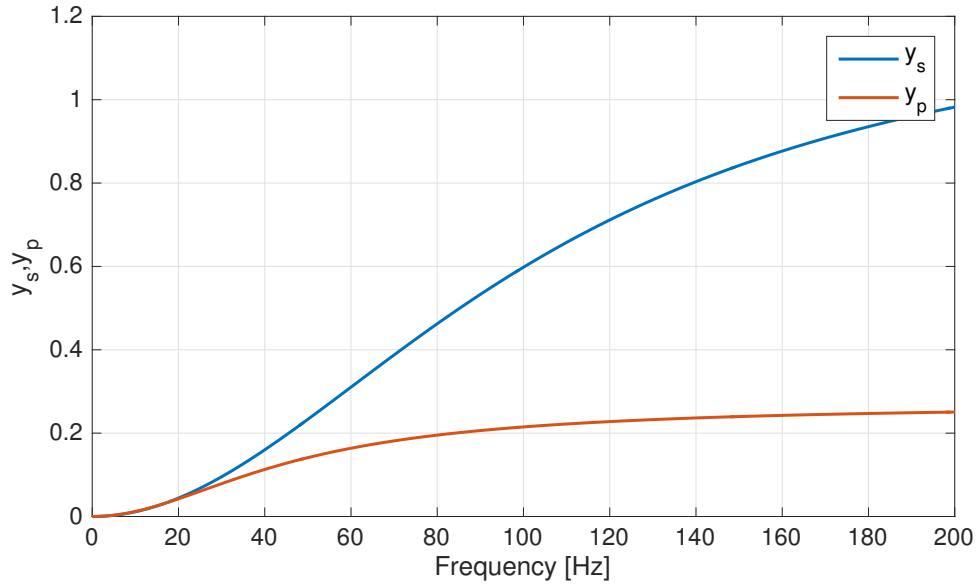

FIGURE 3.2: Skin effect factor and proximity effect factor for a 1000 mm^2 conductor. $\rho_{Cu} = 1.724 \times 10^{-8}$ Ωm, $k_s = 1$, $k_p = 1$

3.1.2 Inductance

The inductance is caused by the magnetic field surrounding the conductor(s) created by the current flowing in the cable, which in turn induces current in the opposite direction. Is can be expressed by:

$$L = \frac{\mu}{2\pi} \ln\left(\frac{D_e}{GMR}\right) \quad \text{[H/m]} \tag{3.8}$$

where μ is the permeability of the conductor, GMR is the geometric mean radius of the conductor, and D_e is the penetration depth of the earth. The latter is given by eq. (3.9), as a function of the earth resistivity and frequency:

$$D_e = 659\sqrt{\frac{\rho_{earth}}{f}} \tag{3.9}$$

3.1.3 Capacitance

For a coaxial transmission cable, the capacitance per unit length is obtained through eq. (3.10). This expression is valid for both low and high frequencies, i.e. the capacitance is not influenced by the distribution of the current in the conductor (skin effect) [30].

$$C = \frac{2\pi\epsilon}{\ln(\frac{r_2}{r_1})} \quad [\mathrm{F/m}] \tag{3.10}$$

where ϵ is the permittivity of the insulation, r_1 the conductor radius and r_2 is the radius over the insulation and semi-conducting layer (see figure 3.3).

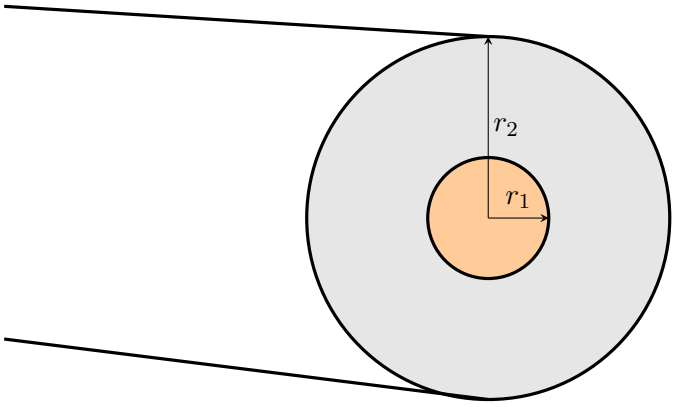

FIGURE 3.3: Cross-section of a single conductor

3.1.4 Conductance

The leakage current between the conductor and ground is represented by a conductance G, as the insulation does not represent an infinite impedance (although being very large, it is not ideal). Hence, the conductance represents the current generated from the conductor through the dielectric material to ground [31]. Similar to the capacitance, the conductance is not affected by the skin effect, and is obtained through eq. (3.11) (for a coaxial cable).

$$G = \frac{2\pi\sigma}{\ln(\frac{r_2}{r_1})} \quad [\mathrm{S/m}] \tag{3.11}$$

where σ is the conductivity of the dielectric of the insulation between the conductor and the outer screen.

3.2 Cable Modeling

There are several ways to model a transmission line/cable, and choosing the right model for simulation purposes depends on what is to be examined. The electrical parameters of the cable can be treated in different ways to create models suited for specific fields of study. There are two main categories in order to treat the cable's electrical parameters; lumped and distributed. Additionally, the parameters are either considered as being constant or frequency dependent. Models using constant parameters can be sufficient in steady state analysis where transient phenomena does not occur, and where the system is evaluated at a single frequency. For dynamic situations however, it is in many cases necessary to use models with frequency dependent parameters in order to obtain sufficient accuracy [31].

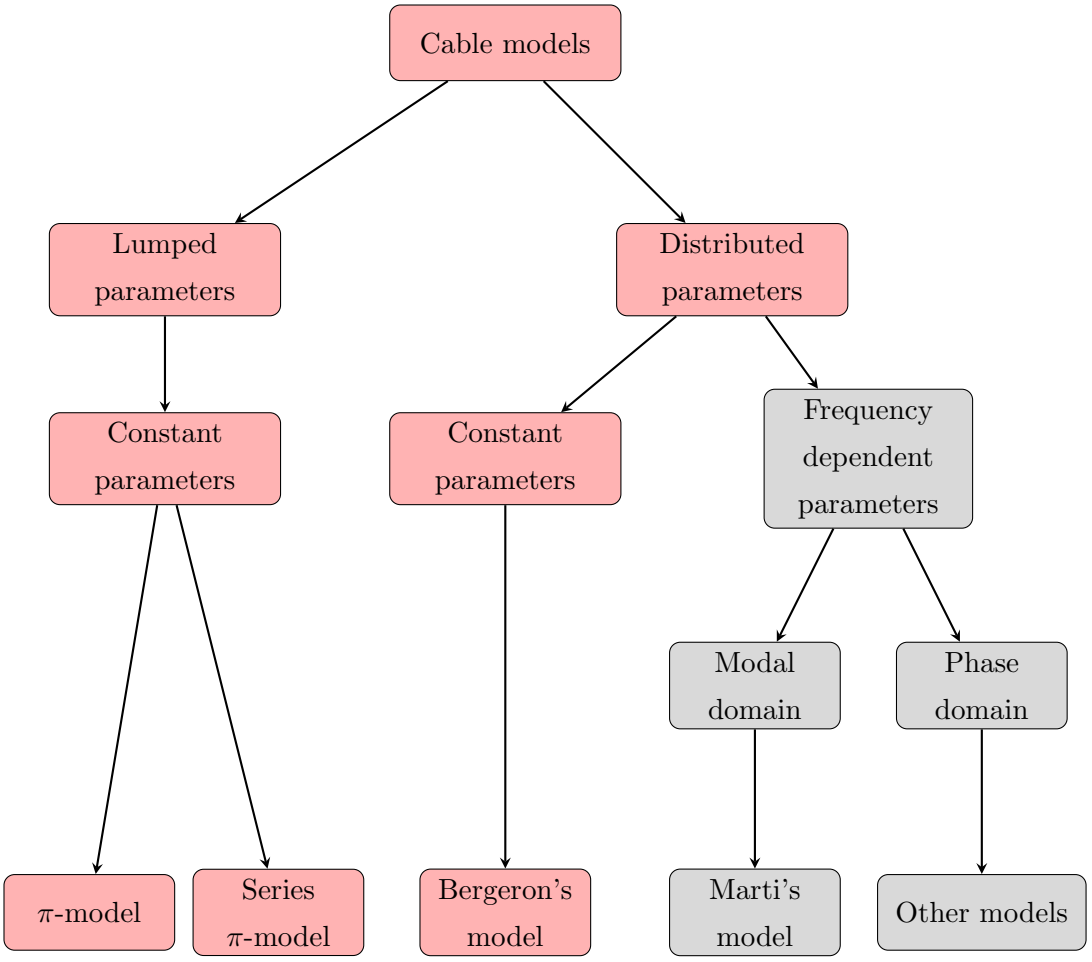

FIGURE 3.4: Model classification

Some of the various cable models found in literature can be seen in fig. 3.4. Among

these models, only the models marked in red will be subject to simulation[1] in this thesis. The remaining models are not used for simulations, and will only be presented briefly.

3.2.1 Time Domain

Models that belong to the time domain, do not use transforms (Fourier or Laplace) in order to obtain the solution [32]. Typical models that make use of the time domain include the lumped parameters models and the distributed, frequency dependent parameters models. Both will be investigated in greater detail in section 3.2.3 and section 3.2.4. These models usually make the assumption of lossless transmission, i.e. neglecting the resistance and/or conductance. In cases where the transmission distance is short, these assumptions can still provide results with sufficient accuracy.

If the electrical parameters in fig. 3.1 are considered to be distributed evenly throughout the transmission cable, the equivalent circuit can be illustrated according to fig. 3.5.

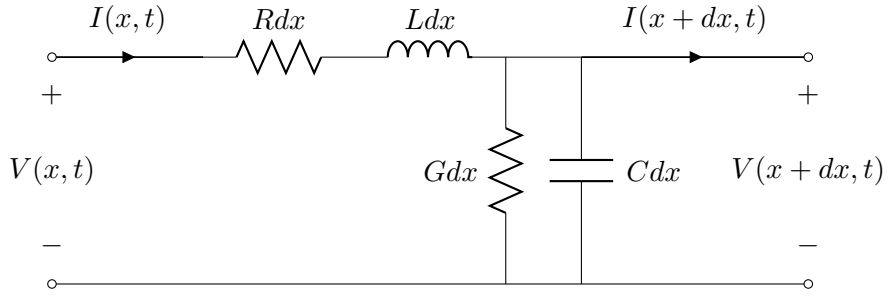

FIGURE 3.5: Circuit showing distributed parameters for a small differential length section

Using Kirchoff's voltage law (KVL) and Kirchoff's current law (KCL), the following equations can be derived:

$$V(x,t) - V(x+dx,t) = RdxI(x,t) + Ldx\frac{\partial I(x,t)}{\partial t} \tag{3.12}$$

$$I(x,t) - I(x+dx,t) = GdxV(x,t) + Cdx\frac{\partial V(x,t)}{\partial t} \tag{3.13}$$

If the cable is considered being lossless, $R = 0$ and $G = 0$.

$$V(x,t) - V(x+dx,t) = Ldx\frac{\partial I(x,t)}{\partial t} \tag{3.14}$$

$$\Leftrightarrow \frac{\partial V(x,t)}{\partial x} = -Ldx\frac{\partial I(x,t)}{\partial t} \tag{3.15}$$

[1] Limited to the SIMULINK Library. See chapter 4, 5 and 6

$$I(x,t) - I(x+dx,t) = Cdx\frac{\partial V(x,t)}{\partial t} \tag{3.16}$$

$$\Leftrightarrow \frac{\partial I(x,t)}{\partial x} = -Cdx\frac{\partial V(x,t)}{\partial t} \tag{3.17}$$

Eq. (3.15) and (3.17) are also known as the telegrapher's equations. They can be developed to:

$$\frac{\partial^2 V(x,t)}{\partial x^2} = -LC\frac{\partial^2 V(x,t)}{\partial t^2} \tag{3.18}$$

$$\frac{\partial^2 I(x,t)}{\partial x^2} = -LC\frac{\partial^2 I(x,t)}{\partial t^2} \tag{3.19}$$

The general solution for these equations is given by (3.20) and (3.21). Here, V^+/I^+ are the forward wave components of the voltage and current, while V^-/I^- are the backward wave components.

$$V(x,t) = V^+\big(t - \sqrt{LC}x\big) + V^-\big(t + \sqrt{LC}x\big) \tag{3.20}$$

$$I(x,t) = I^+\big(t - \sqrt{LC}x\big) + I^-\big(t + \sqrt{LC}x\big) \tag{3.21}$$

3.2.2 Frequency domain

Frequency-dependent models should be used whenever it is desirable to have a very accurate model, taking the variation of parameters with changing frequency into consideration. Models that are frequency dependent can either be represented in the phase domain or the modal domain, and they are valid for a larger range of frequencies compared to the constant parameter models. The resistance and conductance are not neglected, and hence both the propagation constant and the characteristic impedance are dependent on the frequency [33]. Thus, equations (3.12) and (3.13) can be represented in the frequency domain, shown below:

$$-\frac{dV(x,\omega)}{dx} = (R(\omega) + j\omega L(\omega))I(x,\omega) \tag{3.22}$$

$$-\frac{dI(x,\omega)}{dx} = (G(\omega) + j\omega C(\omega))V(x,\omega) \tag{3.23}$$

$$\frac{d^2V(x,\omega)}{dx^2} = \big(R(\omega) + j\omega L(\omega)\big)\Big(-\frac{dI(x,\omega)}{dx}\Big) \tag{3.24}$$

$$\frac{d^2I(x,\omega)}{dx^2} = (G(\omega) + j\omega C(\omega))\Big(-\frac{dV(x,\omega)}{dx}\Big) \tag{3.25}$$

$$\frac{d^2V(x,\omega)}{dx^2} = \big(R(\omega) + j\omega L(\omega)\big)\big(G(\omega) + j\omega C(\omega)\big)V(x,\omega) = zyV(x,\omega) = \gamma^2(\omega)V(x,\omega) \tag{3.26}$$

$$\frac{d^2I(x,\omega)}{dx^2} = \big(G(\omega) + j\omega C(\omega)\big)\big(R(\omega) + j\omega L(\omega)\big)I(x,\omega) = yzI(x,\omega) = \gamma^2(\omega)I(x,\omega) \tag{3.27}$$

where γ is known as the propagation constant, obtained by:

$$\gamma = \alpha + j\beta = \sqrt{(R + j\omega L)(G + j\omega C)} = \sqrt{zy} \tag{3.28}$$

The ordinary differential equations (ODE's) in eq. (3.26) and (3.27) have general solutions given by:

$$V(x,\omega) = A_1e^{-\gamma x} + A_2e^{\gamma x} \tag{3.29}$$

$$I(x,\omega) = B_1e^{-\gamma x} + B_2e^{\gamma x} \tag{3.30}$$

In the above equations, A and B are constants which can be found from initial conditions. The current can be expressed by the same constants as the voltage by using the relationship $I(x,\omega) = -\frac{1}{z}\frac{\partial V(x,\omega)}{\partial x}$. We have:

$$I(x,\omega) = \frac{1}{z}\gamma\big[A_1e^{-\gamma x} - A_2e^{\gamma x}\big] \tag{3.31}$$

$$I(x,\omega) = \frac{1}{z}\sqrt{zy}\big[A_1e^{-\gamma x} - A_2e^{\gamma x}\big] \tag{3.32}$$

The characteristic impedance is defined as:

$$Z_c = \sqrt{\frac{R + j\omega L}{G + j\omega C}} = \sqrt{\frac{z}{y}} \tag{3.33}$$

We then have:

$$I(x,\omega) = \frac{1}{Z_c}(A_1e^{-\gamma x} - A_2e^{\gamma x}) \tag{3.34}$$

By developing the equations using hyperbolic functions and boundary conditions, the following expressions for the receiving end voltage and current can be found. It is however important to remember that these equations are only accurate for a specific chosen frequency.

$$V_R(\omega) = V_S\cosh(\gamma(\omega)l) - Z_cI_S\sinh(\gamma(\omega)l) \tag{3.35}$$

$$I_R(\omega) = -\frac{V_S}{Z_c}\sinh(\gamma(\omega)l) + I_S\cosh(\gamma(\omega)l) \tag{3.36}$$

$$\begin{bmatrix} V_R \\ I_R \end{bmatrix} = \begin{bmatrix} \cosh(\gamma l) & -Z_c \sinh(\gamma l) \\ -\frac{1}{Z_c} \sinh(\gamma l) & \cosh(\gamma l) \end{bmatrix} \begin{bmatrix} V_S \\ I_S \end{bmatrix} \tag{3.37}$$

alternatively:

$$\begin{bmatrix} V_S \\ I_S \end{bmatrix} = \begin{bmatrix} \cosh(\gamma l) & Z_c \sinh(\gamma l) \\ \frac{1}{Z_c} \sinh(\gamma l) & \cosh(\gamma l) \end{bmatrix} \begin{bmatrix} V_R \\ I_R \end{bmatrix} \tag{3.38}$$

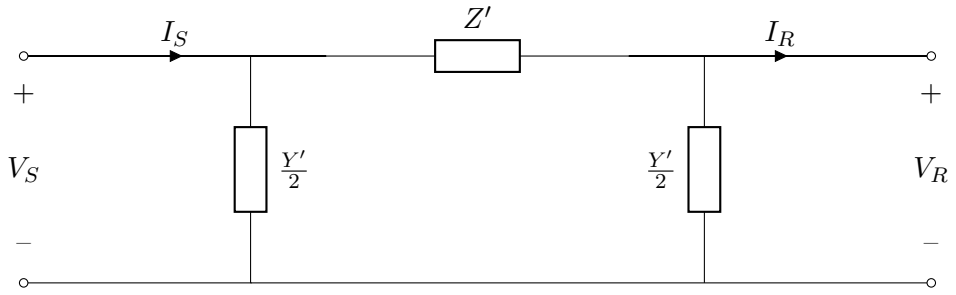

FIGURE 3.6: Equivalent model for a long line

$$Z' = (zl)\frac{\sinh(\gamma l)}{\gamma l} \tag{3.39}$$

$$Y' = (yl)\frac{\tanh(\gamma l/2)}{\gamma l/2} \tag{3.40}$$

3.2.3 Lumped Parameters

Using constant parameters, these models do not take into consideration the distributed manner of the electrical parameters, and the given RLC values per unit length are simply multiplied with the total length of the transmission cable. Additionally, these models are frequency-independent and do not take take into account the change of cable parameters when the frequency changes due to skin effect and proximity effect. Models using this approach include the π-models (single or series).

3.2.3.1 π-model

Also referred to as the *nominal* π-model, this model can be used for short transmission cables at steady state. The parameters are lumped, with the shunt capacitance divided equally and placed at each end of the cable, as illustrated in fig. 3.7.

Figure 3.7 can be represented by impedances and admittances. Z is the total impedance of the line, while Y is the total shunt admittance of the line. See figure 3.8.

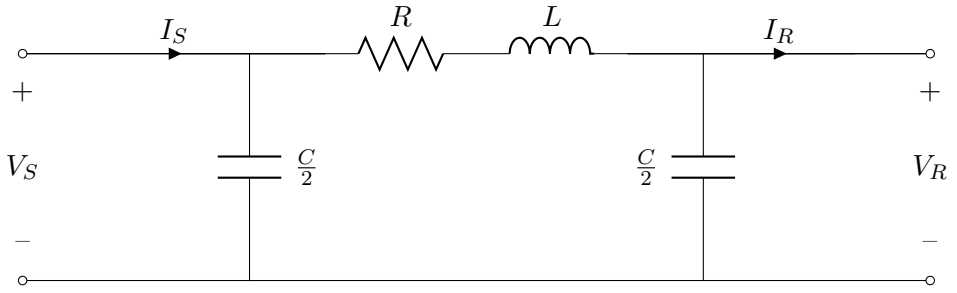

FIGURE 3.7: π-equivalent of a transmission cable

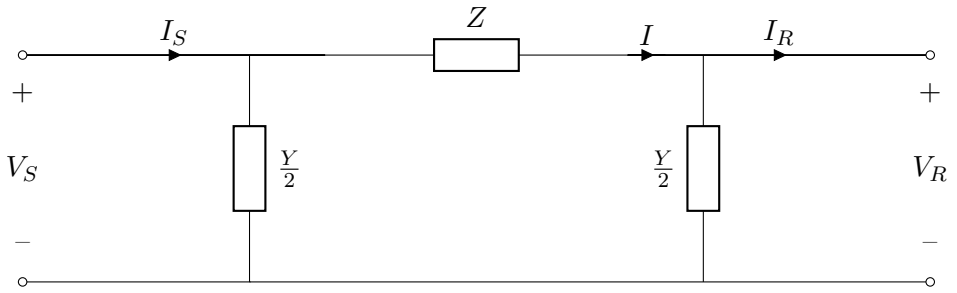

FIGURE 3.8: π-equivalent of a transmission cable represented by impedance and admittance

where

$$Z = (R + j\omega L)l \tag{3.41}$$

$$Y = (G + j\omega C)l \tag{3.42}$$

Expressions for the receiving end voltage and current can be derived by using KCL and KVL:

$$I = I_R + \frac{Y}{2}V_R \tag{3.43}$$

$$I_S = I + \frac{Y}{2}V_S \tag{3.44}$$

$$V_S = V_R + ZI \tag{3.45}$$

Inserting the expression for I in (3.45) gives:

$$V_S = \Big(1 + \frac{ZY}{2}\Big)V_R + ZI_R \tag{3.46}$$

We can now insert the expressions for V_S and I_L into (3.44):

$$I_S = Y\Big(1 + \frac{ZY}{4}\Big)V_R + \Big(1 + \frac{ZY}{2}\Big)I_R \tag{3.47}$$

The sending/recieving end voltages and currents is hence given by:

$$\begin{bmatrix} V_S \\ I_S \end{bmatrix} = \begin{bmatrix} A & B \\ C & D \end{bmatrix} \begin{bmatrix} V_R \\ I_R \end{bmatrix} \tag{3.48}$$

$$\begin{bmatrix} V_R \\ I_R \end{bmatrix} = \begin{bmatrix} D & -B \\ -C & A \end{bmatrix} \begin{bmatrix} V_S \\ I_S \end{bmatrix} \tag{3.49}$$

where

$$A = D = \left(1 + \frac{ZY}{2}\right) \tag{3.50}$$

$$B = Z \tag{3.51}$$

$$C = Y\left(1 + \frac{ZY}{4}\right) \tag{3.52}$$

Though giving satisfactory results for short cables, the single π-model is not suited for modeling long underground cables. In some cases, it might however be sufficient to cascade multiple π-sections to create the series π-model.

3.2.3.2 Series π-model

The π-circuit in figure 3.7 can be connected in series as illustrated in figure 3.9, creating the series π-model.

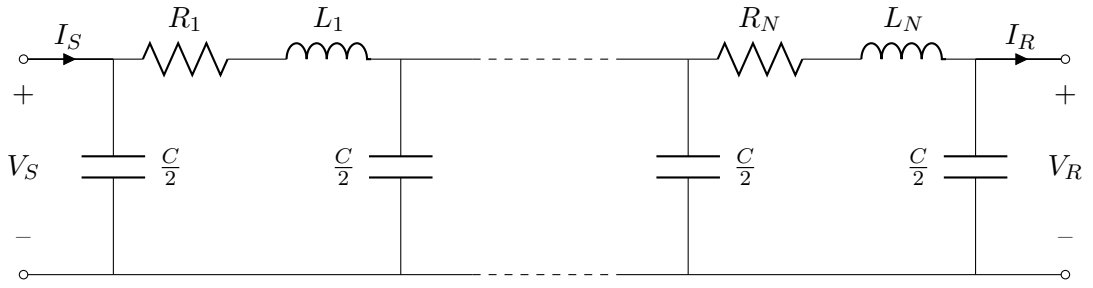

FIGURE 3.9: π-equivalent of a transmission cable in series

The maximum frequency that can be represented by a certain number of cascaded π-circuits is given in eq. (3.53) [34]. Table 3.1 shows the maximum frequency for a selection of series π-models.

$$f_{max} = \frac{N}{8l\sqrt{LC}} \tag{3.53}$$

where N is the total number of cascaded π-sections, l is the total cable length, while L and C are the cable inductance and capacitance per unit length, respectively.

TABLE 3.1: Frequency range for different series π-models
$l = 200$ km, $L = 25$ mH, $C = 183$ nF

	$N = 1$	$N = 10$	$N = 50$
f_{max}	76 Hz	764 Hz	3818 Hz

3.2.4 Distributed Parameters

When the transmission distance becomes very long, the parameters can no longer be considered to be lumped. Instead, distributed parameters are used, as seen in figure 3.10. Models utilizing this approach give a more accurate representation of the parameter's distributed manner in the transmission cable, and hence provide more accurate results. A common model using distributed parameters is the Bergeron model, based on traveling wave theory. This model is also used in simulation software such as SIMULINK.

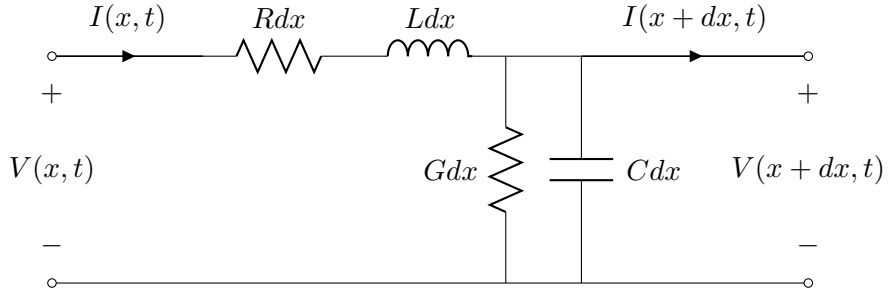

FIGURE 3.10: Circuit showing distributed parameters for a small differential length section

3.2.4.1 Bergeron's Model

In the Bergeron's model (traveling wave model), the parameters are considered as being distributed, except for the resistance which is lumped in the cable ends ($R/4$) and in the middle of the cable ($R/2$). Note that the conductance G is neglected. The model assumes that the quantity $e + Zi$ entering the sending end of the cable must arrive with a time delay, but unchanged, at the receiving end (see fig. 3.11) [35]. The time delay can be expressed by the following equation:

$$\tau = \frac{l}{v} = l\sqrt{LC} \tag{3.54}$$

where v is the propagation velocity of the traveling wave, defined by:

$$v = \frac{1}{\sqrt{LC}} \tag{3.55}$$

Table 3.2 shows the traveling time for different cable lengths.

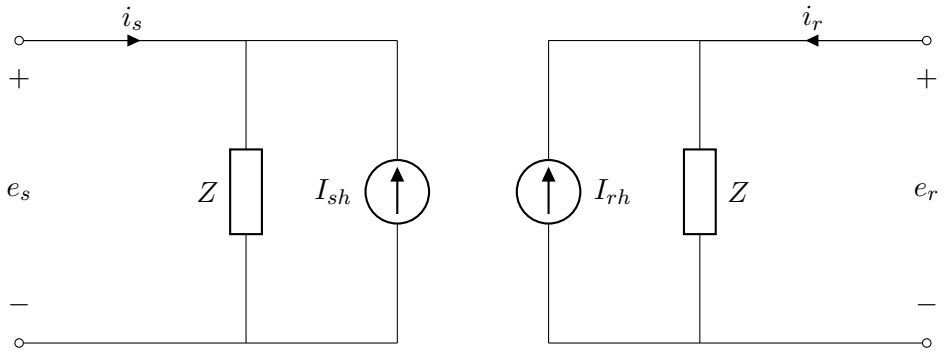

FIGURE 3.11: Bergeron's traveling wave model

Introducing the lumped resistances and the current injection method, we obtain:

$$I_{sh}(t) = \Big(\frac{1+h}{2}\Big)\Big[\frac{1}{Z}e_r(t-\tau) + hi_r(t-\tau)\Big] + \Big(\frac{1-h}{2}\Big)\Big[\frac{1}{Z}e_s(t-\tau) + hi_s(t-\tau)\Big] \quad (3.56)$$

$$I_{rh}(t) = \Big(\frac{1+h}{2}\Big)\Big[\frac{1}{Z}e_s(t-\tau) + hi_s(t-\tau)\Big] + \Big(\frac{1-h}{2}\Big)\Big[\frac{1}{Z}e_r(t-\tau) + hi_r(t-\tau)\Big] \quad (3.57)$$

where $Z = Z_c + \frac{R}{4}$ and $h = \frac{Z_c - \frac{R}{4}}{Z_c + \frac{R}{4}}$.

An equivalent circuit illustrating the distributed manner of the inductance/capacitance and the lumped resistance is shown in fig. 3.12

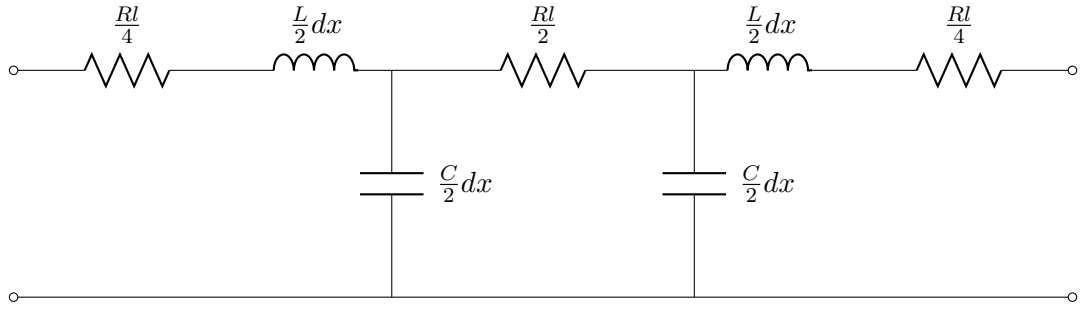

FIGURE 3.12: Equivalent circuit with distributed and lumped parameters in the Bergeron model

TABLE 3.2: Traveling time for different cable lengths, $L = 0.3661$ mH/km, $C = 183$ nF/km

	l = **150 km**	l = **200 km**	l = **250 km**	l = **300 km**
τ	1.23 ms	1.64 ms	2.05 ms	2.46 ms

Bergeron's model gives sufficient accuracy where the total resistance of the cable is significantly smaller than the characteristic impedance, i.e. $Rl << Z_c$ [36]. However,

the model is mainly recommended for use in cases where one specific frequency is under consideration. The propagation time of the traveling wave and the characteristic impedance is given as steady state values, and the model represents the fundamental frequency. Hence the model is not suited for rapid transient studies, and the utilization of frequency dependent models should be considered as an option [37].

3.2.4.2 Marti's Model

The Marti model is based on the Bergeron model, with some modifications. Firstly, the model is based on voltage sources instead of current sources, see figure 3.13. Secondly, it uses distributed parameters where the equations are developed in the frequency domain [31].

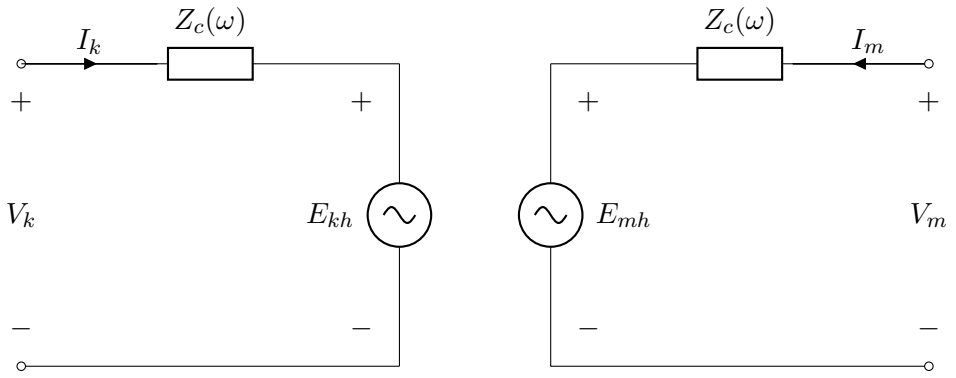

FIGURE 3.13: Marti's model

$$V_k(\omega) = Z_c(\omega)I_k(\omega) + E_{mh}(\omega) \tag{3.58}$$

$$V_m(\omega) = Z_c(\omega)I_m(\omega) + E_{kh}(\omega) \tag{3.59}$$

where

$$E_{mh}(\omega) = \big[V_k(\omega) + Z_c(\omega)I_k(\omega)\big]e^{-\gamma(\omega)l} \tag{3.60}$$

$$E_{kh}(\omega) = \big[V_m(\omega) + Z_c(\omega)I_m(\omega)\big]e^{-\gamma(\omega)l} \tag{3.61}$$

The above equations state that the quantities $V_{k/m} + Z_c I_{k/m}$ are transmitted to the cable end of length l according to the propagation function $e^{-\gamma(\omega)x}$ when $x = l$ [36]. The Marti model is not accurate at low frequencies, neither for lines/cables that are very short.

The flowchart in fig. 3.14 gives an indication of how to choose an appropriate model for transmission cables, taking into account the time step in the simulation software.

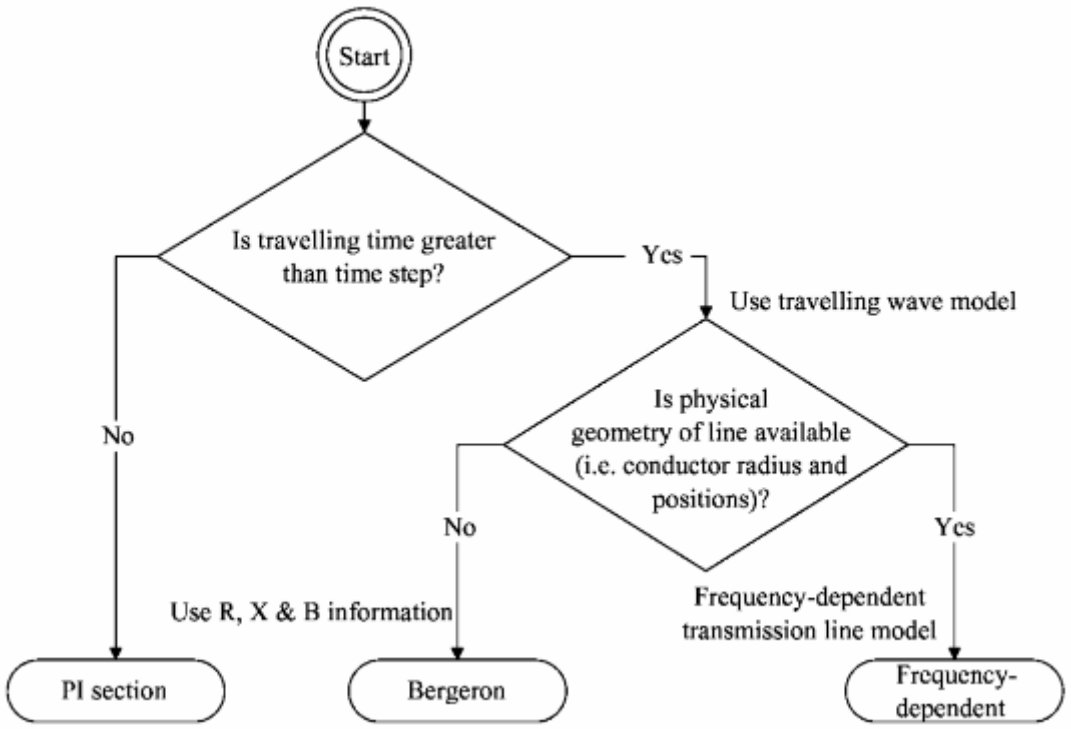

FIGURE 3.14: Selection of transmission line/cable model [38]

3.3 Ferranti Effect

When energizing an unloaded (or lightly loaded) transmission line, the capacitive charging current of the line becomes greater than the load, and the voltage increases along the cable. This effect is called the *Ferranti effect* and is more prominent in underground cables compared to overhead lines (OHLs). This is due to the high capacitance in cables, which can be 10-20 times larger than the capacitance of OHLs.

To illustrate, consider a lossless π-equivalent with the receiving end unloaded, see fig. 3.15. L and C are the inductance and capacitance per unit length respectively, while l is the total length of the transmission line. We have:

$$V_S - V_R = j\omega Ll \cdot I \tag{3.62}$$

Being unloaded, the expression for I becomes:

$$I = V_R \frac{j\omega Cl}{2} \tag{3.63}$$

$$\Leftrightarrow V_S - V_R = j\omega Ll \cdot V_R \frac{j\omega Cl}{2} = -V_R \frac{\omega^2 LCl^2}{2} \tag{3.64}$$

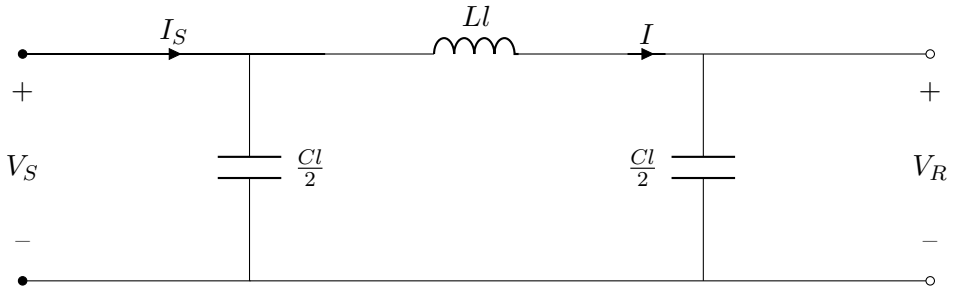

FIGURE 3.15: Unloaded transmission line

$$\Leftrightarrow V_R = V_S \frac{1}{1 - \frac{\omega^2 LCl^2}{2}} \tag{3.65}$$

The receiving end voltage increases with increasing frequency, inductance, capacitance and cable length. Hence, the Ferranti effect is more noticeable in cables than in OHLs. In practice, the effect will be slightly less than seen in (3.65), as the line/cable resistance will reduce the degree of voltage rise. To compensate for the Ferranti effect, shunt reactors can be employed. They are defined as inductive reactances whose purpose is to draw inductive current from the electrical system. The modeling of a shunt reactor can simply be done by connecting an inductance and a resistance in series [39][29].

Chapter 4

Frequency Analysis

4.1 System Description and Model Analysis

As the capacitance increases with the cable length, the problem of harmonic resonance becomes more prominent for long subsea cables, which can result in higher losses and cause damage to other power system components. It is therefore necessary to have knowledge of the resonant frequencies that are present in the power system, and thus prevent interference with other system components by installing harmonic filters. In addition to the cable itself, inductive transmission system components such as power transformers and shunt/smooting reactors influence the resonant frequency distribution, and should also be considered in the analysis [40].

In the following sections, the LFAC export cable will be examined in terms of its resonance frequencies for different system frequencies and cable lengths. Additionally, the impact on resonance frequencies by adding inductive elements to the system will be studied. The system to be investigated is shown in fig. 4.1, which for this chapter is a single-phase circuit. V_s, R_s and L_s represent the offshore wind farm (OWF), and it is assumed that the voltage is already converted by step-up power transformers (at the generating units and at the collecting point prior to the cable). It is also assumed that the frequency is converted from 50 Hz to $16^2/_3$ Hz in the turbines back-to-back converters. R_s and L_s therefore represent the resistance and inductance from the converters, transformers and collector cables in the OWF. V_s is an ideal voltage source in the SIMULINK library, set to produce 600 MW. The values are given in table 4.1.

An impedance measurement block is connected between the receiving end of the cable and ground. The impedance Z_2 in fig. 4.1 is defined in the Laplace domain as the

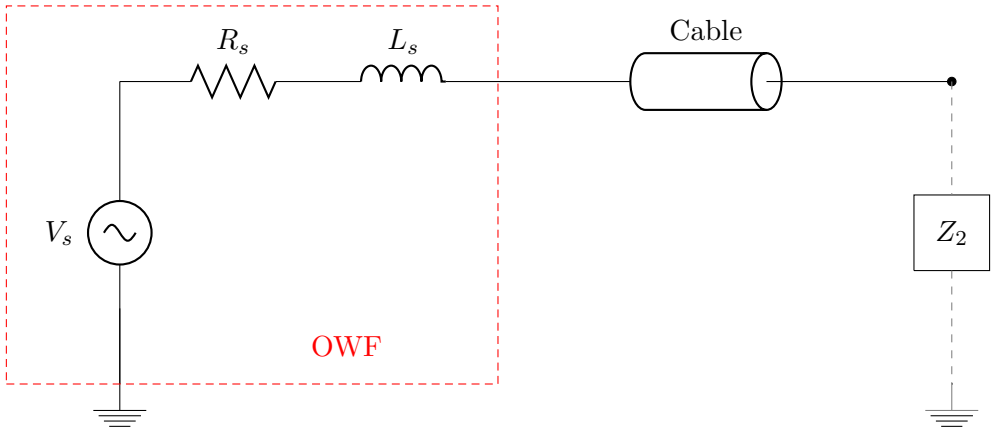

FIGURE 4.1: Circuit set-up for frequency analysis

transfer function between the current injected at the node and the voltage at the node:

$$Z_2(s) = \frac{V_2(s)}{I_2(s)} \tag{4.1}$$

If the analysis is performed through the state-space model, a current source with zero amplitude and nominal frequency can be placed in parallel with the impedance measurement block to provide the second input. Using the SIMULINK impedance measurement tool for the analysis, this action becomes redundant (the simulation results will be identical).

TABLE 4.1: Offshore wind farm (OWF) parameters

Parameters	**Values**
V_s	245 kV[1], 600 MW
R_s	1.0 Ω
L_s	0.1/25/100 mH

The export cable parameters are given in table 4.2 for LFAC and conventional HVAC (see [21]). The conductance is assumed to be negligible[2], the inductance and capacitance per unit length are assumed to be equal for both systems, while the resistance is slightly decreased in the LFAC system due to lower skin- and proximity effect. The cable can be modeled in various ways as described in chapter 3, depending on the case of study. This will be investigated in greater detail in section 4.2.

[1] Phase-to-phase RMS.
[2] In any case, SIMULINK does not include conductance in its line models.

TABLE 4.2: Parameters for a 245 kV, 1200 mm^2 Cu cable

Cable parameters	**HVAC**	**LFAC**
R	25 mΩ/km	17 mΩ/km
L	0.3661 mH/km	0.3661 mH/km
C	183 nF/km	183 nF/km

4.2 Export Cable Analysis

The inductance L_s at the OWF side is chosen to be very small (0.1 mH), and hence the parameters of the cable cable will be dominant in the following analysis. A comparison of the output impedance as a function of the frequency between different cable models is performed. The models examined are:

- Single π-model
- Series π-model, 10 sections
- Series π-model, 50 sections
- Distributed parameters model (DPM)

The results are shown in fig. 4.2. The DPM has an infinite number of resonant frequency peaks, and can therefore be used as a reference when analyzing the π-models (single and series) [35]. The models are accurate until the frequency response starts to deviate significantly from the DPM, as seen in fig. 4.2. Also, the maximum frequencies that can be represented by two of the π-models can be identified, being the frequency at which the last impedance peak occurs. The maximum resonant frequency for the 50-section model can not be identified from fig. 4.2, and is found by simulating over a wider frequency range. The models degree of accuracy and maximum resonant frequency is summarized in table 4.3.

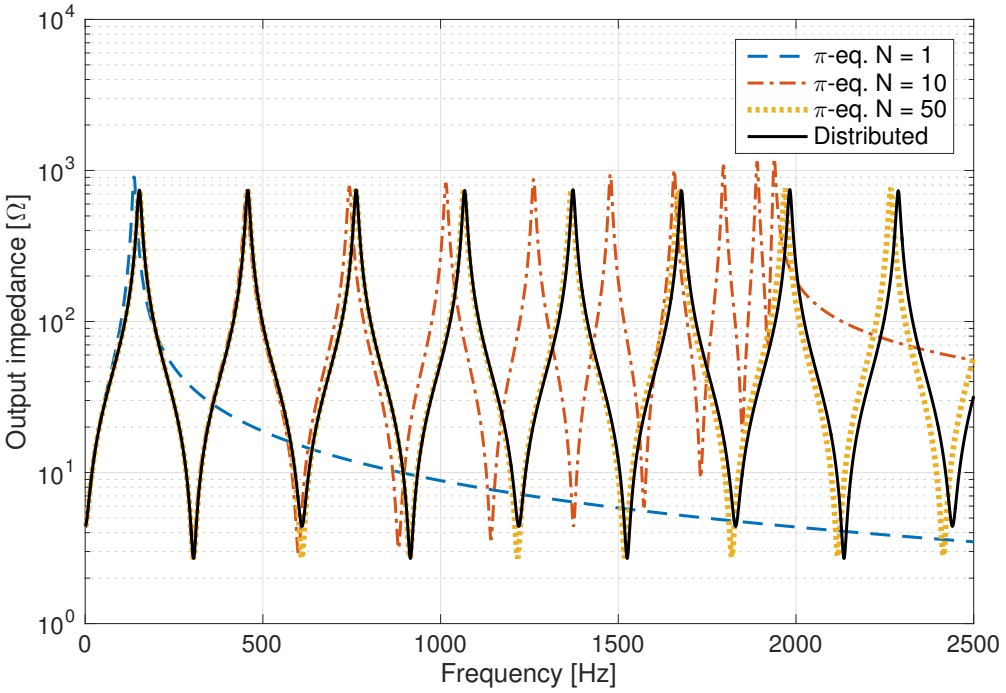

FIGURE 4.2: Frequency response different cable models. l= 200 km, L_s = 0.1 mH

TABLE 4.3: Frequency range of different series π cable models. l = 200 km, L_s = 0.1 mH

	$N = 1$	$N = 10$	$N = 50$
High degree of accuracy up to [Hz]	42	330	595
Approximate accuracy up to [Hz]	100	700	2200
Resonant frequencies up to [Hz]	138	1940	9722

The high degree of accuracy is identified by studying the different π-models relatively to the DPM for smaller frequency intervals, and observing at which frequencies the models start deviating $\sim$1 Ω[3] from the DPM. Approximate accuracy is found by studying fig. 4.2, observing where the π-models start to differ significantly from the DPM reference.

Note that although some of the models are valid up to relatively high frequencies, it does not imply that they are accurate for the respective frequencies. Comparing the results with the theoretical values for f_{max} in table 3.1, it is seen that the approximate frequencies in table 4.3 coincide the most. This shows that although eq. (3.53) gives

[3]See fig. B.1 in appendix B.

a certain perception of the different π-models frequency range, it should not be used uncritically when a high degree of accuracy is desirable.

When operated in steady state, the frequency of a power transmission system is relatively low ($16^2/_3$ / 50 / 60 Hz). From table 4.3, a single π-section model would suffice for steady state analysis, giving an acceptable amount of accuracy. Alternatively, one could cascade several π-models and obtain an even higher level of accuracy. Such models would also give the opportunity to analyze low-frequency transients, which could be caused by harmonic interference between system components.
In a transmission system there are numerous dynamic events that might cause transient behavior for voltages and currents. Depending on the event (switching operations, faults, sudden loss of load etc.), the frequency of the transients may vary from a couple of hundred Hz to several kHz. In order to be able to analyze the system for such events, it is desirable to use a cable model with a large frequency range. From fig. 4.2 and table 4.3 it is evident that the distributed parameters model is the most suitable model for a cable under dynamic conditions. In order to obtain accurate results for a wide frequency range, the **DPM** will be used in the following simulations regarding frequency analysis. For this model, the first resonant frequency can be obtained from:

$$f_1 = \frac{1}{4\tau} = \frac{1}{4l\sqrt{LC}} \tag{4.2}$$

and the next frequencies for the DPM can be found from eq. (4.3) [35].

$$f_{n+1} = f_1 + 2nf_1 \quad , \quad (n = 1, 2, 3...) \tag{4.3}$$

The first maximum is found at 153 Hz as seen in fig. 4.3, which is consistent with eq. (4.2) using the parameters in table 4.2. This frequency is close to the 9th harmonic for an LFAC system (3rd harmonic for a 50 Hz system), with a corresponding impedance of 740 ohms.

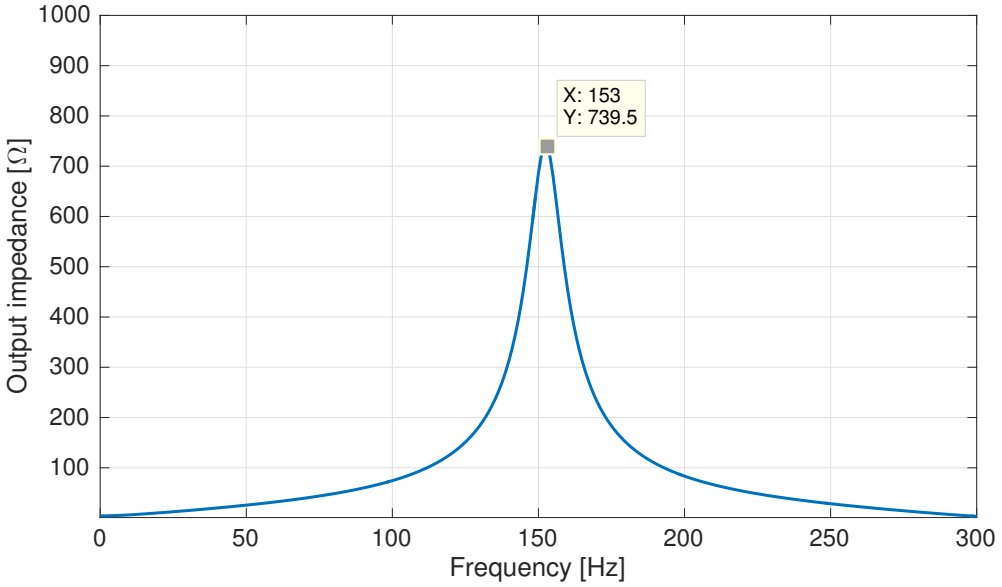

FIGURE 4.3: First frequency mode for the DPM. $l = 200$ km, $L_s = 0.1$ mH

4.2.1 Impact of System Frequency

The first frequency mode for an LFAC cable compared to a conventional HVAC cable can be seen in fig. 4.4. The change of system frequency results in the same resonant frequencies, but with different corresponding output impedance. In both systems, the first frequency mode is found at 153 Hz. This is expected as the inductance and capacitance are assumed to be equal for both systems. Only the resistance is considered being different (lower for LFAC), which results in a lower impedance at the resonant frequencies for the HVAC system due to a higher degree of damping.

At steady state, the impedance is higher for the HVAC system compared to the LFAC system. From fig. 4.4, the single-phase impedance seen from the receiving end of the cable is approximately 10 ohms for the LFAC system and 26 ohms for the HVAC system, exceeding the former by a factor of almost 3. This seems reasonable with regards to eq. (2.4), indicating that the inductive reactance in theory should be three times higher for the HVAC cable.

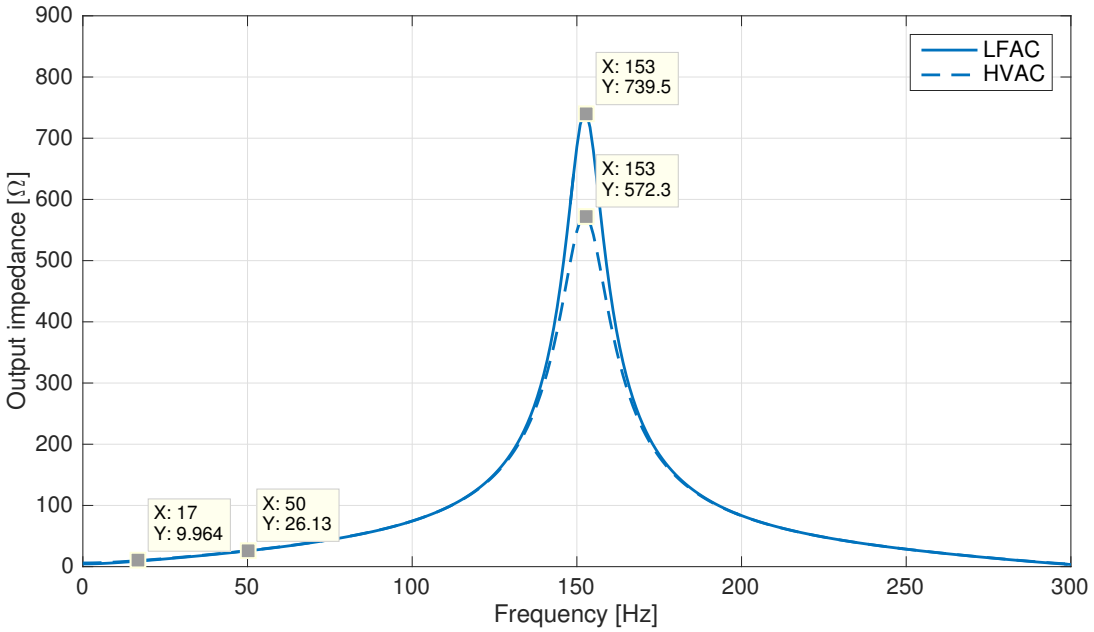

FIGURE 4.4: First frequency mode for the DPM for LFAC and HVAC. l = 200 km, L_s = 0.1 mH

4.2.2 Impact of Cable Length

Fig. 4.5 depicts the the impedance versus frequency for different cable lengths. It can be observed that the resonant frequencies become lower as the cable length is increased, which can be explained by the increased capacitance and inductance. The resonant peaks occur more frequently as the cable length increases, which is consistent with eq. (4.2) and eq. (4.3). The impedance at the resonant frequencies decrease as the cable length increases. This can be explained from the increasing total resistance in the export cable, leading to higher damping. When the cable length is increased to 300 km, the first mode occurs at 102 Hz (see fig. 4.6). In a 100 km cable, the first resonant frequency appears at 304 Hz. The values can also be calculated from eq. (4.2).

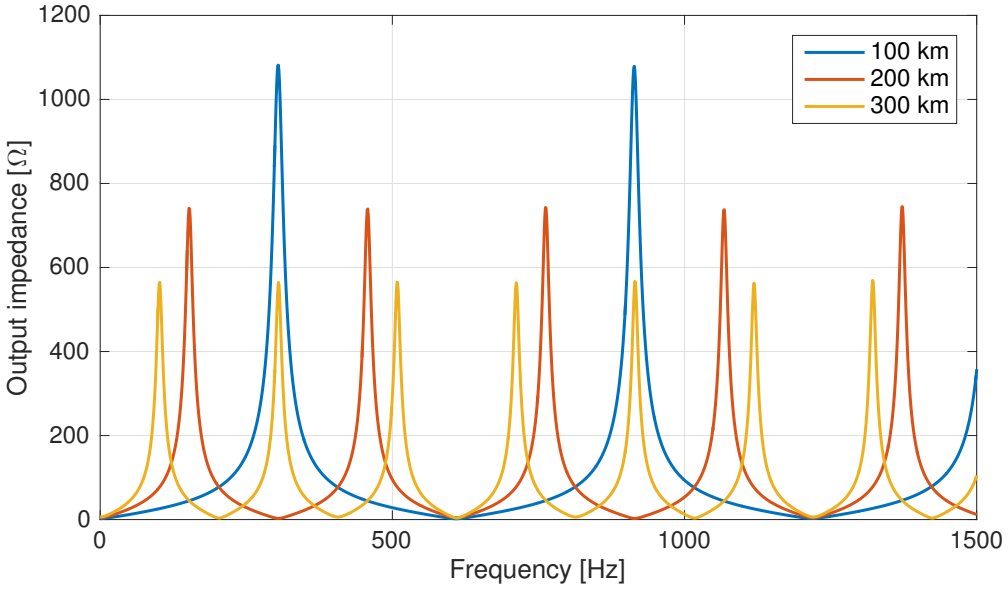

FIGURE 4.5: Resonant frequencies for different cable lengths. $L_s = 0.1$ mH

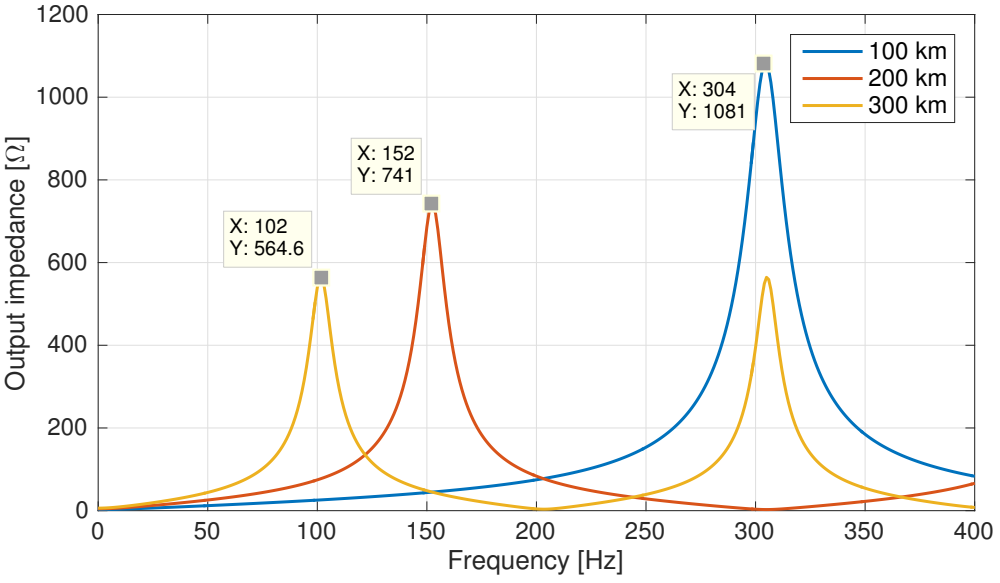

FIGURE 4.6: Closeup showing the first resonant frequencies for different cable lengths. $L_s = 0.1$ mH

4.3 Wind Farm Side Inductive Elements

In the following section, the influence of increasing inductance at the sending end of the export cable will be examined. Transformers, smoothing reactors, collecting cables etc. can be sources to higher inductance at the OWF side of the transmission system. In fig. 4.1, this is represented by the inductance L_s. In the previous section, L_s was

kept very small in order to observe the frequency response of the cable without external influence from other components. In the following, two cases will be presented where L_s is increased, each representing medium and high inductance at the OWF:

- Case 1: $L_s = 25$ mH
- Case 2: $L_s = 100$ mH

Case 1 - Medium Wind Farm Inductance

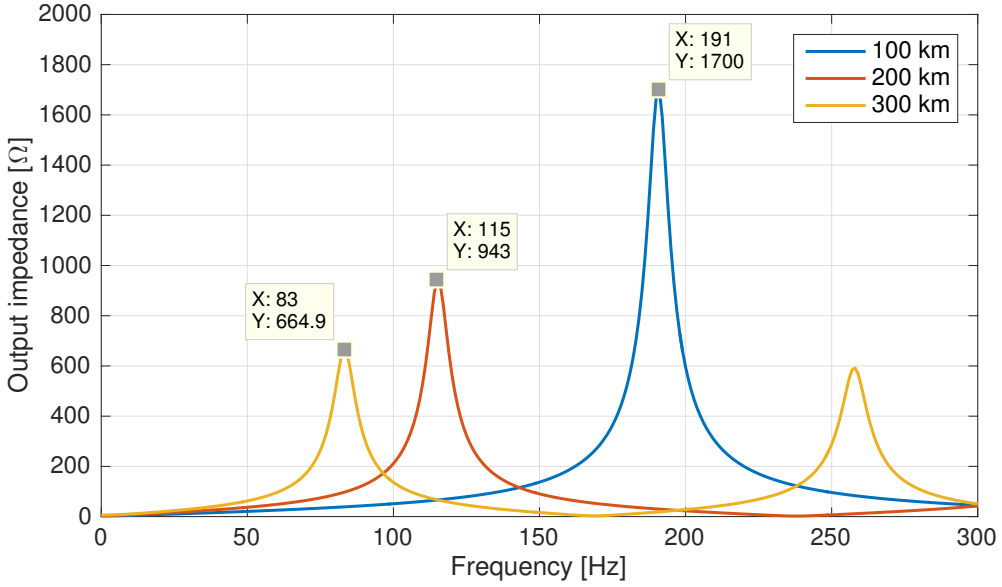

FIGURE 4.7: Output impedance vs. frequency for diffrent cable lengths. $L_s = 25$ mH

From fig. 4.7, resonance peaks are identified close to the 5th, 7th and 11th harmonic of the LFAC fundamental frequency. The resonant frequencies are found at lower frequencies compared to the previous cases, the lowest being below 100 Hz.

Case 2 - High Wind Farm Inductance

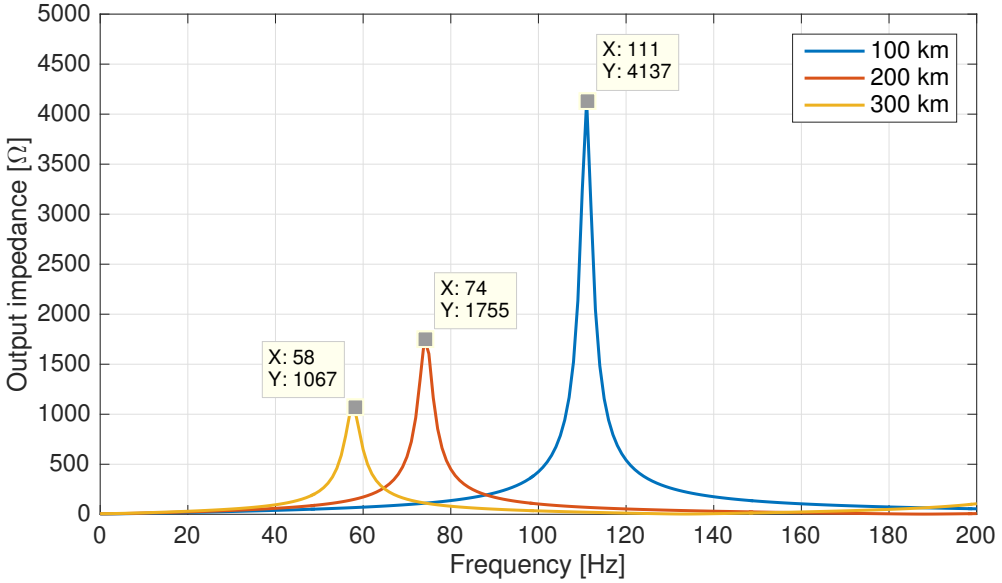

FIGURE 4.8: Output impedance vs. frequency for diffrent cable lengths. $L_s = 100$ mH

Resonance peaks are identified close to the 3rd, 5th and 7th harmonic of the LFAC fundamental frequency.

Case comparison

The first and second resonant frequenceis are shown in fig. 4.9 for the different values of L_s. It is observed that the resonant frequencies decrease with increasing inductance. However, opposite to the case of increasing the cable length, the corresponding output impedance increases.

The results from the preceding analyses are summarized in table 4.4. It can be seen that different combinations of inductance at the OWF side and export cable length may result in various low-order resonance frequencies. This may cause the following problems in the system:

1. Amplification of background harmonic distortion caused by other power system components. The result can be heavily distorted voltage and current signals in the transmission system.

2. Amplification of transient signals, leading to possible overvoltages/overcurrents which can damage components and personel.

3. Interaction with turbine regulators.

It is therefore necessary to take measures in order to minimize the risks connected to the scenarios listed above, e.g. installation of filters designed for the most critical harmonic frequencies. Filter design for LFAC transmission systems are not included in the scope of this thesis, and could be an interesting topic for further studies.

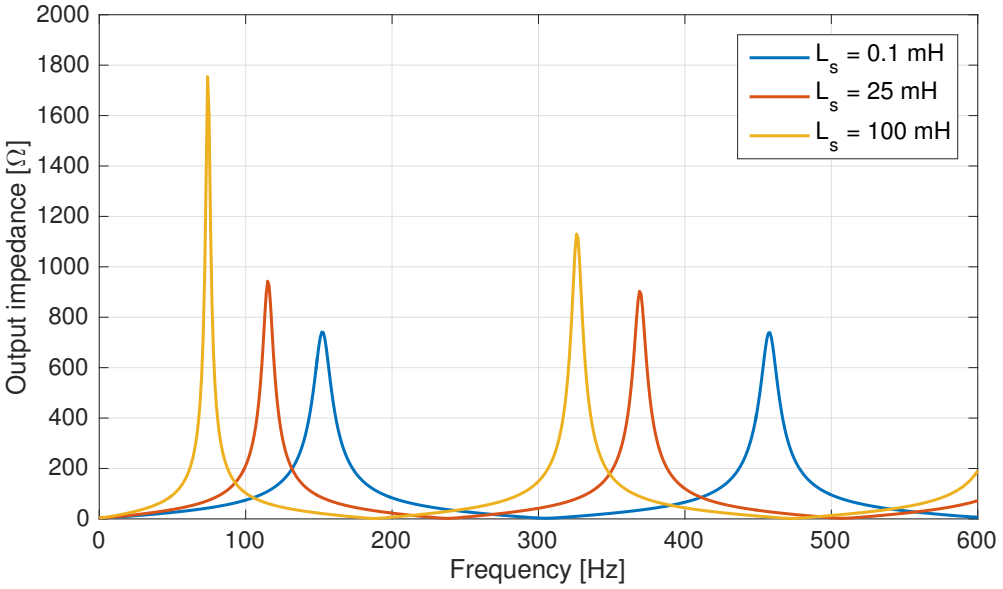

FIGURE 4.9: First and second resonant frequencies for different values of L_s. $l = 200$ km

TABLE 4.4: First resonant frequencies with corresponding impedance for the different cable lengths and OWF side inductances

Cable length [km]	**Source inductance [mH]**	**First frequency mode [Hz]**	**Impedance [ohm]**
100	0.1	304	1081
	25	191	1700
	100	111	4137
200	0.1	153	739.5
	25	115	943
	100	74	1755
300	0.1	102	564.6
	25	83	664.9
	100	58	1067

Chapter 5

Ferranti Effect

5.1 System Description and Model

This chapter aims to study the Ferranti effect in an LFAC system. The Ferranti effect results in a voltage rise in a transmission system which *a*) is lightly loaded or unloaded; *b*) consists of very long transmission lines or cables; or *c*) a combination of the two. Due to the higher capacitance for a subsea cable compared to an overhead line (OHL), the Ferranti effect will be more intense in the former[1]. It is therefore necessary to investigate to what extent the voltage can increase in a power system where a sudden disconnection or loss of load occurs. Having knowledge of the magnitude of a voltage rise caused by the Ferranti effect can be helpful when taking measures to reduce the risk of damage to personnel and/or power system components.

The analysis will be made for a both LFAC and conventional HVAC for comparison. Fig. 4.1 shows the system on which the simulations are performed. Note that the OWF inductance is not included in this chapter ($L_s = 0$), in order to examine the properties of the export cable without external interference. The other parameter values are equal to those listed in table 4.1 and table 4.2 in chapter 4.

[1]From eq. (3.65), large C leads to a higher voltage rise.

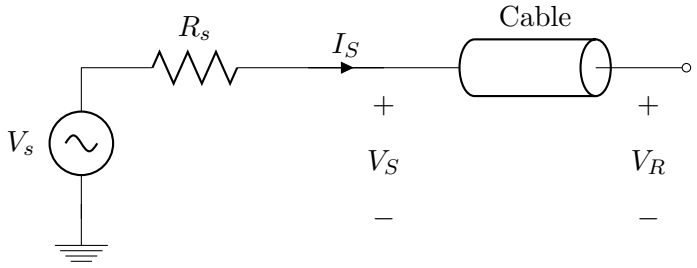

FIGURE 5.1: Ferranti effect analysis set-up for an unloaded system

For the simulations, three-phase π-section blocks in series are used. As the analysis is based on a power system in steady state, there will be no difference in the results if the distributed parameters line model were to be used. A three-phase series π-model in SIMULINK requires a new block to be added for every π-section, which makes it more convenient in terms of measuring the voltage along the cable.

5.2 Voltage Along the Cable

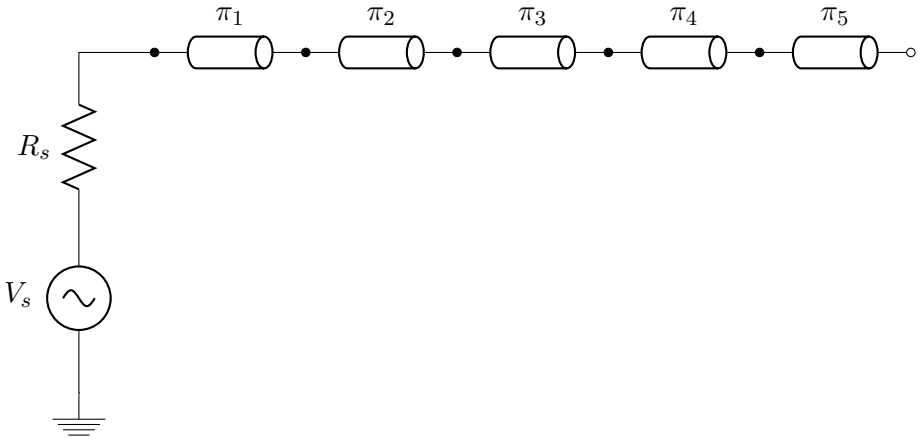

FIGURE 5.2: Circuit set-up for measurement of voltage along the export cable. Nodes indicate points of measurement

Each π-section were initially set to 40 km, simulating a 200 km cable. Measurements were performed between each section in addition to the sending and receiving end of the cable, simulating both an LFAC and an HVAC cable. The distribution of voltage along the cable is shown in fig. 5.3, along with limits indicating 5% and 10% voltage increase. Here, the 5% limit indicates a moderate overvoltage, whereas the 10% limit is treated as a high overvoltage. It can be observed that the Ferranti effect is far more prominent for a conventional HVAC cable than for an LFAC cable. At approximately

40 km, the voltage increases 5% above its rated value. At about 90 km, it reaches 10%. The voltage profile in the LFAC cable is kept under both of these limits along the entire cable length.

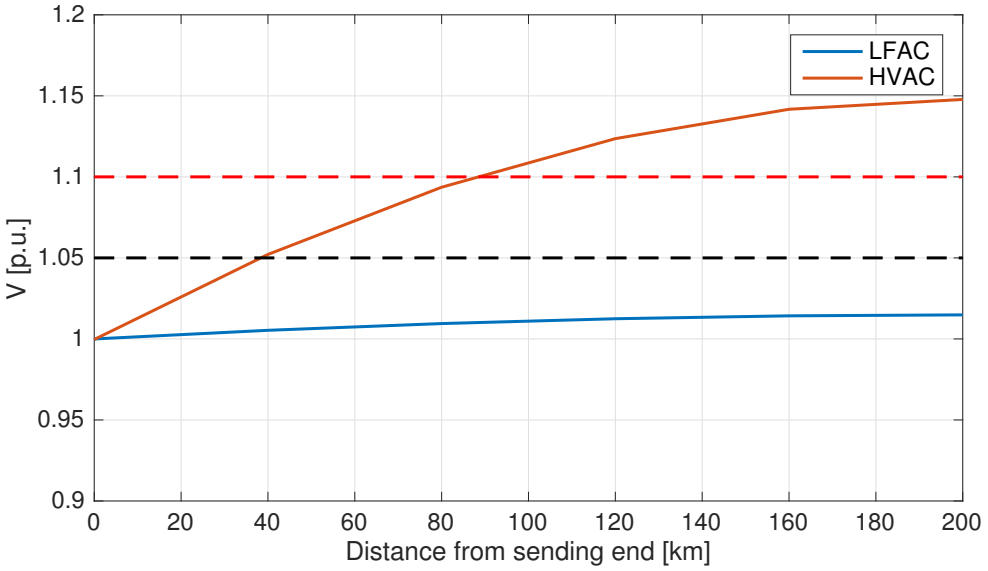

FIGURE 5.3: Voltage profile along a 200 km long cable. The black and red dashed lines indicate 5% and 10% overvoltage limits, respectively

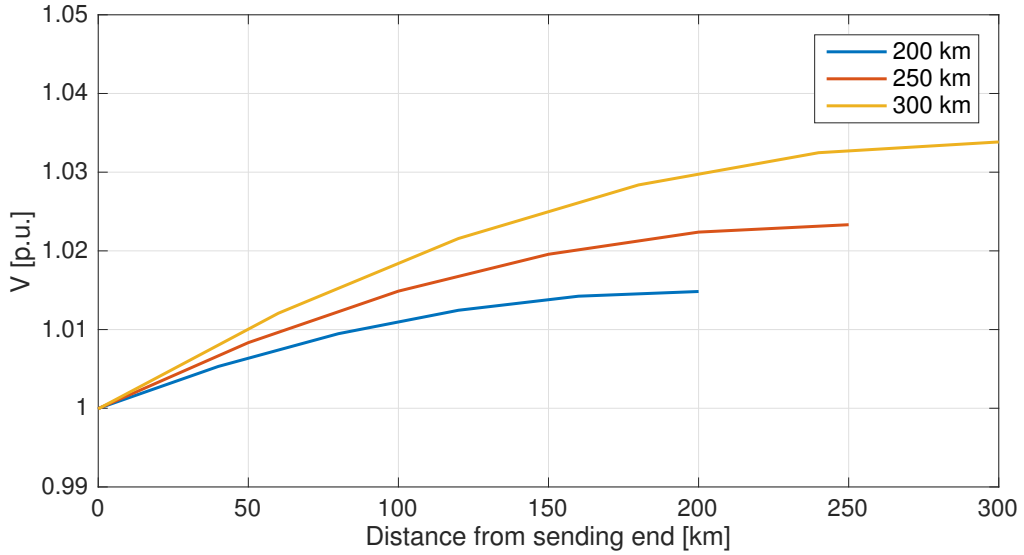

FIGURE 5.4: Voltage profile along LFAC cables with different cable lengths

Fig. 5.4 shows the voltage profile for different cable lengths. Five π-sections were used for all simulations, with 50 km per section for the 250 km cable, and 60 km for the 300 km cable. It is observed that even for very long cables exceeding 200 km, the Ferranti effect does not cause significant high voltages along the cable. By increasing the cable

length to 250 km and even 300 km, it can be observed that the voltage is kept within acceptable limits, i.e. the rise is below 5%. This is shown in fig. 5.4.

5.3 Receiving End Voltage

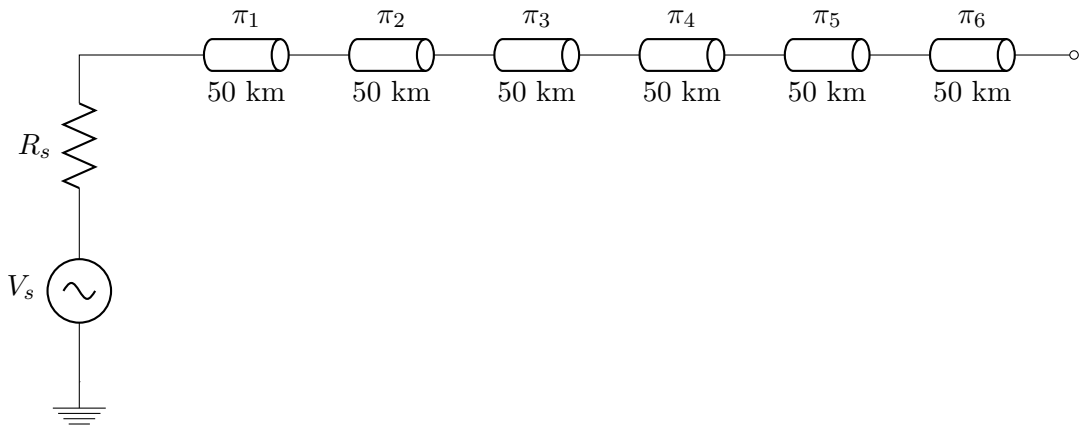

FIGURE 5.5: Circuit set-up for measurement of receiving voltage as a function of cable length

The receiving end voltage was measured as a function of the total cable length. This was done by using π-sections of length 50 km, and adding a new section between each simulation up to a total length of 300 km, see fig. 5.5. The result is shown in fig. 5.6. The LFAC cable shows satisfactory results, as V_R only increases by 1.5% for a 200 km cable and 3% for a 300 km cable. For conventional HVAC, V_R experiences an increase of 5% at 120 km, and 10% at 170 km.

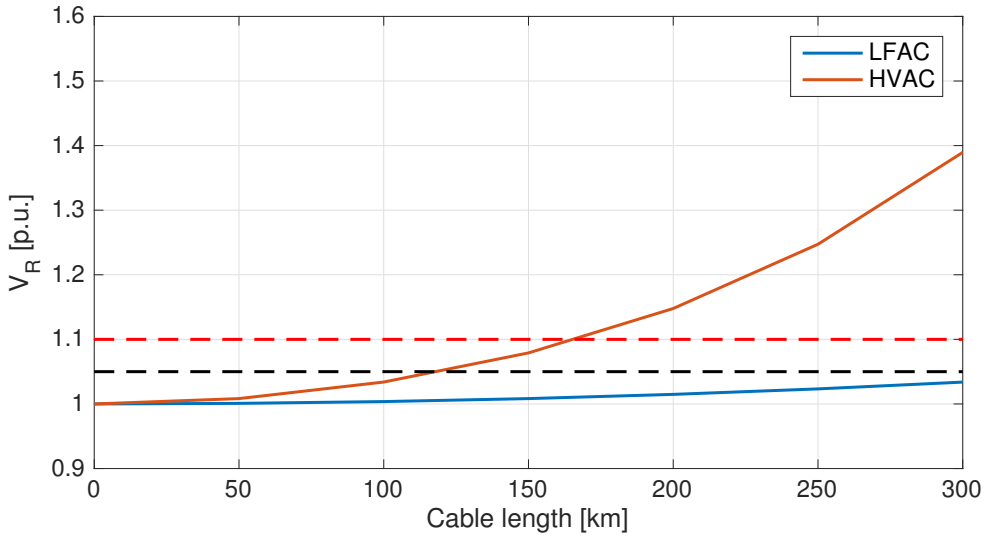

FIGURE 5.6: Receiving end voltage as a function of the total cable length.The black and red dashed lines indicate 5% and 10% overvoltage limits, respectively

TABLE 5.1: Percentage voltage increase for different cable lengths

	100 km	**150 km**	**200 km**	**250 km**	**300 km**
LFAC	0.4%	0.8%	1.5%	2.3%	3.4%
HVAC	3.4%	7.9%	14.8%	24.7%	38.9%

The voltage rise for the HVAC cable is very high, which is unexpected due to the higher resistance in the transmission system. The cable resistance has seemingly very little influence on the damping of the Ferranti effect, and one could suspect that losses were neglected in the simulation. Fig. 5.7 shows the same measurements together with the lossless theoretical values calculated from eq. (3.65), which confirms a small amount of damping for the HVAC cable. For the LFAC cable, the difference between theoretical lossless calculations and the simulated result is negligibly small. To examine whether the results were caused by a model error, the simulations were repeated using the DPM instead of cascaded π-sections. However, the same measurements were obtained.

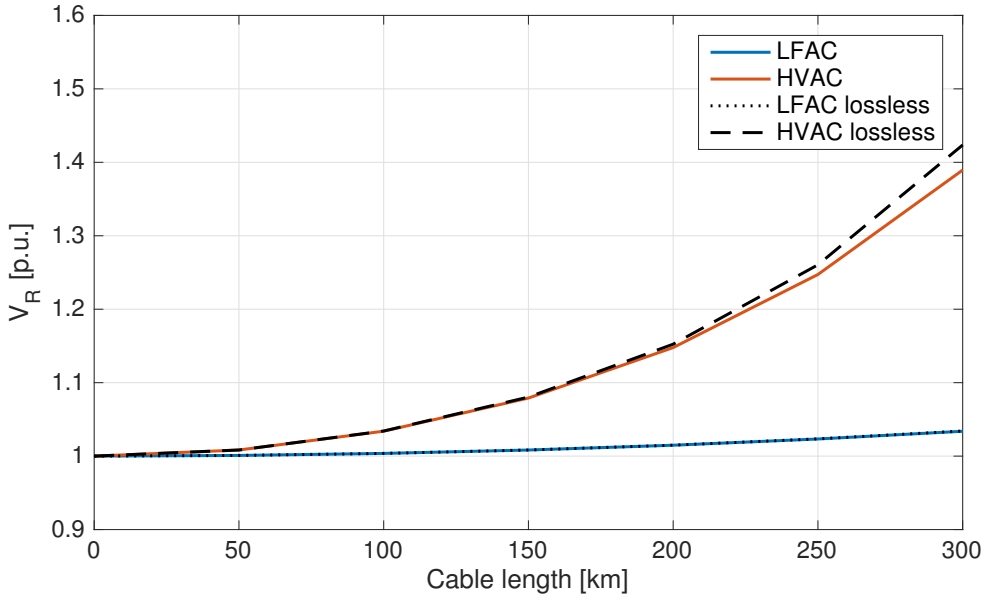

FIGURE 5.7: Receiving end voltage for simulated and theoretical lossless case

Further simulations[2] were performed where the cable resistance was increased stepwise for both systems. The results suggest that even for long cables, the resistance must be increased by a large amount before having a significant influence on the V_R damping. Also, it is observed that V_R experiences the same percentage increase for a 100 km cable, regardless of the cable resistance.

In an independent, but similar study regarding the Ferranti effect, a voltage increase of 1.7% was observed for a simulation of an unloaded 100 km HVAC cable (see [41]). This is half the value observed for the equivalent cable length in table 5.1. In the same study, a voltage rise of 8% was measured for the corresponding physical transmission system, indicating a significant error. A similar comparison can not be made in this thesis, as the simulations are not based on a real physical and accessible power system. It should however be noted that the simulated results above lie in the range of the simulated/measured results in [41].

[2]See appendix C.

Chapter 6

Energization and Switching Operation Analysis

6.1 System Description and Model

This chapter deals with the charging of an LFAC cable by switching. The purpose of the analysis is to investigate the charging currents in an LFAC cable versus an HVAC cable, and possible harmonic interaction between a power transformer and the cable after a switching operation.

For the following simulations, a three-phase system is set up in SIMULINK according to fig. 6.1. Base voltage and power[1] are set to 245 kV and 1000 MVA, respectively.

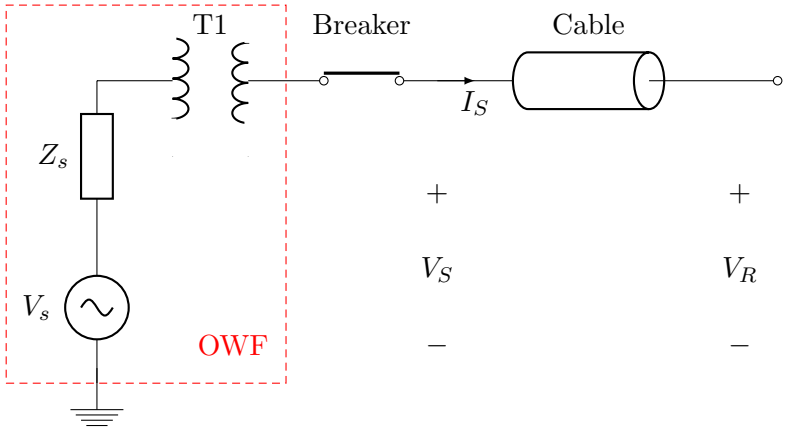

FIGURE 6.1: Unloaded OWF and cable, V_{base} = 245 kV, S_{base} = 1000 MVA

[1]For per unit-calculations, see appendix A, section A.4.

The offshore wind farm (OWF) is represented with a 66 kV phase-to-phase voltage source with internal resistance and inductance ($Z_s = R_s + j\omega L_s$), see table 6.1. The transformer T1 consists of three single-phase transformers, converting the voltage from 66 kV to 245 kV for power transmission. Cable and transformer parameters are found in table 6.2 and 6.3, respectively.

TABLE 6.1: Offshore wind farm (OWF) parameters

Parameters	**Values**
V_s	66 kV[2], 600 MW
R_s	1.0 Ω
L_s	25 mH

TABLE 6.2: Parameters for a 245 kV, 1200 mm^2 Cu cable

Cable parameters	**HVAC**	**LFAC**
I_{th}	1262 A	1534.3 A
R	25 mΩ/km	17 mΩ/km
L	0.3661 mH/km	0.3661 mH/km
C	183 nF/km	183 nF/km

TABLE 6.3: Transformer 1 parameters (T1)

Parameters	**Transformer 1**	
P_n	651.1 MW	
	Winding 1	**Winding 2**
Connection	Yg	Delta
V_n	66 kV	245 kV
R	0.002 p.u.	0.002 p.u.
L	0.08 p.u.	0.08 p.u.
R_m	500 p.u.	
L_m	500 p.u.	

The transformer parameters for resistance and inductance are default values set by SIMULINK, while the power rating is obtained from eq. (6.1):

$$P_n = \sqrt{3} V_n I_{th} \tag{6.1}$$

[2]Phase-to-phase RMS

where V_n is the cable nominal voltage (245 kV) and I_{th} is the current rating of the LFAC export cable (1534.3 A). The same power rating was used for conventional HVAC simulations.

From the frequency analysis in chapter 4, accuracy can be obtained up to several hundred of hertz with a series π-model if a sufficient number of sections are used. However, adding more sections in the series π-model increases the simulation time significantly. Taking this into consideration, the cable model best suited for the following simulations is the three-phase **distributed parameters model** (DPM).

6.2 Energization of Export Cable

In the following section, the energization of an export cable will be investigated. The analysis is divided into two cases; the first examines the sending end current consumed by the cable, while the second case studies the voltage and current behavior in greater detail during cable charging with a transformer present in the system.

6.2.1 Case 1 - Energization without Transformer

The switch in fig. 6.1 is initially open, and transformer T1 is removed in order to study the current consumption by the cable only (see fig. 6.2).

FIGURE 6.2: Energization of a cable by switch

After the switching operation, the root mean square (RMS) value of the sending end current waveforms were measured. The simulation was performed for different cable lengths, and the result is shown in fig. 6.3, where it is seen that the steady state RMS current increases linearly with the cable length.

In fig. 6.4, I_S is compared to an HVAC system for various cable lengths. It can be seen that the sending end current is far more sensitive to the change of cable length in an HVAC system compared to an LFAC system. The steady state values for both systems are summarized in table 6.4, and it can be seen that the ratio between the two systems increases as the cable length is increased. Additionally, larger oscillations are

observed in the HVAC system, which can be explained by the steepness of the current during charging. The oscillations are damped relatively fast, and the time elapsing from switching until I_S reaches its steady state is approximately equal for both systems.

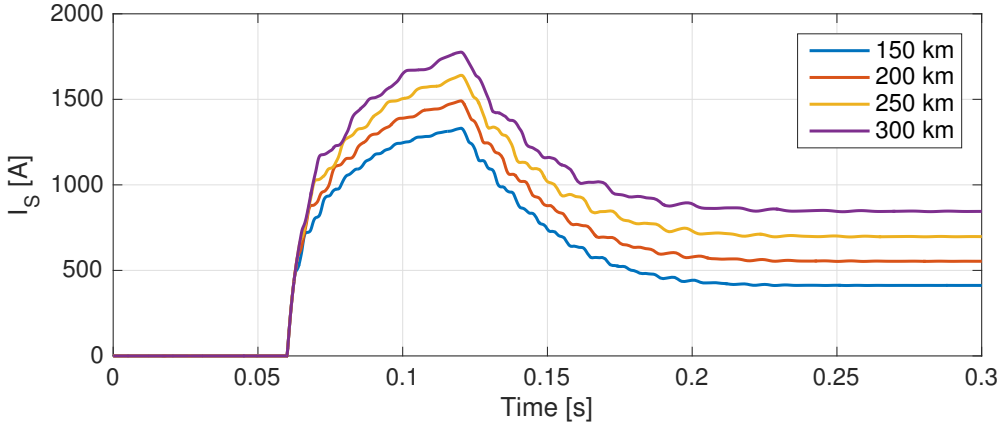

FIGURE 6.3: Sending end current (RMS) for an unloaded LFAC cable

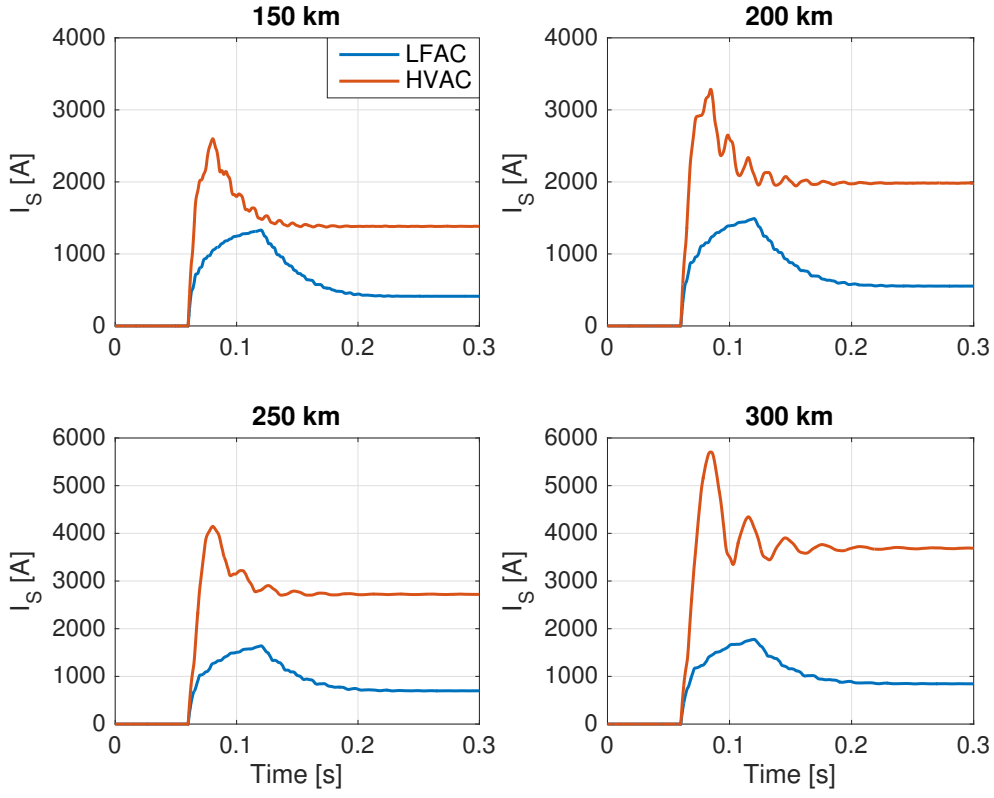

FIGURE 6.4: Sending end current (RMS) for an unloaded LFAC/HVAC cable

TABLE 6.4: Steady state sending end current for an unloaded LFAC/HVAC cable

	I_S **[A]**			
	150 km	**200 km**	**250 km**	**300 km**
LFAC	412	554	698	845
HVAC	1382	1984	2720	3692
Ratio $\left(\frac{\text{HVAC}}{\text{LFAC}}\right)$	3.4	3.6	3.9	4.4

6.2.2 Case 2 - Energization with Transformer

The same switching operation was performed as in the preceding case, but with the transformer added to the system, see fig. 6.5. The sending and receiving end voltages, V_S and V_R were measured, in addition to the sending end current I_S.

FIGURE 6.5: Energization of an unloaded cable

The results can be seen in fig. 6.6 and fig. 6.7. When the switching operation occurs, overvoltages appear at both the sending and receiving end of the cable, before reaching steady state after approximately 200 ms for both LFAC and conventional HVAC operation. The receiving end has a slightly higher value compared to the sending end. The difference is even more noticeable in the HVAC cable, which is consistent with the results from chapter 3 regarding the Ferranti effect. For the LFAC system, it is observed that V_S and V_R experience slight distortions of the waveform before stabilizing at steady state, whereas such distortions are not identified in the HVAC system. Additionally, the voltage at the cable terminals peak at a higher value relatively to its steady state value, compared to that of an HVAC system. The peak and steady state values are summarized in table 6.5. The results show slightly higher peak values relative to the steady state values in the LFAC system.

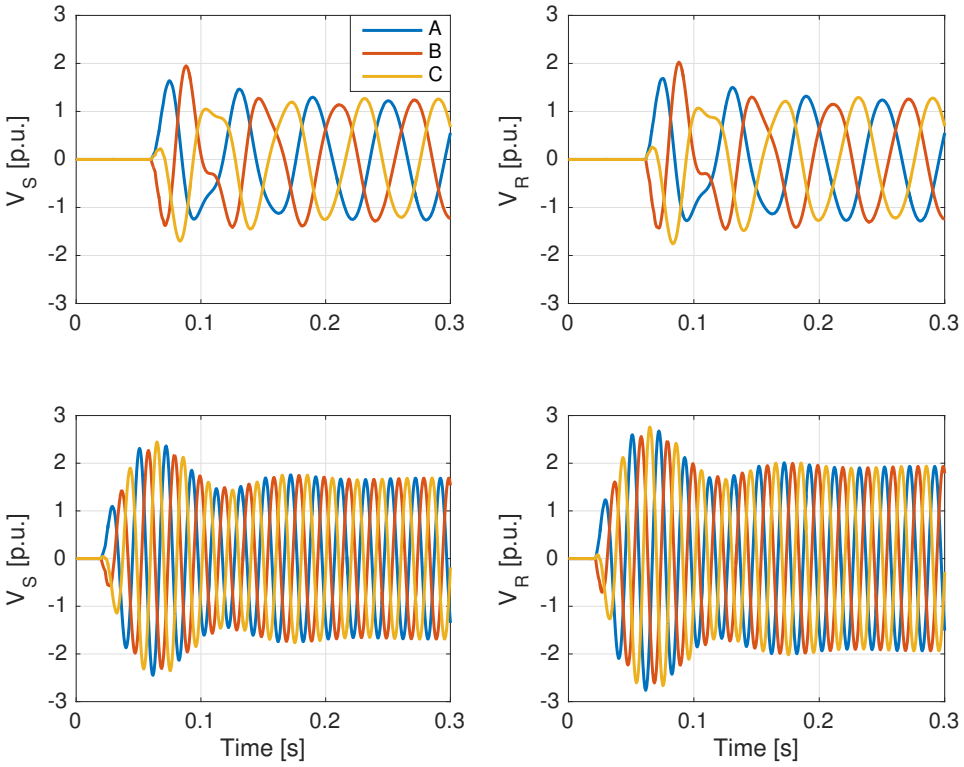

FIGURE 6.6: Sending end (left) and receiving end (right) voltage (phase to ground) after switching an unloaded cable. $l = 200$ km. Above: LFAC. Below: HVAC

TABLE 6.5: Relationship between steady state voltage and maximum voltage after switching

		$\lvert V\rvert$ **in steady state [p.u.]**	$\lvert V_{max}\rvert$ **after closing breaker [p.u.]**	**Ratio** $\left(\frac{\lvert V_{max}\rvert}{\lvert V\rvert}\right)$
LFAC	V_S	1.3	2.0	1.54
	V_R	1.3	2.0	1.54
HVAC	V_S	1.7	2.4	1.41
	V_R	1.9	2.8	1.47

Similar to the voltage, the current experiences temporary transient distortion after switching the LFAC cable. As before, no distortion is present in the HVAC system. The difference in magnitude in steady state for both frequency operations should be noted. In the LFAC system the magnitude is approximately 0.3 p.u., while for HVAC the value is 1.3 p.u. This corresponds to more than four times the LFAC charging current consumed by the export cable. Table 6.6 shows the relationship between the peak

and steady state current, revealing a significant higher current peak relative to its steady state value for the LFAC system compared to the HVAC system.

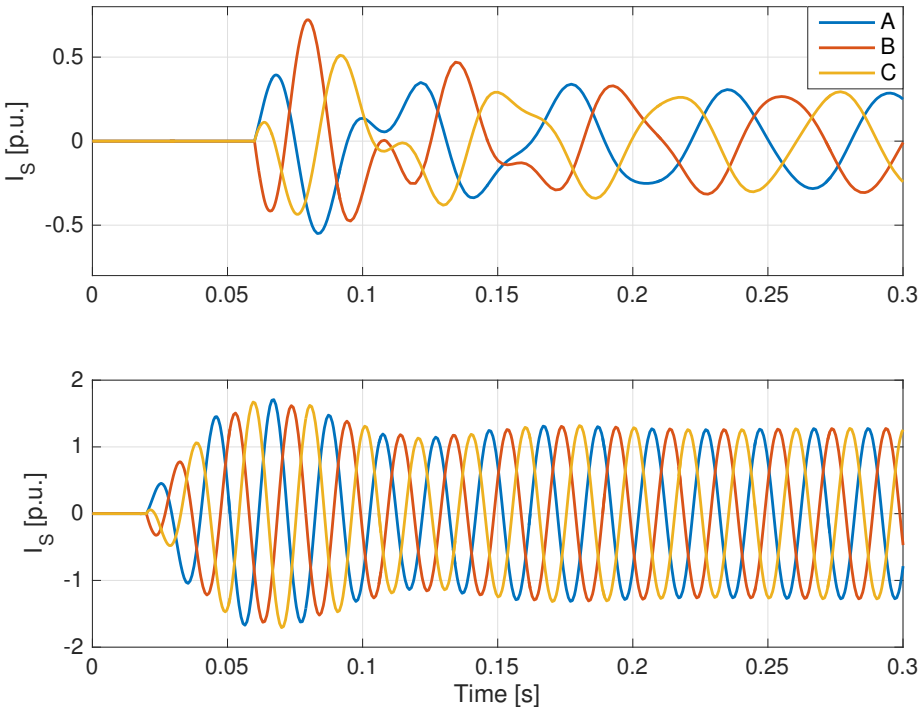

FIGURE 6.7: Sending end current after switching an unloaded cable. $l = 200$ km. Above: LFAC. Below: HVAC

TABLE 6.6: Relationship between steady state current and maximum current after switching

	$\lvert I_S \rvert$ **in steady state [p.u.]**	$\lvert I_{S,max} \rvert$ **after closing breaker [p.u.]**	**Ratio** $\left(\frac{\lvert I_{S,max} \rvert}{\lvert I_S \rvert}\right)$
LFAC	0.3	0.7	2.33
HVAC	1.3	1.7	1.31

Chapter 7

Fault Analysis

7.1 System Description and Model

This chapter deals with the dynamic behavior of the LFAC system as a result of occurring faults. Faults in a power system may cause high transient overvoltages and -currents, which can result in damage to power system components. By studying the behavior of the transmission system both during and after such faults, one receives information that can be used to properly dimension the different system components to effectively handle faults and other unexpected events. In the following sections, the fault analysis is divided in two separate studies; faults occurring at the **receiving end** of a 200 km export cable, and faults occurring at the **sending end** of the cable. The system set-up can be seen in fig. 7.1, with parameter values being the same as in the preceding simulations[1]. Fast transients are expected during the fault analysis, and from the discussion in chapter 4 and following the same reasoning as in section 6.1, the model used for the export cable is the **DPM**.

The OWF and export cable are grid connected through a second step-up transformer (T2) converting the transmission voltage from 245 kV to 400 kV. Parameters for this transformer can be found in table 7.1. In reality, the grid side would include a frequency converter to adapt the low transmission frequency to the nominal grid frequency. Because the modeling of frequency converters is not included in the scope of this thesis, the converter and grid are simply represented by an ideal voltage source acting as a swing bus. Additionally, a shunt reactor (SR) at the receiving end is made available (disconnected until section 7.3.5).

[1] See tables 6.1, 6.2 and 6.3.

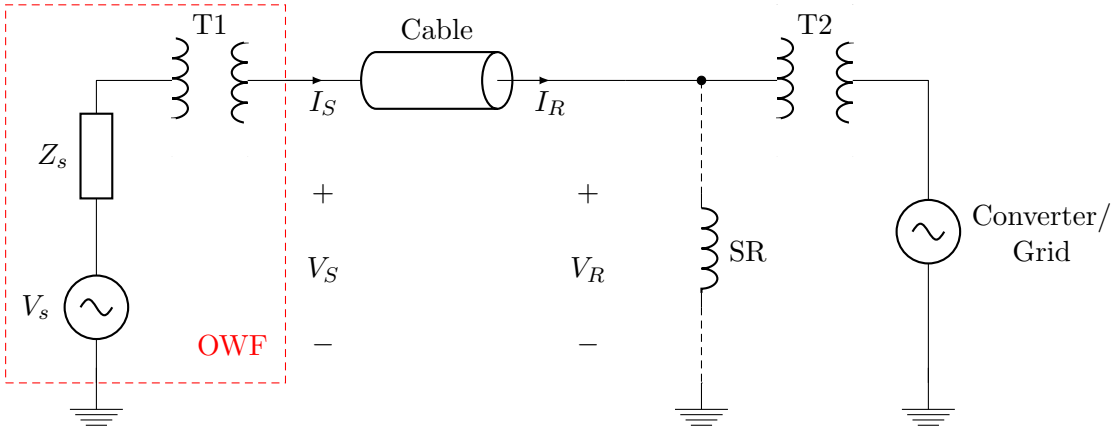

FIGURE 7.1: Fault analysis circuit set-up, $V_{base} = 245$ kV, $S_{base} = 1000$ MVA

TABLE 7.1: Transformer 2 parameters (T2)

Parameters	**Transformer 2**	
P_n	651.1 MW	
	Winding 1	**Winding 2**
Connection	Delta	Yg
V_n	245 kV	400 kV
R	0.002 p.u.	0.002 p.u.
L	0.08 p.u.	0.08 p.u.
R_m	500 p.u.	
L_m	500 p.u.	

7.2 Faults at the Receiving End

Faults occurring somewhere in the grid causing either voltage sags or swells (i.e. sudden, but temporary voltage collapse/rise) will be investigated. The former may be caused by short circuit faults, while the latter can be a result from sudden loss of load(s). For the analysis, the voltage and current at the sending end of the export cable were examined.

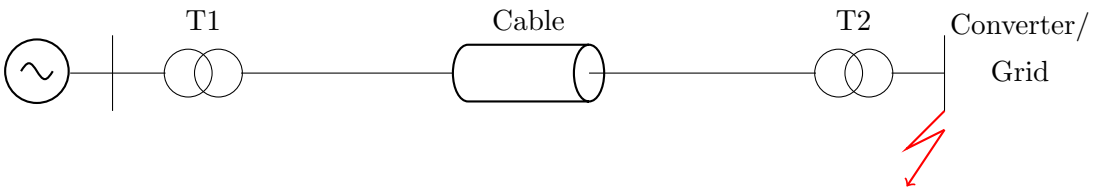

FIGURE 7.2: Fault event occurring somewhere in the grid, resulting in voltage sags/swells

For the simulations, a programmable voltage source from the SIMULINK library was used, where the magnitude voltage sag/swell was specified for each case. The duration of the fault was set equal for both cases:

- Fault occurring at $t = \frac{1}{f_n}$ (= 60 ms)
- Fault cleared at $t = \frac{4}{f_n}$ (= 240 ms)

7.2.1 Voltage Sag

The voltage on the converter/grid side was reduced from 1.0 p.u. to 0.5 p.u. Voltage and current at the sending end of the cable were measured, and the results are shown in fig. 7.3. Temporary voltage distortion is observed for approximately 100 ms after the voltage sag, approaching a steady state value of 0.6 p.u. When the fault is cleared (grid side voltage restored), a short overvoltage is observed, reaching -1.2 p.u.

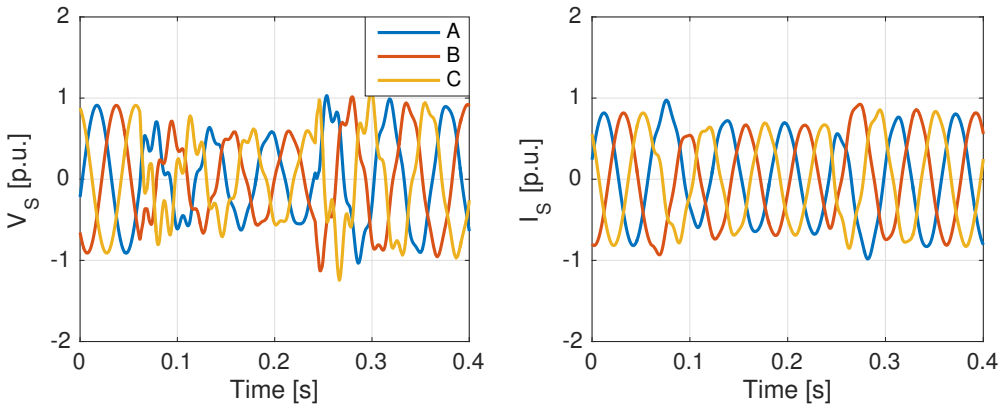

FIGURE 7.3: Sending end voltage (phase to ground) and current before, during and after occurrence of a voltage sag on the grid side

The current I_S experiences no particular transient distortion after the fault or restoration. However, the magnitude increases to 1.0 p.u. (compared to 0.8 p.u. in steady state) for a duration of one time period after fault occurance/clearance.

7.2.2 Voltage Swell

The grid voltage was increased from 1.0 p.u. to 1.5 p.u., and the results are shown in fig. 7.4. Similar to the case of voltage sag, V_S experiences slight transient distortion for approximately two time periods posterior to both fault and restoration. During the

fault, the voltage approaches a steady state value of 1.3 p.u. I_S is observed to peak at 1.2 p.u. after the occurrence of the voltage swell, before stabilizing at 1.1 p.u. during the fault.

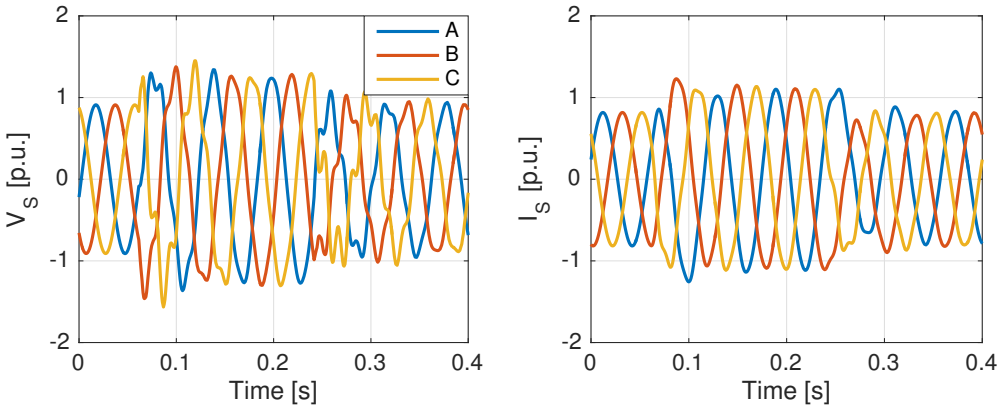

FIGURE 7.4: Sending end voltage (phase to ground) and current before, during and after occurrence of a voltage swell on the grid side

In summary; for both cases regarding a sudden drop or rise in the grid voltage, there is no rapid transient behavior the voltage and current at the opposite end of the transmission cable, although transient distortion is observed for the voltage waveform.

7.3 Faults at the Sending End

In this section, short circuit (SC) faults at the sending end occurring between the first step-up transformer T1 and the LFAC export cable will be examined, as illustrated in fig. 7.5. For comparison purposes, the analysis will also be performed for an HVAC system[2]. The faults to be simulated are:

1. Three phase (ABC) to ground
2. Single phase (A) to ground
3. Two phase (A and B) to ground
4. Phase to phase (A to B)

[2]See appendix D, section D.1.

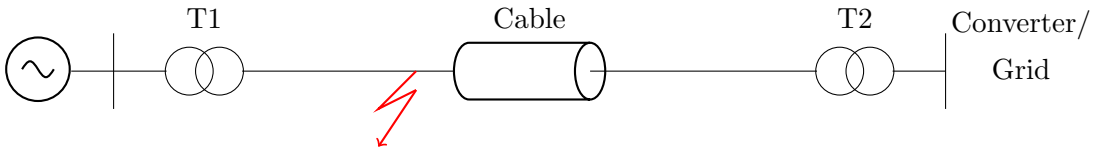

FIGURE 7.5: Short circuit (SC) at receiving end of the LFAC export cable

The duration of the faults are simulated with respect to the the signals time periods, i.e.:

- Fault occurring at $t = \frac{1}{f_n}$ (= 60 ms)
- Fault cleared at $t = \frac{2}{f_n}$ (= 120 ms)

Because the fault is chosen as a function of frequency, the HVAC system faults will be shorter in time, however they last for an equal number of periods. The fault resistance is set to 1.0 mΩ. For each case, the behavior of the voltage and current at both cable ends will be examined. Additionally, the voltage DC offset following some of the SC events will be examined. The simulations performed for the HVAC system can be found in appendix D.

7.3.1 Three Phase to Ground Fault

At the time of the fault, the sending voltage V_S drops to zero, while the receiving voltage V_R experiences transients in the range of 160-180 Hz. At fault clearance, overvoltages occur at both ends of the cable, with phase B reaching a value greater than -2 p.u. The transients are damped relatively fast, although it is observed that the voltage signals are skewed vertically, indicating a DC offset. Large overcurrents are observed at both ends of the cable, with phase A and B reaching -4 p.u. and 4 p.u., respectively. The largest currents are observed at the sending end of the cable, with faster transients than the receiving end. The current rapidly reaches steady state after fault clearance, although a greater share of distortion is observed at the receiving end.

A closeup of the receiving voltage immediately after the fault is shown in fig. 7.7. It can be observed that it takes approximately 1.64 ms before V_R reacts to the fault at the sending end. This time delay is identified as the traveling time τ of the voltage wave, obtained in eq. (3.54) in section 3.2.4.1. Further, V_R experiences sudden drop/rises each 3.28 ms, which is equivalent to 2τ, i.e. the time for the voltage waves to travel to the sending end of the cable and back to the receiving end.

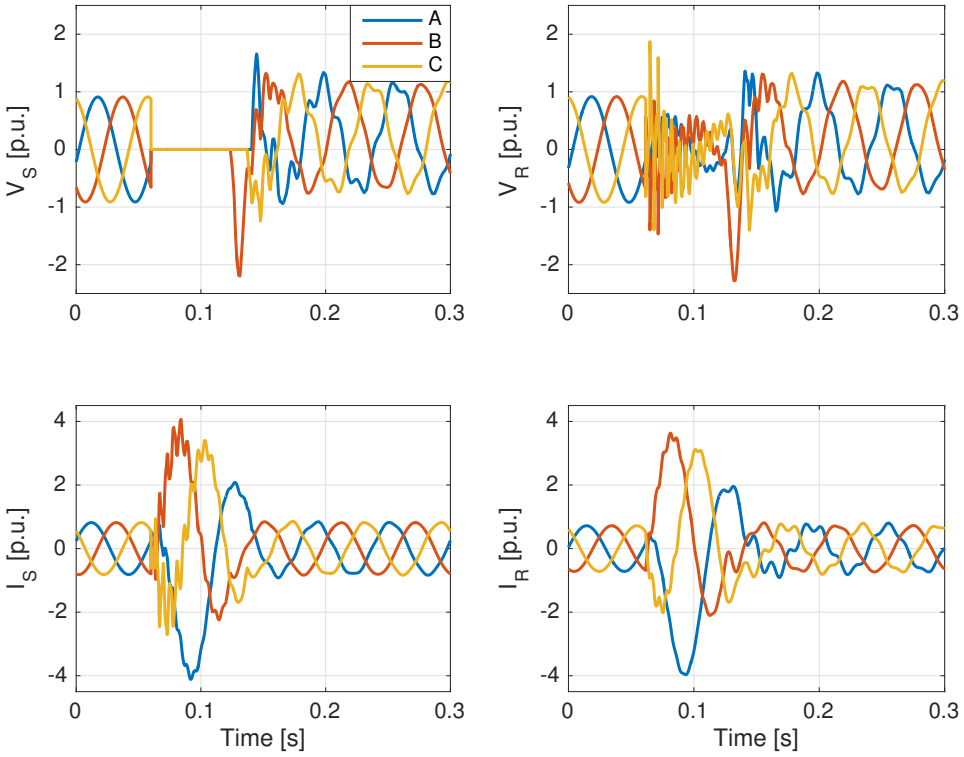

FIGURE 7.6: Sending and receiving end voltages (phase to ground) and currents before, during and after a three phase to ground fault

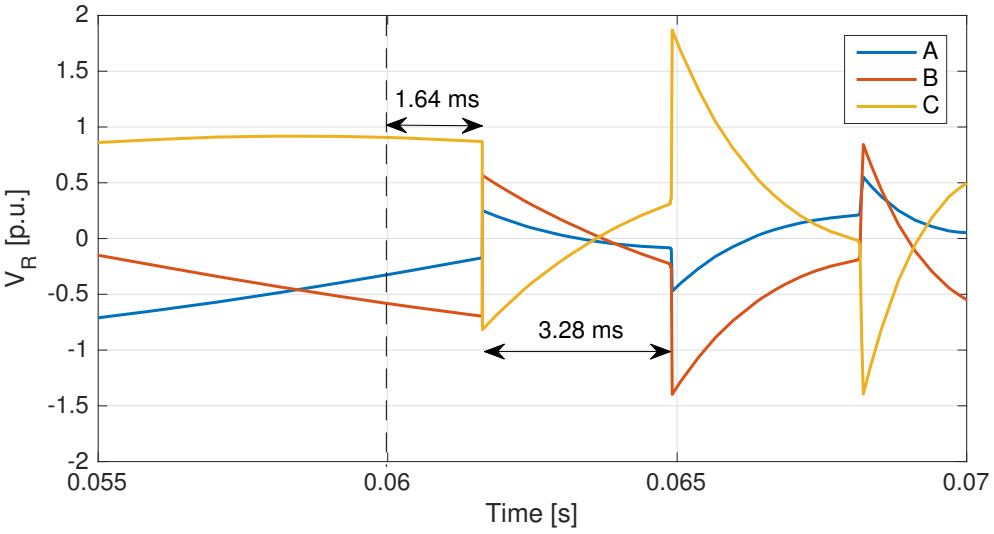

FIGURE 7.7: Closeup of the receiving end voltage after fault

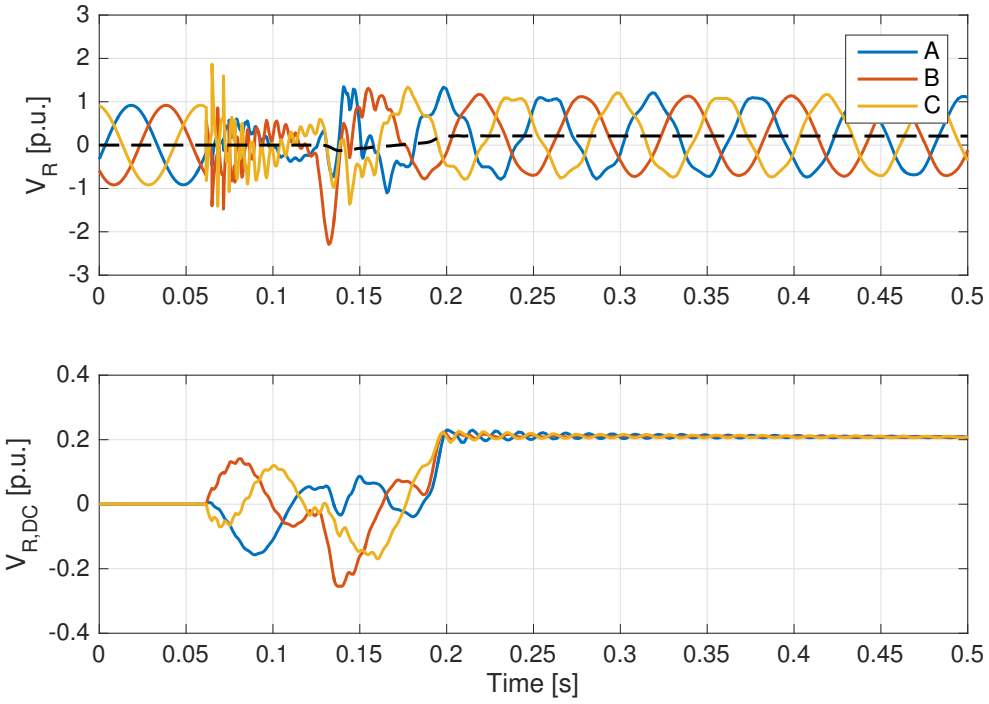

FIGURE 7.8: Above: Receiving end voltage with average DC offset (dashed line). Below: DC offset for all phases.

Fig. 7.8 shows V_R along with the average DC offset ($V_{R,DC_{avg}}$) in addition to the offset $V_{R,DC}$ for each phase. During the fault, the average offset is zero, as the fault is balanced and the sum of all phases are zero. After the fault is cleared and the AC component has regained its steady state waveform, V_R has a DC offset $V_{R,DC_{avg}}$ with a magnitude of 0.2 p.u. The magnitude of the DC component will decrease slowly, reaching zero at after approximately 90 s (see fig. D.5 in appendix D).

7.3.2 Single Phase to Ground Fault

The fault occurs between phase A and ground. From fig. 7.9 it can be seen that for V_S, the amplitudes of phase B and C increase significantly immediately after the fault, both reaching -1.8 p.u. For V_R, the amplitude during the fault is even higher, reaching almost 2 p.u. No significant transient behavior is observed for the voltage and current waves, and steady state is regained rapidly after fault clearance. However, the sinusoid of the voltage for both cable ends is shifted vertically by -1 p.u., indicating a high DC offset. This is shown in fig. 7.10.

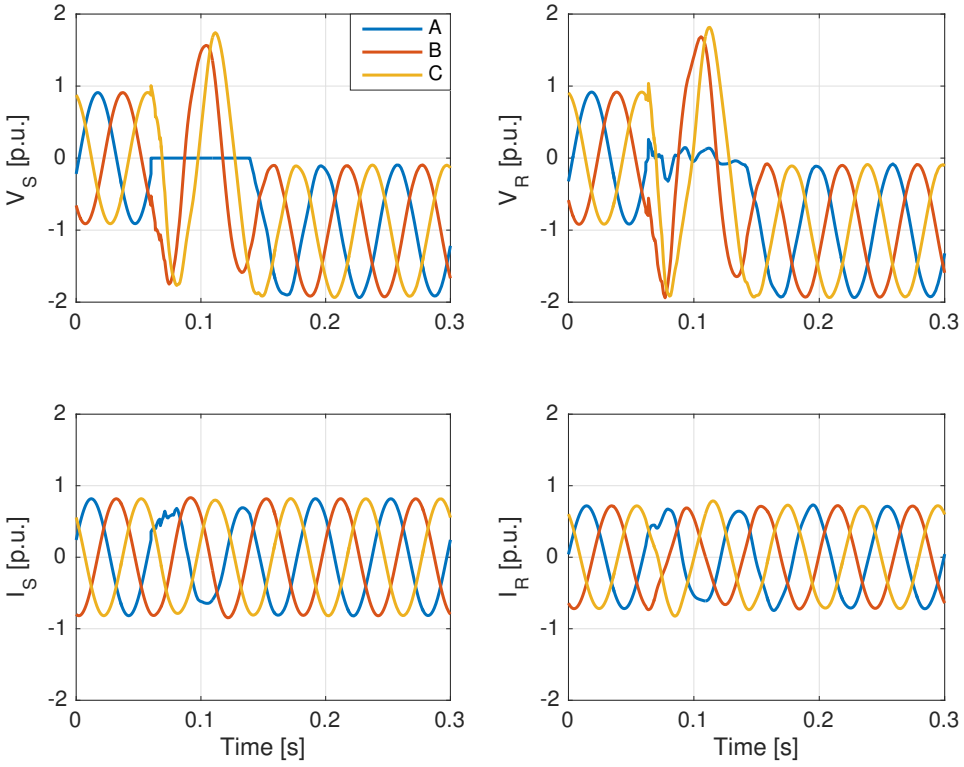

FIGURE 7.9: Sending and receiving end voltages (phase to ground) and currents before, during and after a single phase to ground fault

The fault is observed to have very little influence on the current in the LFAC system. Comparing to the HVAC simulations[3], it can be seen that the behavior of the current is very different. Overcurrents and waveform distortions are observed for the latter, especially at the receiving end. Additionally, the magnitude of the observed voltage DC offset is larger in the HVAC system.

[3]See appendix D, fig. D.2.

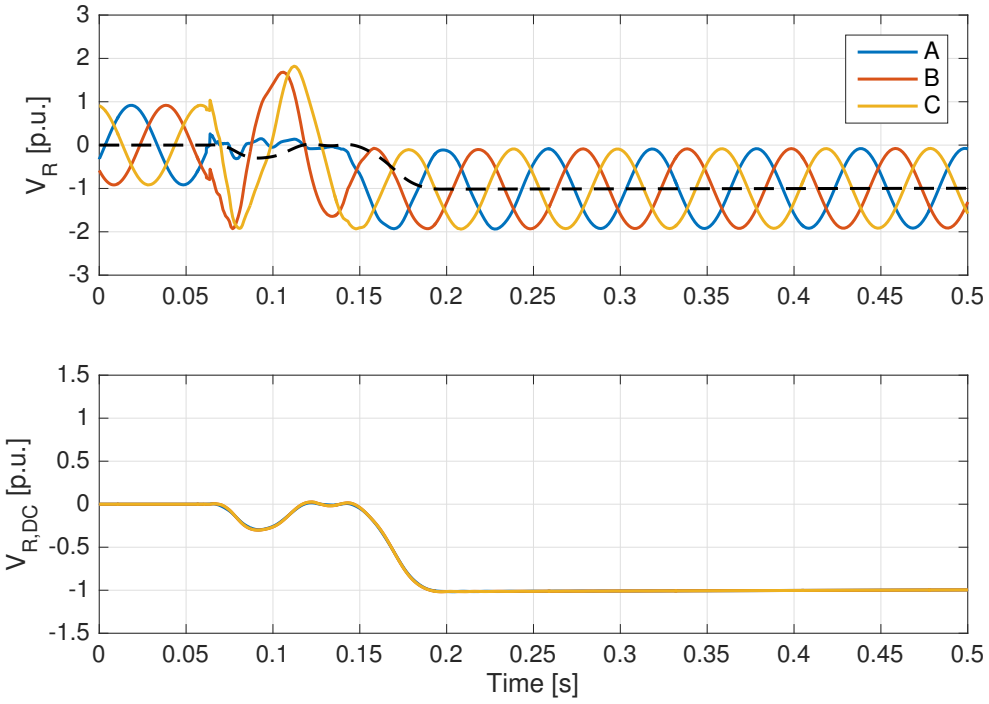

FIGURE 7.10: Above: Receiving end voltage with average DC offset (dashed line). Below: DC offset for all phases

7.3.3 Double Phase to Ground Fault

The fault occurs between phases A and B, and ground, and the sending and receiving end voltages and currents are shown in 7.11. As phase A and B go to zero at fault occurrence, phase C peaks at 1.5 p.u. for V_S. At the receiving end, transients are observed for phases A and B, with a 180° phase shift. After clearance, V_S and V_R peak at 1.6 p.u. and 1.5 p.u., respectively. The voltages have a long lasting DC offsets after fault clearance which last up to 100 s (see fig. D.5). Comparing the LFAC system to the HVAC system (fig. D.6), it is observed that the DC offset is far more prominent for V_S and V_R in the latter.

At the time of the fault, the current in phase A and B increase greatly in amplitude, where the latter reaches a peak value of 4 p.u. Although peaking at the same time, phase A and B are shifted 180° relative to each other. After fault clearance, I_R experiences some transient behavior due to transient distortion, which results in an increased amount of time needed to stabilize at steady state. Approximate measurements show that the time between clearance and regaining steady state is 100 ms for I_S, and 200 ms for I_R.

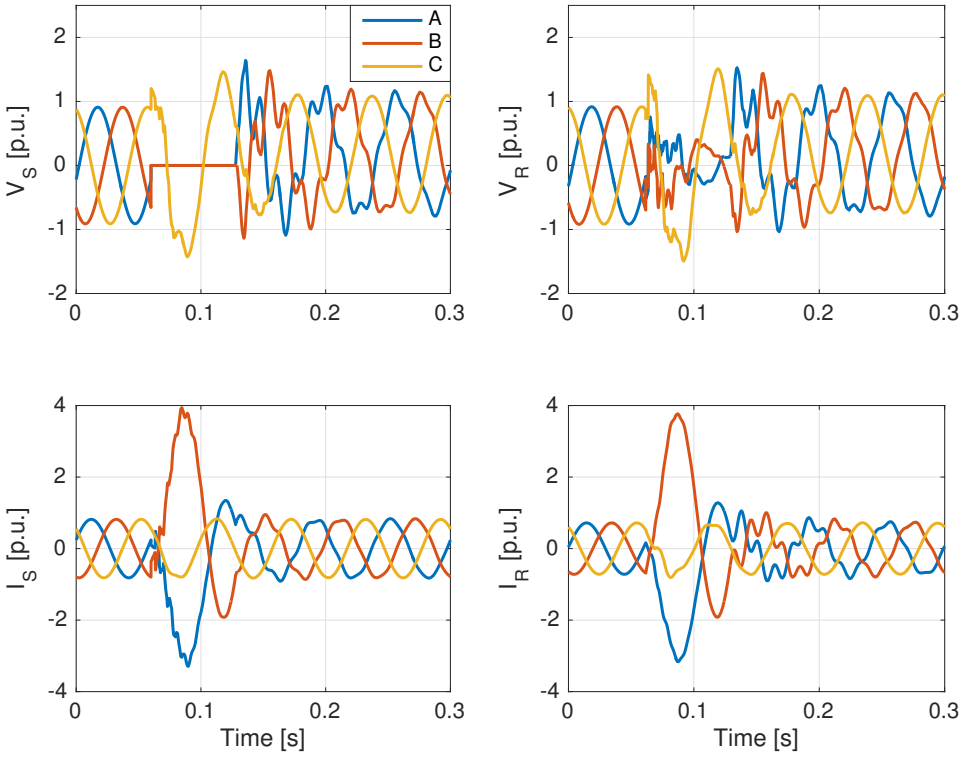

FIGURE 7.11: Sending and receiving end voltages (phase to ground) and currents before, during and after a double phase to ground fault

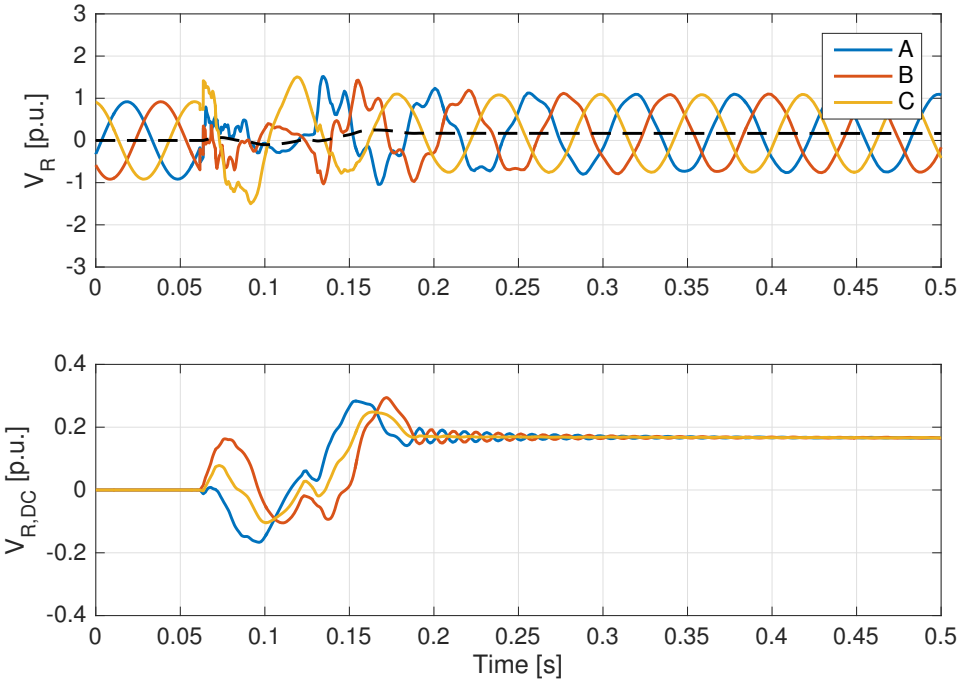

FIGURE 7.12: Above: Receiving end voltage with average DC offset (dashed line). Below: DC offset for all phases

7.3.4 Phase to Phase Fault

The fault occurs between phase A and B, and the result is shown in fig. 7.13. At the time of the fault, phase A and B become equal at the cable sending end. At the receiving end they are shifted 80° apart with fast transient behavior. After fault clearance, V_S and V_R peak at 1.5 p.u. and 1.4 p.u. respectively, and temporary transient distortion is observed. Additionally, a phase to phase fault does not result in a DC offset in V_S or V_R, which was observed for the preceding fault events studied in sections 7.3.1-7.3.3.

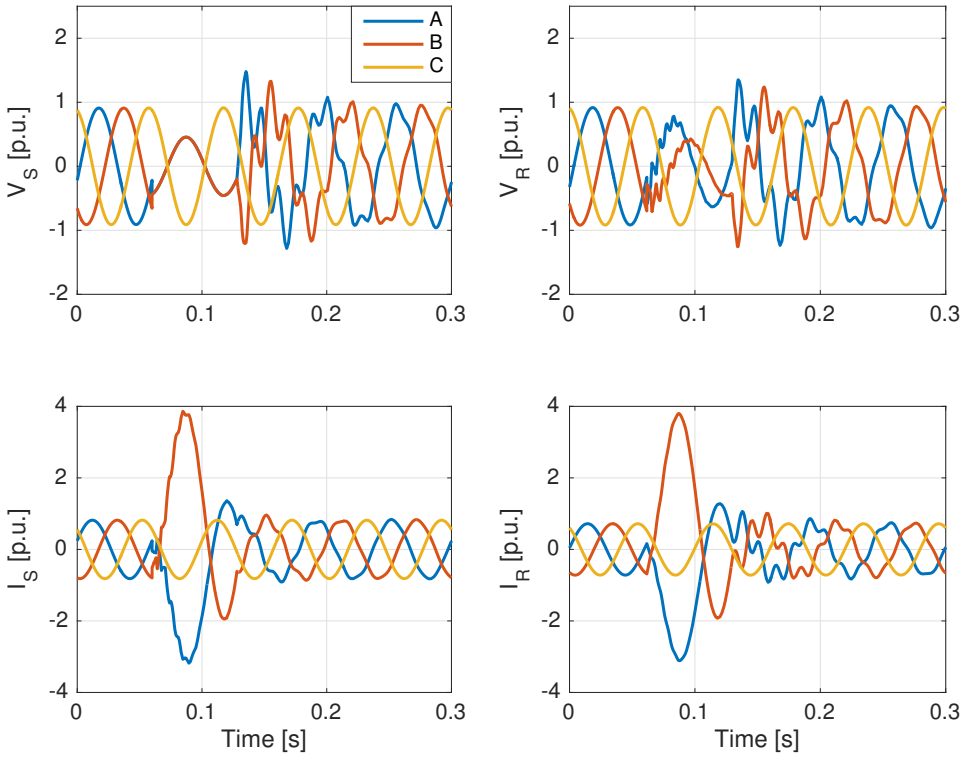

FIGURE 7.13: Sending and receiving end voltages (phase to ground) and currents before, during and after a single phase to phase fault

Similar to the double phase to ground fault, large currents occur at both cable ends at the time of the fault, with phase B peaking close to 4 p.u. Phase A reaches its peak at the same time (-3 p.u.), being shifted 180° compared to phase B. After clearance, the current amplitudes decline rapidly for A and B, reaching steady state after approximately 100 ms at the sending end. For I_R, the time from clearance to steady state is approximately 200 ms, i.e. twice the value compared to I_S. This is due to a larger share of transient distortion which requires damping.

$V_{R,DC_{avg}}$ is zero both during and after the fault, as seen in fig. 7.14. The offsets of phase A and B are observed to be non-zero during and shortly after the fault, with a 180° phase shift with respect to each other (opposite polarity).

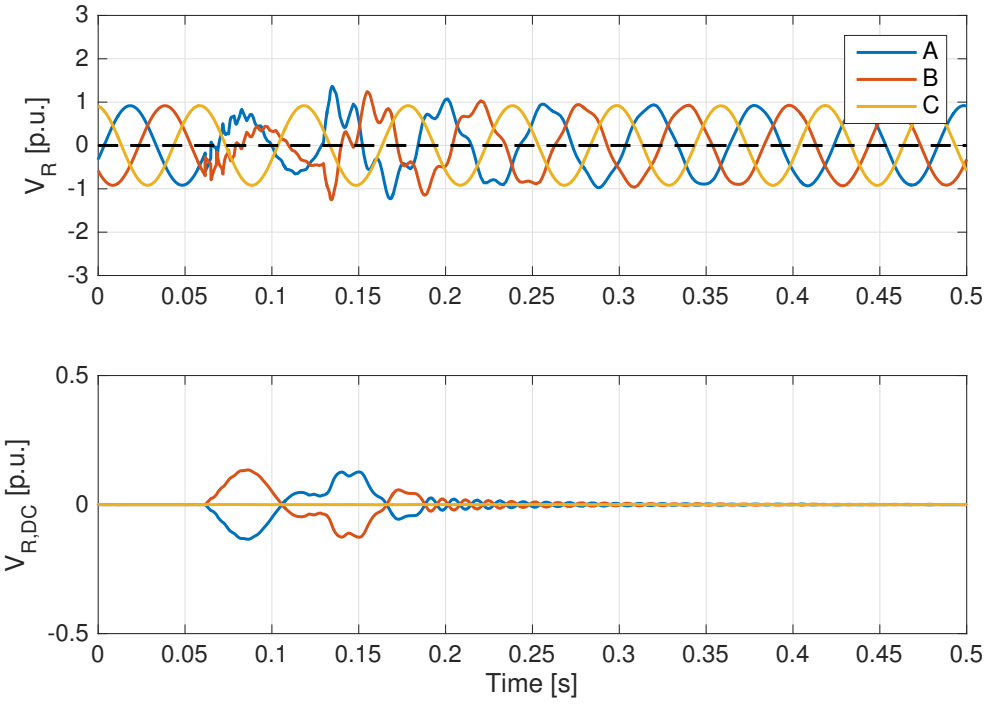

FIGURE 7.14: Above: Receiving end voltage with average DC offset (dashed line). Below: DC offset for all phases

The magnitude of the average DC offset values after fault clearance is summarized in table 7.2 for each fault event, where the values for the HVAC system are obtained from fig. D.6 in appendix D. Among the various fault events, the single phase to ground fault results in the highest DC offset after fault clearance, while the phase to phase fault results in the lowest (being zero). For conventional HVAC, the magnitude of the DC offset is higher than LFAC for all cases except phase to phase fault (being zero also). At most, the DC offset of the HVAC system exceeds the DC offset of the LFAC system by a factor of 10.9, occurring for the double phase to ground fault. The high values, and especially the duration of the DC offsets occurring after the different fault events (for both LFAC and HVAC) should be examined more closely. The cause of the observed results are addressed in chapter 8.

TABLE 7.2: DC offset for different fault events in LFAC and HVAC systems

	$\lvert V_{R,DC_{avg}} \rvert$ **[p.u.]**			
	Three phase to ground	*Single phase to ground*	*Double phase to ground*	*Phase to phase*
LFAC	0.21	1.01	0.17	0
HVAC	0.57	2.44	1.86	0
Ratio $\left(\frac{\text{HVAC}}{\text{LFAC}}\right)$	2.7	2.4	10.9	-

7.3.5 Adding Shunt Reactor

The 350 MVA (purely inductive) shunt reactor in fig. 7.1 is connected to the system. The fault previously resulting in the largest DC offset, i.e. the single phase to ground fault, is simulated.

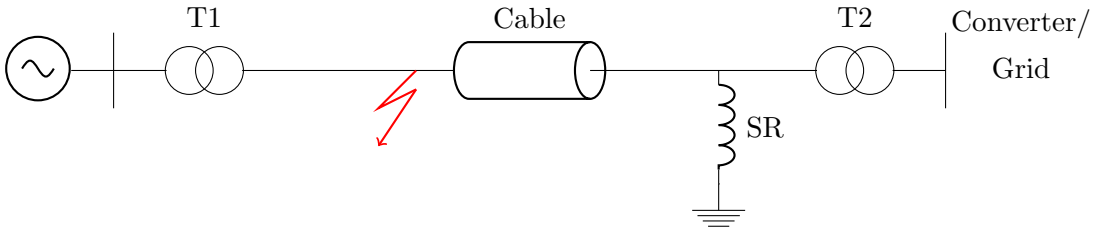

FIGURE 7.15: Transmission system with shunt reactor (SR) at the receiving end

The DC offset of V_R for each phase can be seen in fig. 7.16. It is observed that the maximum magnitude of the DC offset has been reduced from 1.01 p.u. to approximately 0.13 p.u., before being damped rapidly. It can be seen that all the phases of $V_{R,DC}$ oscillate in phase after the fault clearing with a frequency of approximately 30 Hz, i.e. nearly twice the nominal frequency (superharmonic). The oscillations are damped to zero after approximately 500 ms after fault clearing. Such oscillations were not observed in the preceding simulations without the connection of a shunt reactor. The average DC offset in the two cases are compared in fig. 7.17.

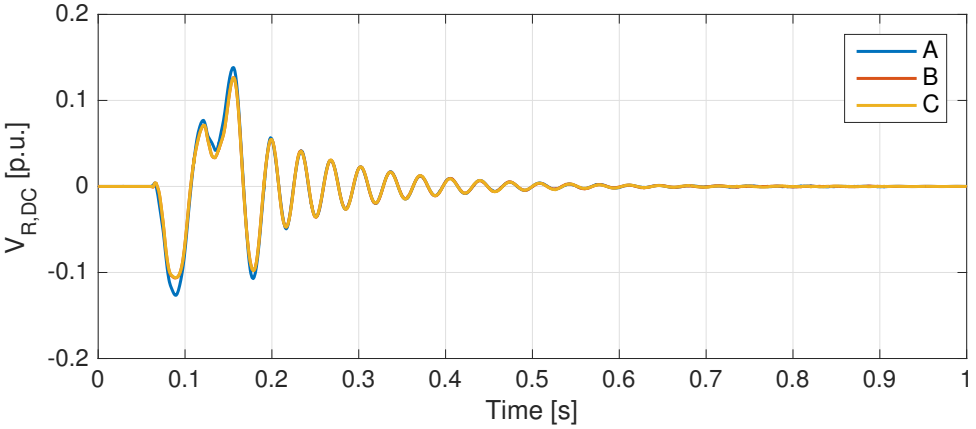

FIGURE 7.16: V_R DC offset for single phase to ground fault with connected shunt reactor

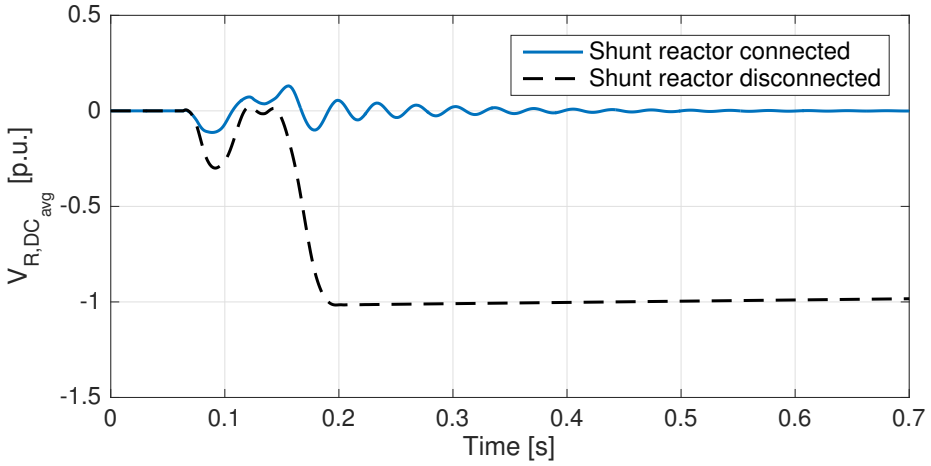

FIGURE 7.17: Average DC offset for the single phase to ground fault with/without shunt reactor

In fig. 7.18, the average value of the DC offset is compared to an HVAC system. The start-time of the fault for the HVAC system has been set equal to the LFAC system (60 ms) in order to make comparisons regarding oscillation damping simpler. It is seen that although the amplitude of the DC offset is similar, the damping is more prominent in the HVAC system. The damping can be improved by adding a resistive component to the shunt reactor, see fig. D.7 in appendix D. Measurements show that the oscillation frequency of $V_{R,DC_{avg}}$ in the HVAC system is approximately 44 Hz, which unlike the LFAC case is below the nominal frequency of the system (subharmonic).

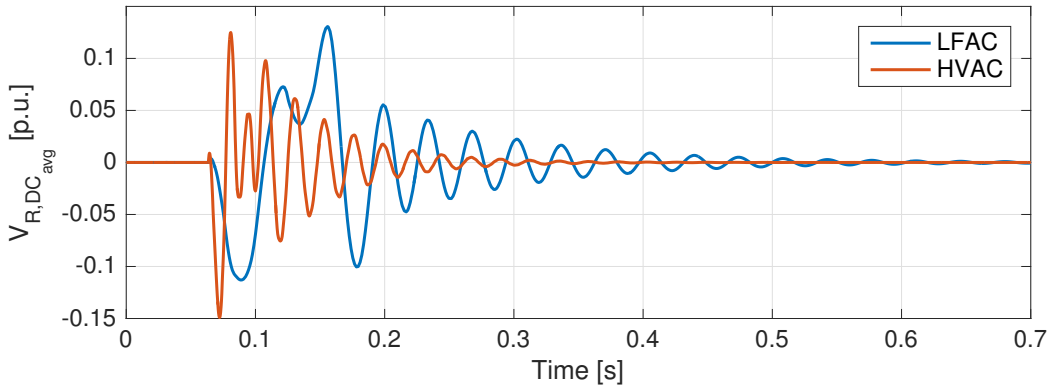

FIGURE 7.18: Average DC offset for the LFAC and HVAC system with connected shunt reactor

Chapter 8

Conclusion and Further Work

Discussion and Conclusion

The properties of an LFAC export cable have been examined under both steady state and certain dynamic conditions. The model representing the LFAC system has been gradually developed throughout the thesis, along with relevant analyses. In the frequency analysis, the frequency response of the export cable along with a simplified model of the offshore wind farm (OWF) was investigated. A comparison with a conventional HVAC system revealed a lower damping at the resonant frequencies for the LFAC system, which can be explained by the lower resistance and inductive reactance in the latter. For an LFAC export cable with a length of 200 km, the first resonant frequency was observed close to the 9th harmonic of the fundamental. Increasing the OWF inductance, lower resonant frequencies close to the 5th and 7th harmonic were observed. Extension of the cable length and OFW inductance contributed to further lowering the resonant frequencies, and the low-order harmonics could interact with other power system components, resulting in disturbances and distortion of voltage and current signals. It is important to keep in mind that the analysis was based on a simplified power system without taking components such as transformers and converters into consideration. A more detailed study on an expanded LFAC transmission system could provide more information regarding harmonic interaction, and could be a topic for future studies.

The Ferranti effect was examined for an unloaded export cable, and the results showed that the Ferranti effect was less prominent for the LFAC system compared to the HVAC system. For a 200 km LFAC cable, the voltage increased by 1.5%, whereas the corresponding increase in the HVAC system was observed to be 14.8%. The difference seems very high, as one could expect a larger damping in the HVAC system. The results were

close, but not identical to the theoretical lossless values. Simulations were repeated using different cable models, however the same results were obtained. A comparison revealed that the simulated result for the HVAC system was in the range obtained for simulated values and actual measurements in a separate study regarding the Ferranti effect. Hence the result seems valid, although more detailed studies are recommended. Because the LFAC cable is less affected by the Ferranti effect, disconnections and load loss are less likely to result in severe overvoltages compared to conventional HVAC systems, and system components are less prone to possible damage.

The energizing current does not seem to be very sensitive to increased cable length for an LFAC cable. In addition to having a higher current demand for energizing an HVAC cable, it is more sensitive to the increase of cable length. Less transient behavior was observed for energizing current in the LFAC system. However, a larger share of distorted waveforms for both currents and voltages were observed when energizing the LFAC cable, and higher peak values relative to its steady state values were identified during energization. Further studies are recommended to determine the degree of possible harmonic distortion in an LFAC system compared to a conventional HVAC system.

The fault analysis revealed short and temporary distortions in the case of grid voltage sags and swells. Analyzing short circuit faults at the cable sending end, the highest voltages and currents were observed in the case of a three phase to ground fault. This fault event also resulted in the fastest transients. Transient distortion was more noticeable for the double phase to ground and phase to phase faults, while the single phase to ground fault resulted in the highest DC offset posterior to the fault clearance. Long lasting DC offsets after fault clearing is generally observed to be higher for the HVAC system compared to the LFAC system. It was observed that the single phase to ground fault resulted in the highest DC offset magnitude compared to other faults.
The high DC offsets can be explained by the model set-up, as there are no ground connections where the fault occurs. Hence, the system section consisting of the cable (and transformer delta-windings) loses its ground reference and becomes a floating neutral after the faults are cleared. To prevent high DC offsets, it is therefore necessary to provide sufficient grounding in the system. By installing a grounded shunt reactor at the receiving end, the problem of long lasting DC offsets was solved; however one should take into consideration the resulting oscillations of the DC offset. The frequency of the oscillating DC offsets were measured to be $\sim$30 Hz for the LFAC system (superharmonic) and $\sim$44 Hz for the HVAC system (subharmonic), and it should be investigated whether these low-frequency oscillations could have a negative impact on the system.

The overall results indicate no significant drawbacks for the LFAC system under steady

and dynamic conditions compared to a HVAC system. Steady state performance regarding the Ferranti effect and charging currents showed a distinct improvement for the LFAC system, while the behavior under dynamic fault conditions were similar for both systems. Further studies are recommended before making final conclusions whether LFAC transmission systems should be used for power transfer from offshore wind farms in the future.

Further Work

Although certain properties of the export cable in an LFAC system have been examined in this thesis, the models used in the analyses have been very simplified. Additionally, many values used in the simulations for the system components (apart from the cable) might differ significantly from real values for an OWF. To determine whether LFAC transmission systems could be a feasible way to transmit power from offshore wind farms in the future, further topics should be investigated. Examples include:

- A more detailed investigation of the Ferranti effect, expanding the model to include additional components apart from the export cable.
- Implementation of a frequency converter, for both the wind turbines and shore-based converter station.
- Exploration of more detailed cable models through alternative simulation tools such as EMTP/PSCAD, utilizing frequency dependent cable models for more accurate analysis of the cable dynamics.
- Simulation of fault events over longer time periods, and investigate circuit breaker operations to handle such faults.
- Investigation of LFAC transformers and power converters with respect to harmonic interference.

Bibliography

[1] European Commission. Eu energy in figures - statistical pocketbook 2014. Technical report, 2014. URL https://ec.europa.eu/energy/sites/ener/files/documents/2014_pocketbook.pdf.

[2] H.H. Larsen and L.S. Petersen. Wind energy - drivers and barriers for higher shares of wind in the global power generation mix. Technical report, Technical University of Denmark, November 2014.

[3] C. Morris and M. Pehnt. Energy transition - the german energiewende, 2012. URL http://energytransition.de/wp-content/themes/boell/pdf/en/German-Energy-Transition_en.pdf.

[4] Renewable Energy Directive. National renewable energy action plan for the united kingdom, 2009. URL https://www.gov.uk/government/uploads/system/uploads/attachment_data/file/47871/25-nat-ren-energy-action-plan.pdf.

[5] Department of Energy & Climate Change. Uk renewable energy roadmap, 2011. URL https://www.gov.uk/government/uploads/system/uploads/attachment_data/file/48128/2167-uk-renewable-energy-roadmap.pdf.

[6] European Wind Energy Association. The european offshore wind industry - key trends and statistics 1st half 2015. Technical report, European Wind Energy Association, July 2015. URL http://www.ewea.org/fileadmin/files/library/publications/statistics/EWEA-European-Offshore-Statistics-H1-2015.pdf.

[7] M. Mace. World's largest floating wind farm gets green light in scotland, 2. November 2015. URL http://www.theguardian.com/environment/2015/nov/02/worlds-largest-floating-windfarm-gets-green-light-in-scotland.

[8] European Wind Energy Association. The european offshore wind industry - key trends and statistics 2010. Technical report, European Wind Energy Association, January 2011. URL http://www.ewea.org/fileadmin/files/library/publications/statistics/20110121_Offshore_stats_Full_Doc_final.pdf.

[9] European Wind Energy Association. The european offshore wind industry - key trends and statistics 2011. Technical report, European Wind Energy Association, January 2012. URL http://www.ewea.org/fileadmin/files/library/publications/statistics/EWEA_stats_offshore_2011_02.pdf.

[10] European Wind Energy Association. The european offshore wind industry - key trends and statistics 2012. Technical report, European Wind Energy Association, January 2013. URL http://www.ewea.org/fileadmin/files/library/publications/statistics/European_offshore_statistics_2012.pdf.

[11] European Wind Energy Association. The european offshore wind industry - key trends and statistics 2013. Technical report, European Wind Energy Association, January 2014. URL http://www.ewea.org/fileadmin/files/library/publications/statistics/European_offshore_statistics_2013.pdf.

[12] European Wind Energy Association. The european offshore wind industry - key trends and statistics 2014. Technical report, European Wind Energy Association, January 2015. URL http://www.ewea.org/fileadmin/files/library/publications/statistics/EWEA-European-Offshore-Statistics-2014.pdf.

[13] European Marine Observation and Data Network. Portal for bathymetry. URL http://portal.emodnet-bathymetry.eu/mean-depth-rainbow-colour-ramp-no-land-data/legend. [Online; accessed 18-January-2016].

[14] European Network of Transmission System Operators for Electricity. Offshore transmission technology, November 2011. URL https://www.entsoe.eu/fileadmin/user_upload/_library/publications/entsoe/SDC/European_offshore_grid_-_Offshore_Technology_-_FINALversion.pdf.

[15] H.-J. Knaak. Modular multilevel converters and hvdc/facts: A success story. pages 1–6, Aug 2011.

[16] X. Wang and X. Wang. Feasibility study of fractional frequency transmission system. May 1996.

[17] H. Waje-Andreassen. Low frequency ac transmission as an alternative of connecting large remote offshore wind farms. NTNU specialization project, 2014.

[18] T. Funaki and K. Matsuura. Feasibility of the low frequency ac transmission. In *Power Engineering Society Winter Meeting, 2000. IEEE*, volume 4, pages 2693–2698. IEEE, 2000.

[19] P. Bresesti, W.L. Kling, R.L. Hendriks, and R. Vailati. Hvdc connection of offshore wind farms to the transmission system. *Energy Conversion, IEEE Transactions on*, 22(1):37–43, 2007.

[20] ABB. Borwin1. URL `http://new.abb.com/systems/hvdc/references/borwin1`. [Online; accessed 20-January-2016].

[21] W.-J. Fischer, R. Braun, and I. Erlich. Low frequency high voltage offshore grid for transmission of renewable power. In *Innovative Smart Grid Technologies (ISGT Europe), 2012 3rd IEEE PES International Conference and Exhibition on*, pages 1–6. IEEE, 2012.

[22] L. Ning, X. Wang, and Y. Teng. Experiment on wind power integration grid via fractional frequency transmission system: Realization of the variable-speed variable-frequency power wind. In *Electric Utility Deregulation and Restructuring and Power Technologies (DRPT), 2011 4th International Conference on*, pages 444–449, July 2011. doi: 10.1109/DRPT.2011.5993932.

[23] Y. Cho, G.J. Cokkinides, and A.P. Meliopoulos. Lfac-transmission systems for remote wind farms using a three-phase, six-pulse cycloconverter. *Power Electronics and Machines in Wind Applications (PEMWA), 2012 IEEE*, pages 1–7, 2012.

[24] H. Chen, M.H. Johnson, and D.C. Aliprantis. Low-frequency ac transmission for offshore wind power. 2013.

[25] P. Achara and T. Ise. Operating phase and frequency selection of low frequency ac transmission system using cycloconverters. In *Power Electronics Conference (IPEC-Hiroshima 2014 - ECCE-ASIA), 2014 International*, pages 3687–3694, May 2014. doi: 10.1109/IPEC.2014.6870028.

[26] N. Qin, S. You, Z. Xu, and V. Akhmatov. Offshore wind farm connection with low frequency ac transmission technology. July 2009.

[27] I. Erlich, F. Shewarega, H. Wrede, and W.-J. Fischer. Low frequency ac for offshore wind power transmission - prospects and challenges. In *AC and DC Power Transmission, 11th IET International Conference on*, pages 1–7, Feb 2015. doi: 10.1049/cp.2015.0017.

[28] P.B. Wyllie, Y. Tang, L. Ran, T. Yang, and J. Yu. Low frequency ac transmission-elements of a design for wind farm connection. In *AC and DC Power Transmission, 11th IET International Conference on*, pages 1–5. IET, 2015.

[29] F.F. da Silva and C.L. Bak. *Electromagnetic Transients in Power Cables*. Springer, 2013.

[30] W.H. Hayt and J.A. Buck. *Engineering Electromagnetics*. McGraw Hill, sixth edition, 2001.

[31] M. Zubiaga et al. *Energy Transmission and Grid Integration of AC Offshore Wind Farms*. InTech, 2012.

[32] L. Marti. Simulation of transients in underground cables with frequency-dependent modal transformation matrices. *Power Delivery, IEEE Transactions on*, 3(3):1099–1110, 1988.

[33] A. Pagnetti. *Cable modeling for electromagnetic transients in power systems*. PhD thesis, University of Bologna, 2012.

[34] M. Khatir, Z.S. Ahmed, S. Hadjeri, and M.K. Fellah. Comparison of hvdc line models in psb/simulink based on steady-state and transients considerations. *Acta Electrotechnica et Informatica Vol*, 8(2):50–55, 2008.

[35] TransEnergie Technologies. *SimPowerSystems for use with Simulink*. The MathWorks, version 3 edition, 2003.

[36] J.R. Marti, L. Marti, and H.W. Dommel. Transmission line models for steady-state and transients analysis. In *Athens Power Tech, 1993. APT 93. Proceedings. Joint International Power Conference*, volume 2, pages 744–750. IEEE, 1993.

[37] U.S. Gudmundsdottir. *Modeling of long High Voltage AC Cables in the Transmission System*. PhD thesis, Aalborg University, 2010.

[38] N. Watson and J. Arrillaga. *IET Power and Energy Series, Volume 39 - Power Systems Electromagnetic Transients Simulation*. Institution of Engineering and Technology, 2007. URL `http://app.knovel.com/hotlink/toc/id:kpIETPESV1/iet-power-energy-series/iet-power-energy-series`.

[39] Ieee standard requirements, terminology, and test code for shunt reactors rated over 500 kva. *IEEE Std C57.21-1990*, pages 1–, 1991. doi: 10.1109/IEEESTD.1991.101052.

[40] M.H.J. Bollen, S. Mousavi-Gargari, and S. Bahramirad. Harmonic resonances due to transmission-system cables. In *Proc. of the International Conference on Renewable Energies and Power Quality, Cordoba, Spain*, 2014.

[41] F.F. da Silva, W. Wiechowski, C.L. Bak, and U.S. Gudmundsdottir. Full scale test on a 100 km, 150 kv ac cable. In *CIGRE Session 2010*, August 2010.

[42] J. Machowski et al. *Power System Dynamics - Stability and Control*. Wiley, second edition, 2012.

Appendix A

Supporting Theory

A.1 Charging Currents

Consider a per phase transmission cable (lossless) with equivalent impedance and admittance in fig. A.1.

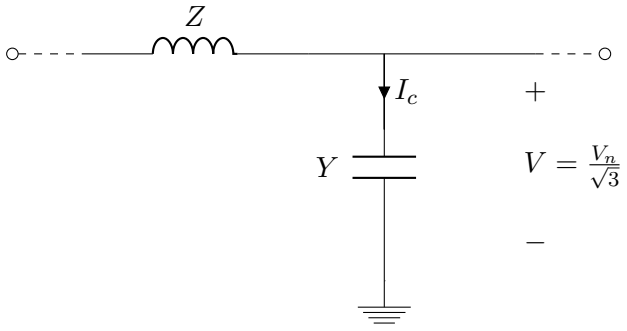

FIGURE A.1: Charging current in an HVAC cable

The capacitive charging current is the current flowing through the capacitance between the phase and ground, charging and discharging the cable. It can be expressed by:

$$I_c = VY = \frac{V_n}{\sqrt{3}}Y = \frac{V_n}{\sqrt{3}}\omega Cl = \frac{V_n}{\sqrt{3}}2\pi fCl \tag{A.1}$$

A.2 Power Transmission

When a transmission line is considered being lossless, R and G are neglected. The resulting characteristic impedance Z_c is purely resisttive (real), while the propagation

constant γ becomes purely imaginary [42]. See eq. (A.2) and (A.3).

$$\underline{Z}_c = Z_c = \sqrt{\frac{\underline{Z}}{\underline{Y}}} = \sqrt{\frac{L}{C}} \tag{A.2}$$

$$\underline{\gamma} = \sqrt{\underline{Z}\underline{Y}} = j\omega\sqrt{LC} \tag{A.3}$$

Hence, in this case, $\alpha = 0$ and $\beta = \omega\sqrt{LC}$. This leads to a change in the hyperbolic functions as $\sinh(\underline{\gamma}l) = j\sin(\beta l)$ and $\cosh(\underline{\gamma}l) = \cos(\beta l)$.

$$\begin{bmatrix} \underline{V}_S \\ \underline{I}_S \end{bmatrix} = \begin{bmatrix} \cosh(\underline{\gamma}l) & \underline{Z}_c \sinh(\underline{\gamma}l) \\ \frac{1}{\underline{Z}_c}\sinh(\underline{\gamma}l) & \cosh(\underline{\gamma}l) \end{bmatrix} \begin{bmatrix} \underline{V}_R \\ \underline{I}_R \end{bmatrix} \tag{A.4}$$

becomes

$$\underline{V}_S = \underline{V}_R \cos(\beta l) + jZ_c\underline{I}_R \sin(\beta l) \tag{A.5}$$

$$\underline{I}_S = \underline{I}_R \cos(\beta l) + j\frac{\underline{V}_R}{Z_c} \sin(\beta l) \tag{A.6}$$

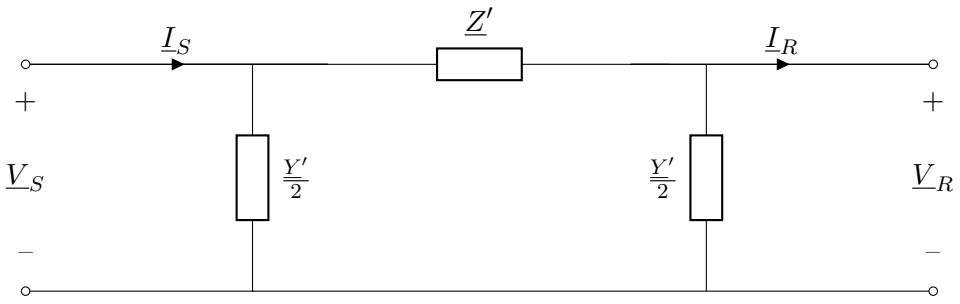

FIGURE A.2: Equivalent circuit for a transmission cable

$\underline{V}_R$ is the reference phasor, and $\underline{V}_S$ leads $\underline{V}_R$ by the *transmission angle* δ. Therefore, $\underline{V}_R = V_R$ and $\underline{V}_S = V_S e^{j\delta}$. δ is sometimes referred to as the *load angle*. From eq. (A.5), the receiving end current can be expressed as:

$$\underline{I}_R = \frac{\underline{V}_S - \underline{V}_R \cos(\beta l)}{jZ_c \sin(\beta l)} = \frac{V_S}{Z_c \sin(\beta l)} e^{j(\delta - \pi/2)} - \frac{V_R \cos(\beta l)}{Z_c \sin(\beta l)} e^{-j\pi/2} \tag{A.7}$$

Receiving end apparent power can be expressed as:

$$\underline{S}_R = \underline{P}_R + j\underline{Q}_R = \underline{V}_R \underline{I}_R^* \tag{A.8}$$

Inserting the expression for $\underline{I}_R$:

$$\underline{S}_R = \frac{V_R V_S}{Z_c \sin(\beta l)} e^{j(\delta - \pi/2)} - \frac{V_R^2 \cos(\beta l)}{Z_c \sin(\beta l)} e^{-j\pi/2} \tag{A.9}$$

Hence, the real power at the receiving end is

$$P_R = Re[\underline{S}_R] = \frac{V_S V_R}{Z_c \sin(\beta l)} \sin(\delta) \tag{A.10}$$

For short and medium-length lines βl is very small, and $\sin(\beta l) \cong \beta l$.

$$P_R \cong \frac{V_S V_R}{Z_c \beta l} \sin(\delta) = \frac{V_S V_R}{\sqrt{\frac{L}{C}} \omega \sqrt{LC} l} \sin(\delta) = \frac{V_S V_R}{\omega L} \sin(\delta) \tag{A.11}$$

$$P_R = \frac{V_S V_R}{X_L} \sin(\delta) \tag{A.12}$$

where X_L is the inductive reactance of the transmission line/cable. It should be noted, however, that this is only valid for short lossless lines. For longer lines or cables, this simplification might not be acceptable. This is due to the higher capacitance of underground cables compared to overhead lines (OHLs), and thus the phase constant β will be higher.

The reactive power can be derived from eq. (A.9):

$$Q_R = Re[\underline{S}_R] = \frac{V_R V_S}{Z_c \sin(\beta l)} \cos\delta - \frac{V_R^2 \cos(\beta l)}{Z_c \sin(\beta l)} = \frac{V_R}{Z_c \sin(\beta l)} (V_S \cos(\delta) - V_R \cos(\beta l)) \tag{A.13}$$

A.3 Power Transformer

Power transformers are essential in a power systems, as they make it possible to convert low voltages from generating units to high levels to reduce losses in the power transmission. They are also necessary in order to transform the voltage to the appropriate level for the end user. Fig. A.3 depicts the equivalent circuit for a ideal single phase transformer, with a transformation ratio of N_1/N_2. The root mean square (RMS) voltage induced in the primary winding, E_1 is caused by the mutual flux which links the primary and secondary coils.

If the flux is assumed to be sinusoidal:

$$\phi = \Phi_{max} \cos(\omega t) \tag{A.14}$$

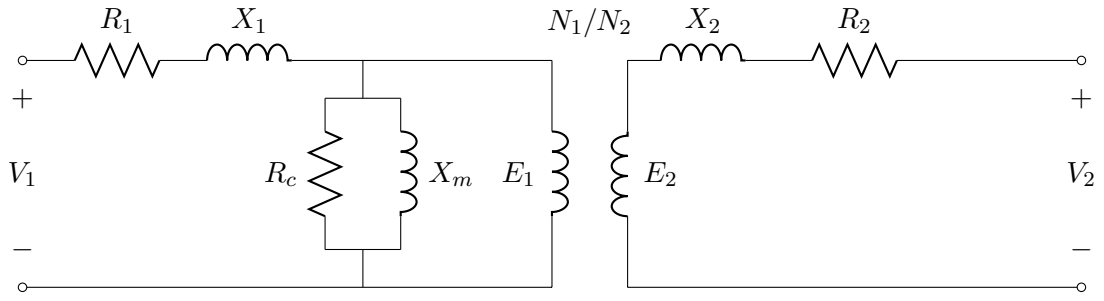

FIGURE A.3: Equivalent circuit showing a single phase, two-winding transformer

the instantaneous induced voltage e_1 is

$$e_1 = N_1 \frac{d\phi}{dt} = -\omega N_1 \Phi_{max} \sin(\omega t) = E_{1max} \cos(\omega t + 90^\circ) \tag{A.15}$$

where

$$E_{1max} = 2\pi f N_1 \Phi_{max} \tag{A.16}$$

and the corresponding RMS value

$$E_1 = \frac{1}{\sqrt{2}} 2\pi f N_1 \Phi_{max} = 4.44 f N_1 \Phi_{max} \tag{A.17}$$

or alternatively, with the flux represented by the cross-section of the transformer core A_c, and the flux density B.

$$E_1 = 4.44 f N_1 A_c B \tag{A.18}$$

Equivalently, the RMS voltage in the secondary coils is given as

$$E_2 = 4.44 f N_2 A_c B \tag{A.19}$$

A.4 The Per Unit System

Base value in p.u. $= \frac{\text{Quantity in SI units}}{\text{Base value}}$

To find the per unit values for voltage and current:

$$V_{p.u.} = \frac{V}{V_{base}} \tag{A.20}$$

$$I_{p.u.} = \frac{I}{I_{base}} \tag{A.21}$$

where

$$I_{base} = \frac{S_{base}}{V_{base}} \tag{A.22}$$

Appendix B

Frequency Analysis

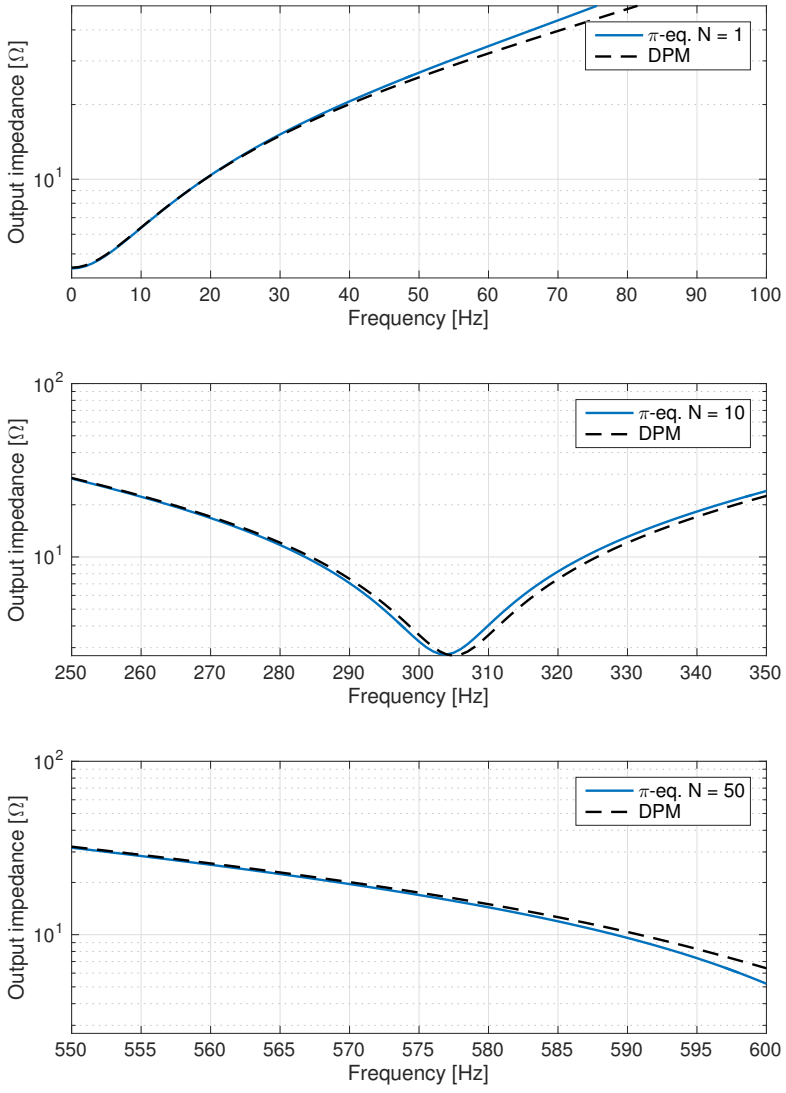

FIGURE B.1: Frequency range where π-models start deviating from the DPM

Appendix C

Ferranti Effect

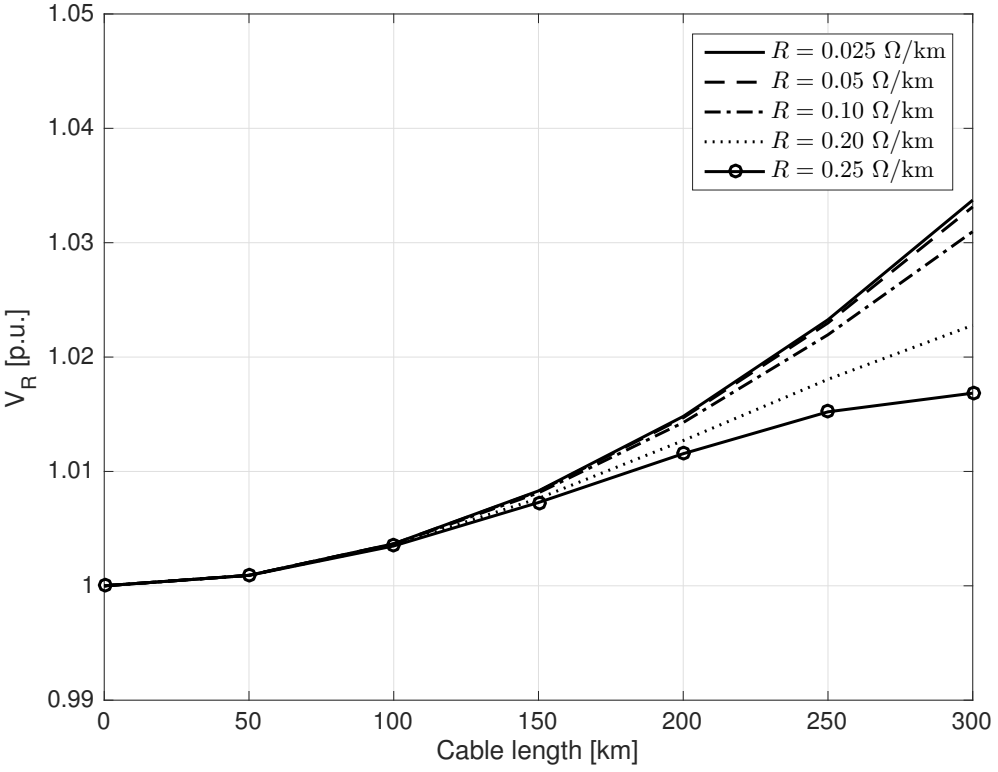

FIGURE C.1: Ferranti effect in an LFAC cable for varying conductor resistance

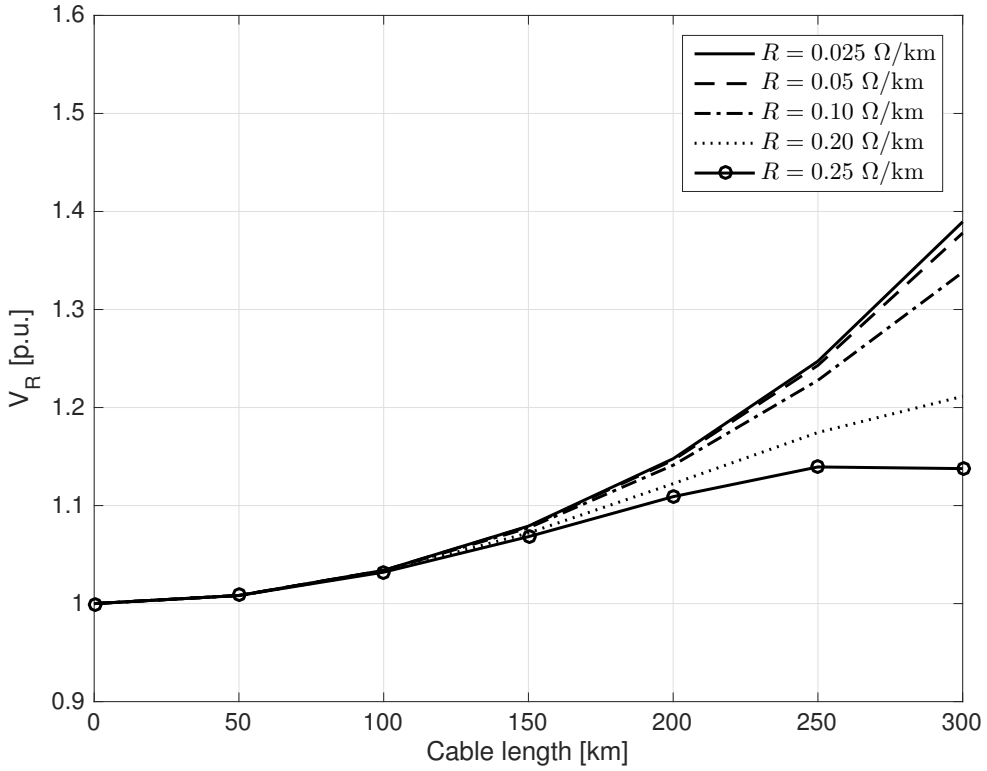

FIGURE C.2: Ferranti effect in an HVAC cable for varying conductor resistance

Appendix D

Fault Analysis

D.1 Fault at Sending End of an HVAC System

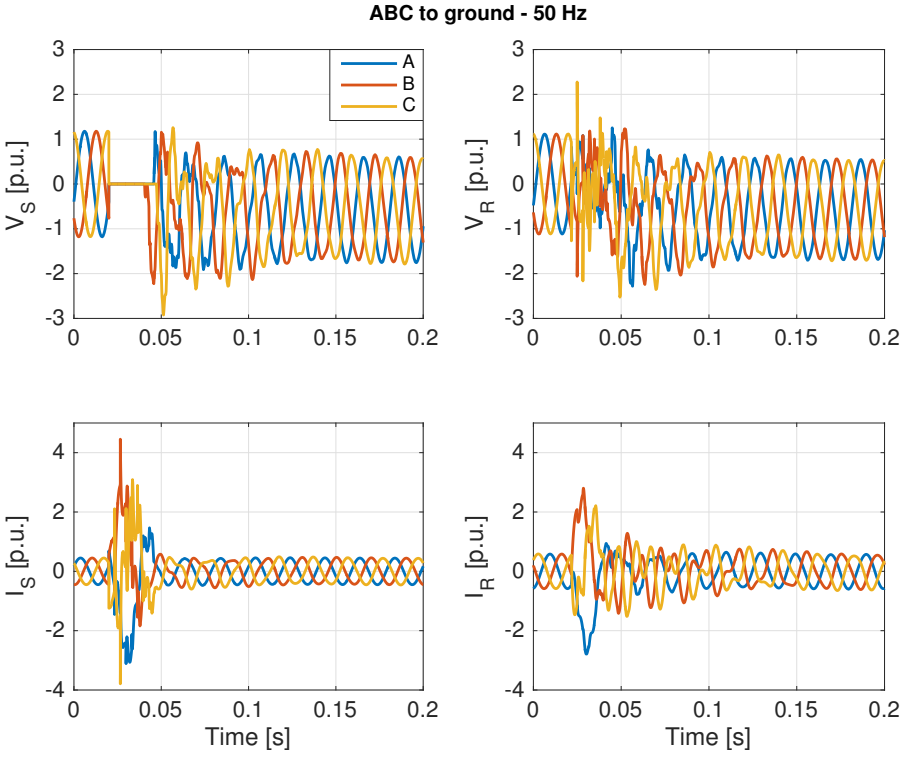

FIGURE D.1: Sending and receiving end voltages and currents before, during and after a three phase to ground fault for an HVAC system

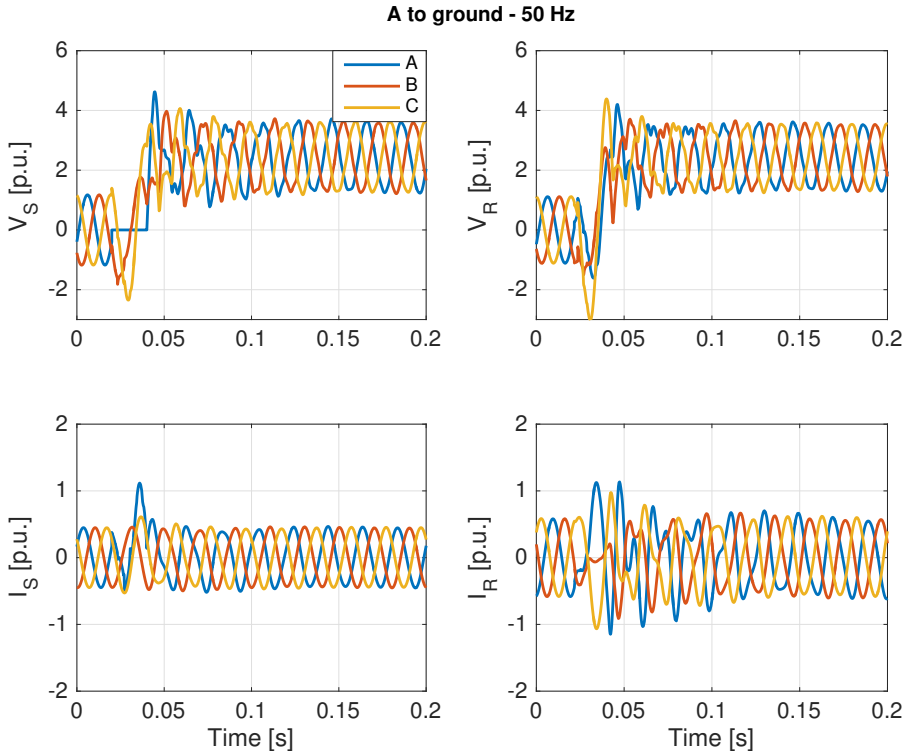

FIGURE D.2: Sending and receiving end voltages and currents before, during and after a single phase to ground fault for an HVAC system

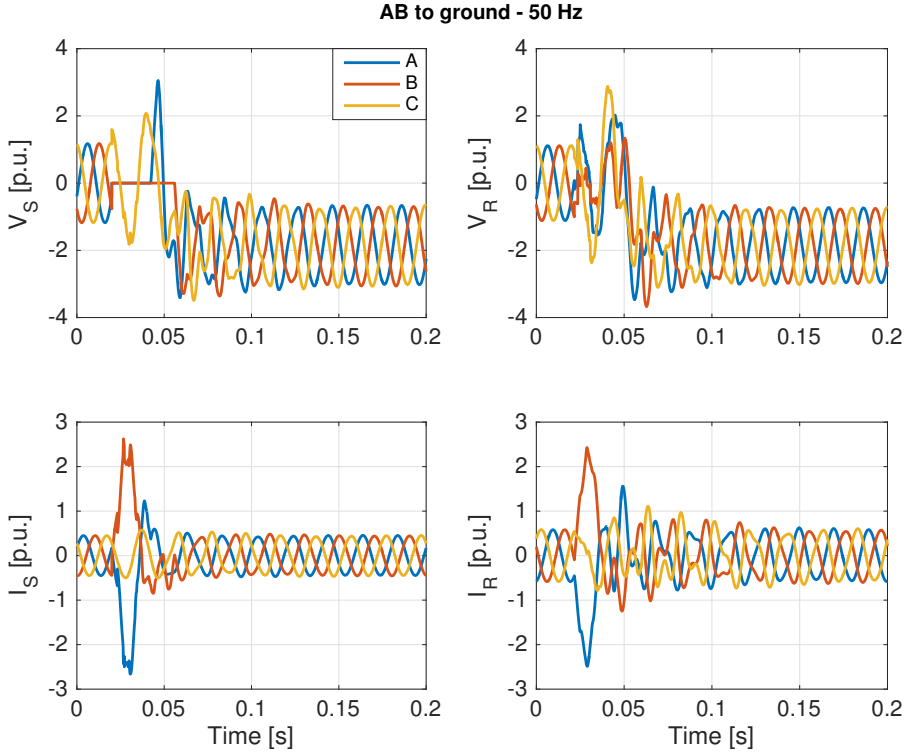

FIGURE D.3: Sending and receiving end voltages and currents before, during and after a double phase to ground fault for an HVAC system

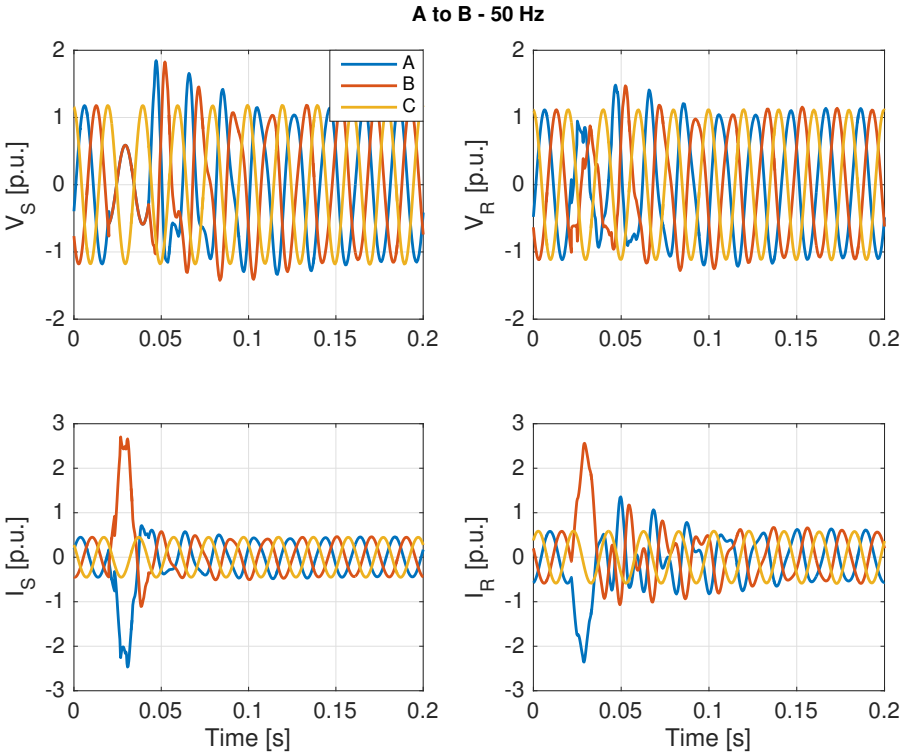

FIGURE D.4: Sending and receiving end voltages and currents before, during and after a single phase to phase fault for an HVAC system

D.2 Average DC Offset

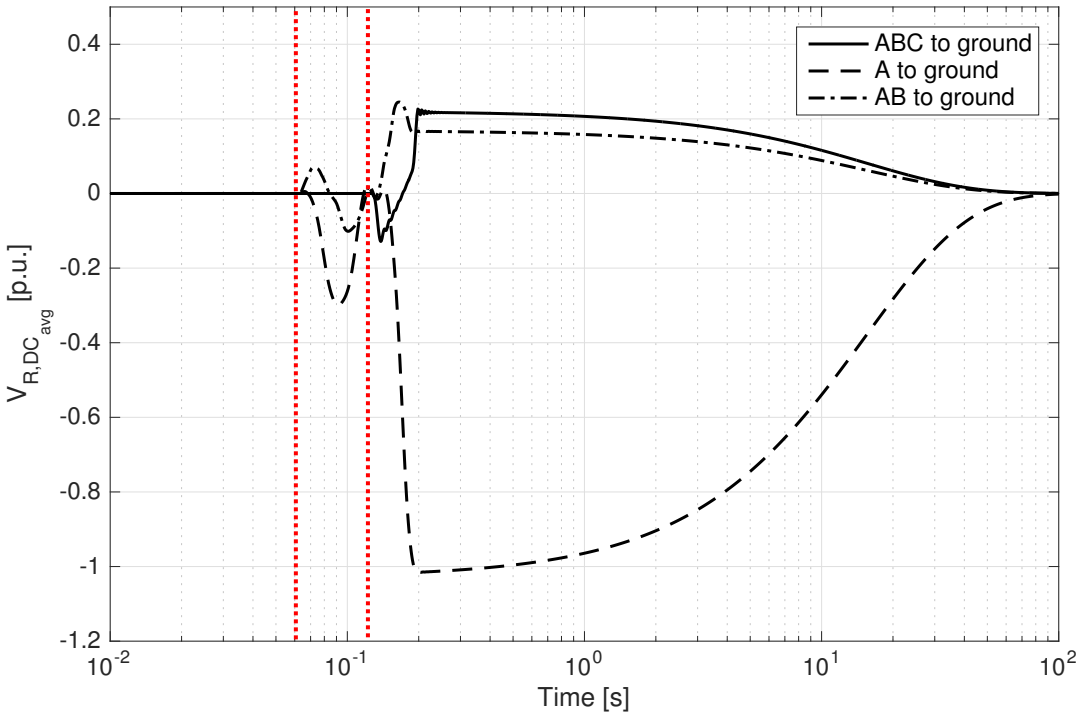

FIGURE D.5: Average DC offset for three different fault events. Red dotted lines indicate the fault time interval

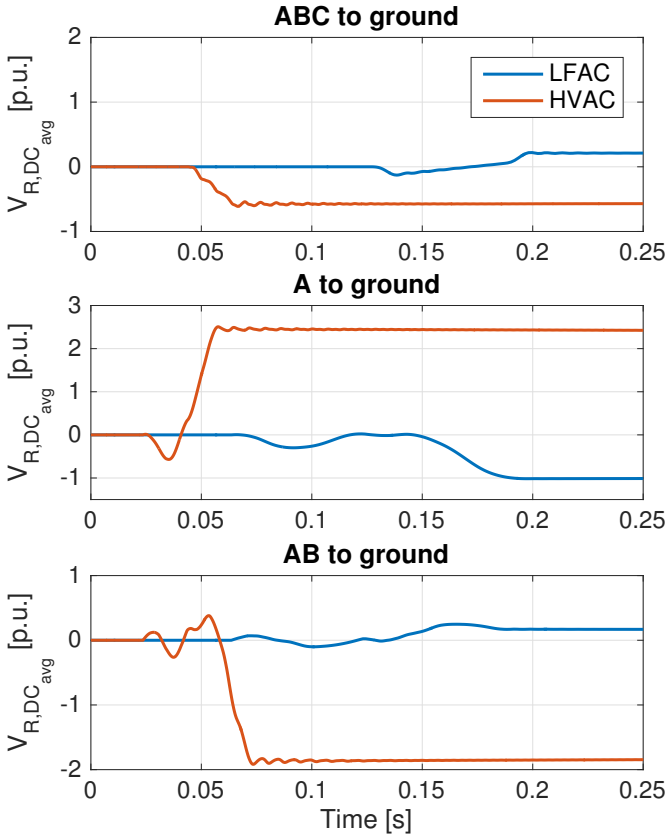

FIGURE D.6: Average DC offset for the LFAC and HVAC systems

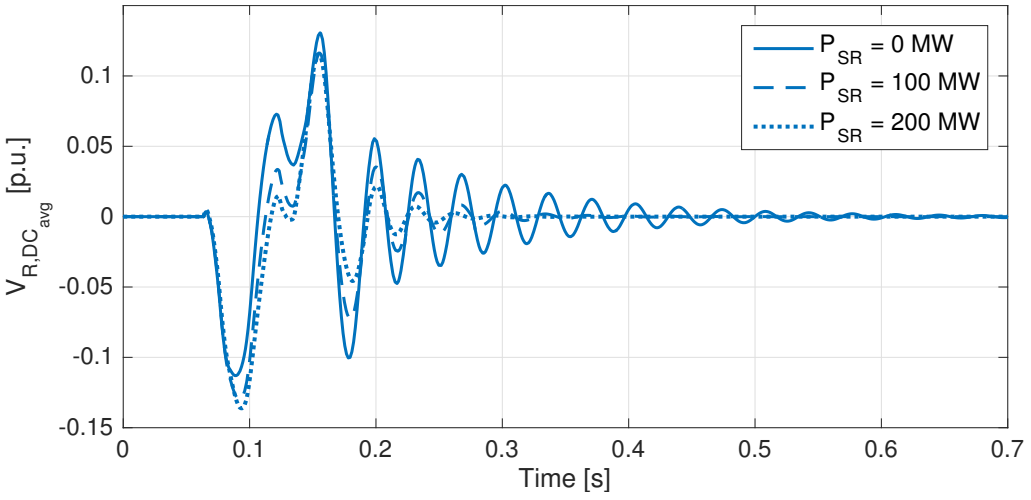

FIGURE D.7: Average DC offset for the LFAC system with connected shunt reactor and different degree of damping, $Q_{SR} = 350$ MVA